Photoinduced Dynamics
in OH, H_2, and N_2O

Mark P. J. van der Loo

Photoinduced Dynamics in OH, H_2, and N_2O

Een wetenschappelijke proeve op het gebied van de
Natuurwetenschappen, Wiskunde en Informatica

Proefschrift

ter verkrijging van de graad van doctor
aan de Radboud Universiteit Nijmegen
op gezag van de rector magnificus prof. mr. S.C.J.J. Kortmann,
volgens besluit van het College van Decanen
in het openbaar te verdedigen op `maandag 26 mei 2008`
om `13:30` uur precies

door

Mark Petrus Jacobus van der Loo

geboren op 28 september 1976
te Deurne

Aan mijn ouders,

omdat ik op de schouders van reuzen sta.

Contents

CHAPTER 1

Introduction

The focus of this introduction is to introduce the non-specialist reader into the subjects of this thesis. For more specialized introductions and theory the reader is referred to the subsequent chapters.

This thesis is about the influence that light has on the behaviour of small molecules. With small molecules, we mean molecules which consist of only a few atoms. These molecules are to be found almost everywhere in nature. Any physical environment with temperatures below about 5000 K is capable of hosting molecules, and thus one can obtain information about these environments by studying the molecules in them. Examples of environments where the study of small molecules is important include combustion engines and flames, planetary atmospheres, the interstellar medium and molecular clouds, star-, and planet forming regions, and the universe before the formation of the first stars. It is often hard to study molecules directly in their environment. However, since molecules (and atoms) interact with electromagnetic radiation, we can study the light which is emitted or altered by atoms and molecules. Thus, if we precisely understand the interaction between molecules and electromagnetic radiation we can gain information about the environment they are in, such as pressure, temperature and the presence of electric or magnetic fields. Alternatively, molecules can be probed, and even controlled in the laboratory using precisely tuned electromagnetic fields.

1.1   The shoulders of giants

It was first noticed by William Hyde Wollatson in 1802 that the spectrum of
sunlight contains dark lines. These, and more lines were independently redis-
covered and categorized by Josef von Fraunhofer in 1814, who first recognized
the importance of this discovery. Fraunhofer's work opened up an active field
of research, called spectroscopy, which in 1860 culminated in Kirchoff and
Bunsen's statement[1] that every chemical element has a characteristic ab-
sorption spectrum. They deduced that the dark lines in the solar spectrum
were due to absorption of solar light by elements in the sun's atmosphere[2,3].
Kirchoff also formulated his three laws of spectroscopy, which postulated
the black-body radiation of heated bodies, and the discrete absorption and
emission lines of gases.

Although this realization quickly found applications, no underlying phys-
ical theory of light-matter interaction existed. In fact, no complete theory
of electromagnetism existed. An important step was taken by James Clerk
Maxwell[4], who, building on the work of Michael Faraday, published a paper
in 1861 where he first unified magnetic and electric phenomena in terms of
a mechanical model. Later, Maxwell abandoned the mechanical interpreta-
tion, and in 1864 he presented his dynamical theory of the electromagnetic
field before the Royal Society[5–7]. Maxwell's of theory electromagnetic fields
could describe for the first time electromagnetic fields in terms of propa-
gating waves. The theory also describes the interaction of electromagnetic
fields with (macroscopic) material objects. Maxwell's theory was soon con-
firmed experimentally by Heinrich Rudolf Hertz who discovered radio waves
in 1888[8]. The classical theory of electromagnetism was developed further in
the second half of the 19th century, where important contributions were made
by Lorentz, Poynting, and Heaviside. The latter is credited for transforming
Maxwell's original twenty differential equations to the set of four vector dif-
ferential equations which are found in the textbooks today. It is safe to say
that the dynamical theory of electromagnetic fields revolutionized science in
the 19th century, since Maxwell developed the first physical theory where
Newton's idea of action on a distance was left behind. This concept, *via* the
work of Lorentz, ultimately led to the development of special relativity.

In spite of the large successes obtained trough the development of classical
electromagnetism, physics was facing some severe problems at the end of
the 19th century. In 1885, Johann Jakob Balmer had published a simple
formula that predicts the occurrence of a series of lines in the spectrum
of the hydrogen atom[9]. However, there was no underlying physical model
which explains why there should be discrete lines, nor why they should occur
exactly at the places where they do. A second problem was the shape of

the spectrum of black body radiation emitted by heated objects. The latter problem was solved by Max Planck, who published a paper in 1901, where he assumed that matter and radiation can exchange energy only in discrete quantities[10]. Using the machinery of statistical mechanics, he was able to derive the shape of the black body spectrum. The idea of quantized radiation-matter interaction was taken a step further by Albert Einstein. In 1905 he postulated that the fact that light-matter interaction occurs in discrete quantities of energy, is not a property of the interaction process, but rather that electromagnetic radiation itself comes in quantized packets[11]. With this assumption, he was able to explain the photo-electric effect[12] which had been discovered by Hertz[13] in 1887. Thus, Einstein abandoned Maxwell's theory of electromagnetic radiation by introducing a wave-particle duality for electromagnetic radiation. In 1907, Einstein showed[14] in a paper on the specific heat of solids, that the motion of atoms oscillating in a solid also has to be quantized in order to account for Planck's radiation law. Thus, in less than a decade after 1900, the measurement and modeling of light-matter interaction had undermined the foundations of 19th century physics: classical electromagnetism and classical mechanics. An equally important role was played by the emerging theory and measurements on radioactivity and scattering of charged particles, and the theory of (special) relativity. However, the focus of this thesis is on light-matter interaction. On the atomic and molecular level, physics was back to the same situation as around 1860: phenomenological models existed, but no underlying theory for the structure of matter and radiation existed to explain phenomena on that scale.

In 1911, Ernest Rutherford published a paper[15], where he reanalyzed scattering experiments of Geiger and Marsden[16,17]. He deduced that atoms must consist of a positive charge centered in a small volume with negatively charged electrons in a much larger volume around it. In 1913 Niels Bohr published a paper[18] in which he developed a physical model for the hydrogen atom. He postulated that electrons occupy stable, discrete circular orbits around the nucleus, and that light can induce transitions between those orbits. According to Bohr's theory, the electron cannot have any amount of energy of motion, but only certain values $E(n)$, which can be numbered with $n = 0, 1, 2, \ldots$. The value of n determines the energy, and is nowadays called a quantum number. The frequencies of light which can be absorbed by the atom are then determined by the energy differences between the states numbered with different n. This model, combined with Planck's radiation law allowed Bohr to derive the spectroscopic line series of Balmer, and a similar series found by Paschen in 1908[19]. In fact, he predicted a family of series, of which one had been observed by Lyman in 1906[20], but Bohr was not aware of at that time.

Bohr's paper was the start of what is now known as the "old quantum theory". In the old quantum theory, a system of particles would be treated with classical mechanics, augmented with certain *ad hoc* quantization rules, just like Bohr had done in his paper. In classical mechanics, a system of particles can in theory have any internal energy of motion E. Finding quantisation rules amounts to limiting the possible energies for such a system to a countable number of energies. Bohr had done this for the motion of an electron about a nucleus and later similar procedures were found for the rotational motion of complete molecules, and for the vibrational motion of atoms in molecules. In the decade or so following the publication of Bohr's paper, spectroscopists adopted the old quantum theory to interpret many atomic and molecular spectra. For example, in the old quantum theory, the possible end-over-end rotational energies $E(J)$ of a diatomic molecule were given by[21,22]:

$$E(J) = hc[B(J^2 + const.) + DJ^4 + FJ^6 \ldots], \tag{1.1}$$

where h is Planck's constant, c the speed of light, the B, D and F are so-called spectroscopic constants and J is the rotational quantum number, which can take values $0, 1, 2, \ldots$. Although the old quantum theory allowed spectroscopists to interpret and classify the spectra of many molecules, it was certainly not complete. Firstly, the old quantum theory works only for systems where particles stick together, such as atoms and molecules, but it does not work for processes where particles collide, recombine, or dissociate. Secondly, there was no way of determining spectroscopic constants such as B, D, F.. from theory, since there was no underlying mathematical theory which explained why the energies should be discrete at all. These problems, and more, were solved with the advent of the modern quantum theory in 1925.

Modern quantum theory was developed independently *via* two different routes. The first to arrive at modern quantum theory was Werner Heisenberg, who invented and published his matrix mechanics in 1925[23]. In his theory, observable quantities (observables) are represented by mathematical matrices. The development of observables in time is described by the development of these matrices in time according to the Heisenberg equation. At around the same time, Louis de Broglie suggested in his PhD thesis[24] that not only light, but also material particles exhibit a wave-particle duality. Using this idea, he was able to mathematically derive the Bohr-Sommerfelt quantization rules from the old quantum theory. In 1926[a] Erwin Schrödinger

---

[a]One often finds the year 1925 for the discovery of the Schrödinger equation. It is known that it was actually derived by Schrödinger in 1925 but appeared in print in 1926. The paper was received by *Annalen der Physik* on January 27, 1926.

published the mathematical equation that describes how these matter-waves must propagate in time[25,26]. With his formulation Schrödinger derived the spectrum of the hydrogen atom, and he showed that his formulation could be generalized to other systems. Not much later he also showed that his wave mechanical description is completely equivalent to Heisenberg's matrix mechanics[27].

The impact of modern quantum theory on atomic and molecular physics was, and is, huge. The formulation of quantum mechanics led to a whole series of discoveries of new physical phenomena, which continues to this day. Some achievements worth mentioning here are: the explanation of the chemical bond (Heitler and London, 1927)[28], the quantum mechanical description of absorption and emission of electromagnetic radiation by atoms, (Dirac, 1927)[29], the discovery of electron spin (Uhlenbeck and Goudsmit, 1925)[30,31] and it's explanation as a consequence of special relativity by Dirac in 1928[32,33].

The appearance of quantum mechanics also had a large impact on the field of spectroscopy. For example, as it turns out the equation giving energy levels for rotating diatomic molecules, derived in the old quantum theory [see Eq. (1.1)] is not entirely correct. A better equation is given by:

$$E(J) = hc[BJ(J+1) + DJ^2(J+1)^2 + ...], \qquad (1.2)$$

where, depending on the molecule, J can have the values $1, 2, \ldots$ or $1/2, 3/2, \ldots$. The fact that J can be half-integer is a consequence of the existence of spin. In principle, using modern quantum mechanics one can also calculate the constants $B, D, \ldots$ for molecules, although it is certainly no straightforward calculation. Similar changes were necessary for quantum numbers describing vibration of molecules. This led to a complete revision of spectroscopic constants, in the years following 1925, culminating to a paper by Robert Mulliken[22] in 1930 where the modern standards for spectroscopic notation were settled. Nearly all conventions put down in Mulliken's paper are still in use today. It is safe to say that the paper by Mulliken marks the completion of the foundation for modern spectroscopy, nearly 130 years after Wollatson noted the dark lines in the spectrum of the sun.

Nowadays, spectroscopy plays a central role in molecular science, and virtually every application or experiment which is designed to investigate molecular processes includes some form of spectroscopy. One of the most important ideas being developed nowadays theoretically as well as experimentally, is that electromagnic fields and radiation can be used not only to perform measurements on molecules, but to also control them.

Important examples include hexapole focusing, where a beam of molecules is focused at some point in a vacuum chamber by leading them through

a hexapolar electromagnetic field, and Stark deceleration[34] where a beam of molecules can be slowed down using carefully tuned electromagnetic fields and eventually even be trapped. Once molecules can be precisely controled, it becomes possible to perform experiments on them which, combined with detailed theoretical models, can give insight into their dynamics on a fundamental level. One example is the velocity map imaging[35–37] technique, where a laser is focused on a controled beam of molecules, causing some of the molecules to break up. With velocity mapped imaging, it is possible to study the the quantum distribution of the separating fragments as a function of their flight direction and velocity. Together with theoretical models, these experiments make it possible to study molecular processes in unprecedented detail. Other examples include the study of precisely controlled molecular collisions and chemical reactions. In the relatively new field of "cold molecules[38]", researchers are trying to cool down molecular gases to the point where they form a Bose-Einstein condensate. Development in this field also strongly depends on the availability of sound theoretical models and computational methods. For example, using methods from theoretical chemistry, it is possible to point out or reject candidate molecules to cool to Bose-Einstein condensates for certain experiments[39]. One advantage of being able to slow down and cool ensembles of molecules is that the interaction time with a probing laser can be drastically increased, allowing for accurate measurements. Developments in ultrahigh resolution molecular spectroscopy are now reaching the point where spectroscopists are able to study the possible variability of fundamental constants, such as the electron-proton mass ratio[40,41] and the fine structure constant[42].

1.2 Photoinduced dynamics

The most important forces that govern the behaviour and structure of a molecule are electromagnetic in nature. Therefore, when a molecule is put in an external electromagnetic field, the dynamics of the electrons and nuclei which constitute the molecules will change. The collection of effects that can occur, are called photoinduced dynamics. Examples include excitation of the vibrational or rotational motion of the nuclei, excitation of the electronic motion in the molecule, break-up of the molecule (photodissociation) either directly or *via* some intermediate process (predissociation), and formation of molecules from separate fragments (radiative association, Raman association). Most of the examples mentioned here are treated in later chapters of this thesis.

In a complete theoretical description, the electromagnetic attraction be-

tween electrons and nuclei, the repulsion between electrons and nuclei amongst each other, and interaction with the external electromagnetic field should be treated quantum mechanically. However, there are certainly no analytical solutions available for the equations that govern such complex systems, and it is computationally difficult to obtain numerical solutions. Fortunately, it is possible to make some simplifying assumptions by neglecting or approximating relatively small physical effects. First, electromagnetic interactions are treated classically, and it is assumed that electromagnetic forces act instantly between charged particles instead of traveling with the speed of light. Second, it is assumed that the electrons and nuclei move slowly enough (with respect to the speed of light), so that special relativistic effects can be ignored. The conditions that validate the first assumption are easily met here. The molecules that are studied in this work are very small (typically on the order of 1 Å$= 10^{-10}$ m), so it takes a very short time for light to travel through the system. The second assumption becomes problematic only when the atoms involved are much heavier than the ones that are treated in this work. However, it does imply that spin has to be introduced *ad hoc* (by introducing it as an extra degree of freedom in the wave function), to account for the electronic and nuclear structure of the molecule.

Finally, we assume that the field external to the molecule is weak enough, so that the characteristics of the molecule stay similar to the characteristics of the molecule outside of the field. The computational methods following from the third assumption are called perturbation theory. It is based on the notion that the stable configurations of a system will change only slightly when a small influence (perturbation) is exerted from outside.

With these assumptions, the procedure to theoretically describe photoinduced dynamics separates into two steps: first, the wave function for the free molecule is found by numerically solving the corresponding Schrödinger equation, and second, perturbation theory is applied to model the dynamics induced by external electromagnetic fields. However, as it turns out, molecules are so complex that an extra assumption must be made to handle the first step: the so-called adiabatic-, or Born-Oppenheimer approximation[43]. Since the atomic nuclei are much heavier than their surrounding electrons and the total forces exerted upon electrons and nuclei are equal, the nuclei move much slower than the electrons.

This allows one to separate the molecular Schrödinger equation in such a way that it can be solved for the electrons and nuclei consecutively. In many situations, and also in the work described in this thesis, the approximations made here are too severe to accurately reproduce experimental results. Thus, considerable efforts have to be made *a posteriori* to correct for the effects introduced by the approximations. In this work, the coupling between

electronic spin and electronic motion (spin-orbit coupling) and the coupling between nuclear (rotational) motion and electronic motion is especially important. The former effect is caused by neglecting special relativity, the latter by the Born-Oppenheimer approximation.

For example, in Chapter 2 the lifetimes of excited electronic states of the OH radical are calculated. In the process that is studied, the OH molecule can make a transition from an excited electronic bound state to an unbound state *via* spin-orbit coupling or a coupling between rotational motion of the nuclei with electronic motion. This effect shortens the lifetime of the studied states (otherwise determined by radiative decay) by a factor of ten or more. In Chapter 3 the rovibrational energy level spectrum and radiative lifetimes of OH in the electronic ground state are computed. Neglecting coupling between rotational and electronic motion would result in about 10% difference in some of the computed lifetimes. In Chapter 4, coupling between nuclear rotational motion and electronic motion is included in the calculations to reproduce the energy level spectrum of molecular Hydrogen. The fact that the peaks in the so-called Raman association spectrum (Fig. 4.3 and 4.4) are split in two is also a consequence of nuclear rotaional motion. Finally, in Chapter 6, momentum coupling (non-adiabatic coupling, neglected in the Born-Oppenheimer approximation) between five different electronic states of N_2O is essential to describe photodissociation processes in the N_2O molecule.

1.3   Molecules in this thesis

In the following subsections, some examples are given where the molecules treated in this work are of importance. The main results of this thesis are sketched.

1.3.1   The hydroxyl radical OH

The OH molecule is a highly reactive agent (radical) in the earth's atmosphere. It is produced mainly by photodissociation of water induced by the sun's ultraviolet radiation, but it is also present as a chemical reaction intermediate. Because of it's high reactivity, the OH molecule helps transforming many types of molecules in the earth's atmosphere, some of which are emitted by mankind. For this reason the OH molecule is sometimes referred to as the atmosphere's cleaning agent. In Fig. 1.1 an overview of some processes involving OH in the earth's atmosphere are shown.

One way to perform measurements on the atmosphere, is to observe the radiation that is emitted by atmospheric OH on the night side of earth. Dur-
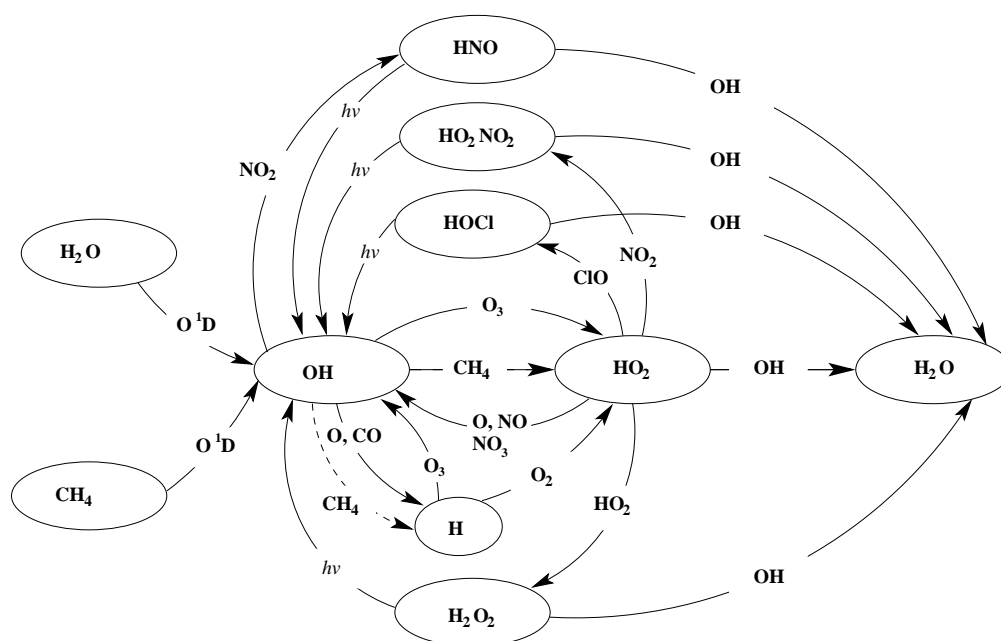
Figure 1.1: Schematic overview (Nicolet diagram) of chemical processes in the earth's atmosphere involving the OH molecule[44]. Species on the arrows are reactants.
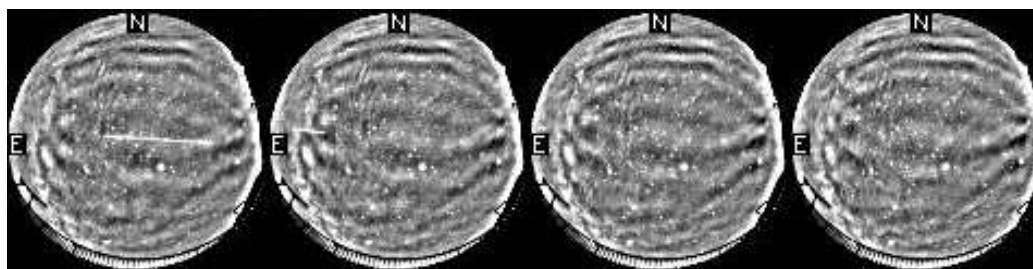
Figure 1.2: False color images of OH infrared radiation in the night sky[45]. The ripples are called gravity waves, and are caused by temperature and pressure differences in the earth's atmosphere.

ing the day, OH radicals are excited (heated up) by sunlight and during the night they can emit infrared radiation which may be observed from earth (see Fig. 1.2). The radiation process is a quantum mechanical process, and it is clear that a thorough understanding of it can directly lead to better understanding of OH in atmospheric circumstances, and thus improve atmospheric research. In Chapter 3 we report, among other things, on accurate calculations of emission coefficients for OH.

A second field where OH plays an important role is in astrophysics. For example, the stimulated emission of radio waves (MASER) by OH-molecules near supernovae are measured by radio astronomers to investigate supernova shock waves[46]. Other applications of OH-MASERs include the investiagation of pulsars[47], star-forming regions[48] and envelopes of late-type stars[49].

OH radicals are also produced in our own solar system by comets. When comets approach the sun, water vaporizes from the outer mantle, which subsequently dissociates under the influence of sunlight into H and OH. Some of the highly excited OH radicals will subsequently fall apart into O and H, and some will radiate. Part of the produced OH-molecules will dissociate under the influence of solar radiation. There are several pathways by which OH molecules can dissociate under the influence of sunlight. One of the pathways runs *via* excitation to the so-called $D^2\Sigma^-$ and $3^2\Sigma^-$ states[50].

In chapter 2, a 2+1 Resonance Enhanced MultiPhoton Ionisation (2+1 REMPI) experiment which probes the excited $D^2\Sigma^-$ and $3^2\Sigma^-$ states of the OH molecule is modeled. The nuclear and electronic structure are determined by *ab initio* calculations and rotational constants of these states are determined. A good correspondence between experimental and computed constants is found, and an idea is given of the relative importance of different excitations in the experiment. The various decay processes (emission, predissociation) of these excited states are also studied and compared for the first time. It is concluded that predissociation is the most important decay process for molecules in these excited states.

1.3.2   The hydrogen molecule H_2

The hydrogen molecule (H_2) is subject of the chapters 4 and 5. It is both the most simple neutral molecule and the most abundant molecule in the universe. It was also one of the first molecules to appear in the history of the universe[51–53]. H_2 was present long before the first stars were born, about 10^8 years after the big bang. In fact, it is generally believed that the presence of molecular hydrogen was important for the formation of those first stars. According to current early universe models, the first stars started forming when clouds of atomic hydrogen, deuterium, helium, and some molecular species were formed under the gravitational pull of dark matter. The accumulation of matter causes the gas clouds to increase in temperature, counteracting the collapse. Thus, in order to explain the formation of the first stars, some kind of cooling mechanism must have been present in the early stages. The most probable option is the presence of a molecular species, such as H_2, which is able to convert thermal energy into (infrared) radiation. This raises the question as to how H_2 is formed, and how much H_2 was around at that time.

In Chapter 4, an H_2 production process called Raman association is proposed that could have contributed to the formation of H_2 in the early universe. Raman association is a scattering process where background radiation scatters inelastically off two colliding hydrogen atoms, taking away kinetic energy. It is shown how to calculate the necessary properties (cross sections) to describe this process.

In Chapter 5 the results of Chapter 4 are used to calculate the rate of H_2 formation, which is then applied to an actual model of the early universe. It is shown that the Raman association process contributed significantly at some time (redshift factor $z \approx 1600$ or about 1.5×10^5 years), but the total contribution to H_2 production is minor compared to other processes such as the one initiated by $H + H^+$ collisions.

1.3.3   Nitrous oxide N_2O

The N_2O molecule is probably best known for its anaesthetic effects, or under its common name "laughing gas". It was first synthesized by Joseph Priestley in 1775 who recognized its anaesthetic properties[54].

Modern scientific interest in N_2O stems mainly from the fact that the N_2O molecule is an important constituent of the earth's atmosphere[44] and the estimate that N_2O is responsible for about 5% of the human induced greenhouse effect[55]. Atmospheric N_2O arises from both natural and human sources, the main human sources being agriculture, sewage treatment, burning of fossil fuels and various chemical industries. It is estimated that the atmospheric N_2O concentration has increased by about 16% since the start of the industrial revolution[56]. In the upper atmosphere, N_2O molecules can photodissociate under the influence of sunlight, yielding a highly reactive oxygen atom, and the chemically inert N_2 molecule.

The photodissociation processes that can take place in a molecule such as N_2O can be very complex. In principle, all information about the process can be obtained in the laboratory by breaking up the molecule with a laser, and determining the quantum states of the fragments. Such experiments are difficult however, and interpreting the lab data in terms of a dynamical model of the photodissociation process is far from easy. Thus, theoretical models have to be built to help interpret the lab data, and to gain a better understanding of the system. Based on that knowledge, more advanced experiments might be developed that challenge theory again.

In Chapter 6, we use N_2O as an example molecule to test a photodissociation model[57], wich has been applied on N_2O and various comparable molecular systems in the last few years[58,59]. Within this so-called long-range interaction model the distribution of quantum states (polarization) of the

emerging oxygen atom can be estimated. In order to check the model, in Chapter 6 a more advanced model of the N_2O molecule is developed, and detailed calculations have been performed in order to study the assumptions underlying the model. The current results indicate that some of the assumptions may not hold. In particular, the assumption that the behavior of the interaction potential at the point where the most important dynamical processes take place are of the analytical long-range form is not valid. However, the basic dynamical description of the model appears correct: the short-range dynamics mainly determine the outcome of the photodissociation process at relatively high photodissociation energies, even for the relatively sensitive polarization effects.

1.4   Notes on publications

Most of the work in this thesis has been accepted for publication in scientific journals. The publications are indicated at the beginning of each chapter. The full lists of authors can be found in the list of publications (p.115). Differences between published material and the thesis are pointed out here.

- Chapter 2: References to "the accompanying paper" are replaced by Greenslade *et al.*[60].

- Chapter 3: Numbers in Table 3.4, Table 3.5 and Fig. 3.4 differ slightly from the numbers in van der Loo and Groenenboom[61]. The changes are reported in an erratum, and do not alter the conclusions. The appendix to Chapter 3 was not published before.

- Chapter 5: The introduction and the discussion of the chemical rate equations is expanded. Figure 5.3 and a discussion have been added.

Ab initio calculation of (2+1) REMPI spectra and lifetimes of the $(D,3)^2\Sigma^-$ states of OH and OD

High-level *ab initio* potential energy curves and transition dipole moments for the OH $X^2\Pi$, $2^2\Pi$, $1^2\Sigma^-$, $D^2\Sigma^-$, $3^2\Sigma^-$, $A^2\Sigma^+$, $B^2\Sigma^+$, $1^2\Delta$, $1^4\Sigma^-$, and $1^4\Pi$ states are computed. The results are used to estimate the (2+1) resonance enhanced multiphoton ionization spectrum for the $(D,3)^2\Sigma^-(v') \xleftarrow{2h\nu} X^2\Pi(v'')$ transitions, which are compared with experiments by M. E. Greenslade *et al.*[60] . We use the discrete variable representation-absorbing boundary condition method to incorporate the effect of the dissociative intermediate $1^2\Sigma^-$ state. We obtain qualitative agreement with experiment for the line strengths. Radiative and predissociative decay rates of the Rydberg $(D,3)^2\Sigma^-$ states of OH and OD were computed, including spin-orbit coupling effects and the effect of spin-electronic and gyroscopic coupling. We show that the lifetime of the Rydberg $^2\Sigma^-$ states for rotationally cold molecules is limited mainly by predissociation caused by spin-orbit coupling.

2.1 Introduction

The first observation of the Rydberg $D^2\Sigma^-$ state of OH was reported by Douglas[62] in 1974, while the first theoretical potential energy curves of the $D^2\Sigma^-$ and $3^2\Sigma^-$ states were reported one year earlier by Easson and Price[63]. The Rydberg $D^2\Sigma^-$ and $3^2\Sigma^-$ states have been studied experimentally[64–66]

and theoretically[67–69] ever since by various authors. In 1983, van Dishoeck[67] *et al.* reported the first extensive theoretical description of the $D^2\Sigma^-$ state. The electronic assignments $D^2\Sigma^-(1\pi^2 3p\sigma)$ and $3^2\Sigma^-(1\pi^2 4s\sigma)$ are discussed by Stephens and McKoy[68]. The need for a good description of the ~ 10 eV energy region of OH/D for astrophysical applications has long since been recognized[50,70,71] and is still relevant today[72]. Recently a sensitive OH/D detection scheme based on the one-photon $D^2\Sigma^- \leftarrow X^2\Pi$ transition was proposed[66].

The present work was directly motivated by the recent two-photon resonant, resonance enhanced multiphoton ionization [(2+1)REMPI] experiments performed on rotationally cold, state selected $OH[X^2\Pi(v, J = |M_J| = |\Omega| = 3/2)]$ radicals by Greenslade *et al.*[60]. The purpose of our work is to explain why certain transitions were observed, and others not, and to estimate the absolute sensitivity of the experimental method. The lifetimes of the Rydberg $^2\Sigma^-$ states are still only estimated very crudely in various papers[64,66]. Here, we elucidate both radiative and nonradiative decay mechanisms of the Rydberg $^2\Sigma^-$ states to accurately estimate the lifetimes of these states for OH and OD.

In Sec. 2.2.1 we describe the calculation of a new set of potential energy curves and electronic transition dipole moments, computed at the multireference configuration interaction level, for all electronic states up to and including the $3^2\Sigma^-$ state (see Figs. 2.1 and 2.2). In order to describe the (2+1)REMPI spectrum, we derive in Sec. 2.2.2 a rate model that includes the two-photon excitation, the detection step, and the competition of the detection step with decay of the excited states. We use second-order perturbation theory (Sec. 2.2.2) to estimate the two-photon absorption cross sections and to compare the relative intensities for different vibronic transitions.

Since the experiment is performed on state-selected, aligned molecules, we also derive the equations that relate the two-photon absorption strength to the direction and polarization of the laser beam with respect to the (space-fixed) quantization axis of the total molecular angular momentum.

Calculating the $(D, 3)^2\Sigma^- \leftarrow X^2\Pi$ two-photon absorption absorption cross sections involves an integral over the nuclear states of the dissociative $1^2\Sigma^-$ state. In Sec. 2.2.2 we show how the discrete variable representation-absorbing boundary condition (DVR-ABC) method of Seideman and Miller[73–75] can be applied to treat this problem numerically. In Sec. 2.2.2 we discuss the calculation of the decay rates of rovibrational Rydberg $(D, 3)^2\Sigma^-$ states associated with several homogeneous and heterogeneous predissociation processes.

2.2   Theory

We describe the wave function in terms of eigenfunctions of the nonrelativistic molecular Hamiltonian $\hat{H}$:

$$\hat{H} = \hat{T}_{\text{nuc}} + \hat{H}_{\text{elec}}, \tag{2.1}$$

where $\hat{H}_{\text{elec}}$ represents the non-relativistic electronic Hamiltonian in the clamped-nuclei approximation and $\hat{T}_{\text{nuc}}$ is the nuclear kinetic energy operator, which can be written as the sum of a radial ($\hat{T}_{\text{r}}$) and a rotational part $\hat{H}_{\text{rot}}$:

$$\hat{T}_{\text{nuc}} = \hat{T}_{\text{r}} + \hat{H}_{\text{rot}} = \frac{-\hbar^2}{2\mu r} \frac{\partial^2}{\partial r^2} r + \frac{\hat{\mathbf{R}}^2}{2\mu r^2}, \tag{2.2}$$

where r is the internuclear distance, μ is the reduced mass of the system, and $\hat{\mathbf{R}} \equiv \hat{\mathbf{J}} - \hat{\mathbf{S}} - \hat{\mathbf{L}}$ describes the nuclear angular momentum operator acting on the polar angle β and the azimuthal angle α of the diatomic axis in the space-fixed frame. The operators $\hat{\mathbf{J}}$, $\hat{\mathbf{S}}$, and $\hat{\mathbf{L}}$ represent the total angular momentum apart from nuclear spin, the electronic spin, and the electronic orbital angular momentum, respectively. At low rotational levels, the Π states of OH/D approach the Hund's case (a) limit, while multiplets of Σ symmetry are formally pure Hund's case (b) states[76]. Since in this work we describe the OH/D molecule at only the lowest rotational levels, we use the pure case (a) description for Π states and the pure case (b) description for Σ states. The Hund's case (a) and (b) wave functions of parity p are given by:

$$|v; JM_J\Omega(L)\Lambda S\Sigma p\rangle = \frac{[1 + (-1)^p\, \hat{i}\,]}{\sqrt{(2 - \delta_{\Lambda 0}\delta_{\Sigma 0})}} \frac{\chi_v^a(r)}{r} |JM_J\Omega(L)\Lambda S\Sigma\rangle \tag{2.3}$$

$$|v; JM_J N(L)\Lambda S p\rangle = \frac{[1 + (-1)^p\, \hat{i}\,]}{\sqrt{(2 - \delta_{\Lambda 0})}} \frac{\chi_v^b(r)}{r} |JM_J N(L)\Lambda S\rangle, \tag{2.4}$$

where J, M_J, Ω, N, Λ, and S are the usual Hund's case (a), (b) quantum numbers[77]. The nuclear wave functions ($\chi_v^{a/b}$) are labeled with the vibrational quantum number v, which is replaced by the energy E for continuum states. The superscripts (a) and (b) represent all case (a) and case (b) quantum numbers. States with parity $(-1)^{J-\frac{1}{2}}$ and $(-1)^{J+\frac{1}{2}}$ are labeled by e and f, respectively. The electronic orbital angular momentum L is not a good quantum number. However, we use (L) to indicate its value in the atomic limit. We will also use the labels F_1 and F_2 to indicate Hund's case (b) states with $N = J + \frac{1}{2}$ and $N = J - \frac{1}{2}$, respectively. We use the phase conventions

defined in the appendix of van Vroonhoven and Groenenboom [78] to obtain the action of the inversion operator $\hat{i}$:

$$\hat{i}|JM_J\Omega(L)\Lambda S\Sigma\rangle = (-1)^{J+L-S}|JM_J-\Omega(L)-\Lambda S-\Sigma\rangle \tag{2.5}$$

$$\hat{i}|JM_JN(L)\Lambda S\rangle = (-1)^{N+L}|JM_JN(L)-\Lambda S\rangle. \tag{2.6}$$

The rotronic Hund's case (a) and (b) basis functions are given by:

$$|JM_J\Omega(L)\Lambda S\Sigma\rangle = \sqrt{[J]/4\pi}D^{(J)*}_{M,J\Omega}(\alpha,\beta,0)|(L)\Lambda S\Sigma\rangle \tag{2.7}$$

$$|JM_JN(L)\Lambda S\rangle = \sum_{M_N M_S}\sqrt{[N]/4\pi}D^{(N)*}_{M_N,\Lambda}(\alpha,\beta,0)|(L)\Lambda\rangle|SM_S\rangle$$
$$\times\langle NM_NSM_S|JM_J\rangle, \tag{2.8}$$

where $\sqrt{[N]/4\pi}D^{(N)*}_{M_N\Lambda}(\alpha,\beta,0)$ represents a two-angle normalized Wigner D-matrix and $[X] \equiv 2X + 1$.

2.2.1   Electronic structure calculations

Ab initio potential energy curves for the OH $X^2\Pi$, $2^2\Pi$, $1^2\Sigma^-$, $D^2\Sigma^-$, $3^2\Sigma^-$, $A^2\Sigma^+$, $B^2\Sigma^+$, $1^4\Sigma^-$, $1^4\Pi$, and $1^2\Delta$ states are computed with the `MOLPRO`[79] program package at the internally contracted multireference configuration interaction with single and double excitations[80,81] (MRCI) level. The molecular orbitals are obtained from state averaged complete active space self consistent field (SA-CASSCF) calculations[82,83]. We also computed the the Breit-Pauli[84] spin-orbit coupling and $\hat{L}_\pm$ matrix elements and the r-dependent electronic transition dipole moments at the SA-CASSCF+MRCI level. Details of the *ab initio* calculations are given in Table 2.1.

   All *ab initio* points are interpolated using cubic splines. To improve our ability to predict the position of unobserved vibrational levels, we also apply a linear scaling of the form

$$V_{\text{sc}}(r) = c_3V(r'), \quad r' = c_1 + c_2r, \tag{2.9}$$

to the potentials $V(r)$ of the $D^2\Sigma^-$ and $3^2\Sigma^-$ states. The scaling parameters c_1, c_2, and c_3 are obtained by a non-linear fitting procedure that minimizes the relative error in calculated vibrational spacings and rotational B_v constants. The $D^2\Sigma^-$ and $3^2\Sigma^-$ state curves are shifted to match the experimentally observed OH$[(D,3)^2\Sigma^-(v=0) \leftarrow X^2\Pi(v=0)]$ transition frequencies. The dissociative curves are shifted to match the atomic energies[87] at 10 a_0, and the $B^2\Sigma^+$ potential energy curve was shifted to match the experimental OH$[B^2\Sigma^+(v'=0) \leftarrow X^2\Pi(v''=7)]$ transitions as reported by Copeland *et al.*[88]

Table 2.1: Details of the *ab initio* electronic structure calculations.

State[a]	basis[b]	space[c]	SA-CASSF[d]
$X^2\Pi$	aV6Z	$5\sigma2\pi$	
$A^2\Sigma^+, 1^2\Sigma^-$	aV6Z	$5\sigma2\pi$	
$1^4\Sigma^-$	aV6Z	$6\sigma1\pi$	
$1^4\Pi$	aV6Z	$6\sigma1\pi$	
$1^2\Delta$	aV6Z	$5\sigma2\pi$	$1^2\Sigma^-(\frac{1}{4})$
$D^2\Sigma^-$	daV5Z	$6\sigma2\pi$	$1^2\Sigma^-, 1^2\Delta(\frac{1}{2}:\frac{1}{4})$
$3^2\Sigma^-$	daV5Z	$6\sigma2\pi$	$1^2\Delta, (1,D)^2\Sigma^-$
$2^2\Pi$	daV5Z	$5\sigma2\pi$	$X^2\Pi_{x,y}(\frac{1}{4})$
$B^2\Sigma^+$	daVTZ	$5\sigma2\pi$	$A^2\Sigma^+, 1^2\Delta$
$\langle X^2\Pi|\hat{\mathbf{d}}|1^2\Sigma^-\rangle$	aV6Z	$5\sigma2\pi$	
$\langle X^2\Pi|\hat{\mathbf{d}}|A^2\Sigma^+\rangle$	aV6Z	$5\sigma2\pi$	
$\langle 1^2\Sigma^-|\hat{\mathbf{d}}|D^2\Sigma^-\rangle$	daV5Z	$6\sigma1\pi$	$1^2\Delta$
$\langle 1^2\Sigma^-|\hat{\mathbf{d}}|3^2\Sigma^-\rangle$	daV5Z	$6\sigma1\pi$	$1^2\Delta, D^2\Sigma^-$
$\langle X^2\Pi|\hat{\mathbf{d}}|D^2\Sigma^-\rangle$	daV5Z	$6\sigma1\pi$	$1^2\Sigma^-, 1^2\Delta$
$\langle X^2\Pi|\hat{\mathbf{d}}|3^2\Sigma^-\rangle$	daV5Z	$6\sigma1\pi$	$1^2\Delta, (1,D)^2\Sigma^-$
$\langle 3^2\Sigma^-|\hat{\mathbf{d}}|D^2\Sigma^-\rangle$	daV5Z	$6\sigma2\pi$	$1^2\Sigma^-, 1^2\Delta$
$\langle (D,3)^2\Sigma^-|\hat{H}_{\mathrm{so}}|2^2\Pi\rangle$	daVTZ	$5\sigma1\pi$	$X^2\Pi_{x,y}, 1^2\Sigma^-, 1^2\Delta$
$\langle (D,3)^2\Sigma^-|\hat{H}_{\mathrm{so}}|B^2\Sigma^+\rangle$	daVTZ	$5\sigma1\pi$	$A^2\Sigma^+, 1^2\Sigma^-, 1^2\Delta$
$\langle (D,3)^2\Sigma^-|\hat{H}_{\mathrm{so}}|1^4\Pi\rangle$	daVTZ	$5\sigma1\pi$	$1^2\Sigma^-, 1^2\Delta$

[a] The electronic state or the matrix element. We used Davidson's correction[85] for the $(D,3)^2\Sigma^-$, $2^2\Pi$, and $B^2\Sigma^+$ states. The $L_\pm$ matrix elements are obtained from the same calculation as the spin orbit matrix elements.

[b] The one-electron basis sets are of the (doubly) augmented correlation consistent polarized valence triple-zeta, 5-zeta, or 6-zeta [(d)aV(T,5,6)Z] type[86]. For the spin orbit and $L_\pm$ matrix elements uncontracted basis sets are used.

[c] The active space used in the SA-CASSCF calculation: $n\sigma$ means that the $2\sigma - n\sigma$ orbitals are included (the 1σ orbital is kept doubly occupied in all calculations) and $n\pi$ means that the $1\pi_{x,y} - n\pi_{x,y}$ orbitals were used.

[d] States also included in the SA-CASSCF calculation. All states have equal weights unless otherwise indicated, states in the first column always have weight 1.

2.2.2 (2+1) REMPI

The use of rate models to describe the production and detection of ions in resonant multiphoton ionization processes is well established[89–93]. The (2+1) REMPI process as described in Greenslade *et al.*[60] may be summarized schematically as follows:

$$\text{OH} + 2h\nu \xrightarrow{k_1} \text{OH}^* \begin{array}{l} \xrightarrow{h\nu, k_2} \quad \text{OH}^+ \rightarrow \text{detector} \\ \xrightarrow{k_3} \quad \text{OH}, \text{O} + \text{H (decay)}. \end{array} \tag{2.10}$$
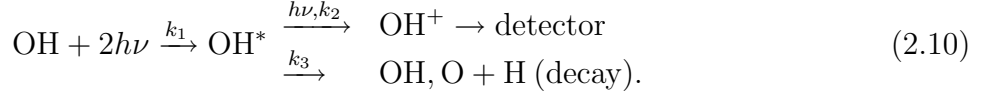
The state-selected OH molecule is first two-photon excited at rate k_1, after which it is either ionized (rate k_2) with a third photon and detected as OH^+, or it decays (rate k_3) and the molecule is lost for detection. The rate coefficients in s^{-1} are given by:

$$k_1 = g^{(2)}\sigma^{(2)}(\omega)[I/\hbar\omega]^2 \tag{2.11}$$
$$k_2 = \sigma_{\text{ion}}(\omega)I/\hbar\omega \tag{2.12}$$
$$k_3 = \tau_{\text{OH}^*}^{-1}, \tag{2.13}$$

where $\sigma^{(2)}$ is the generalized two-photon absorption cross section in cm^{4}s, I the laser intensity in W/cm^2, ω the laser angular frequency in s^{-1}, σ_{ion} the excited state ionization cross section in cm^2 and τ_{OH^*} the lifetime of the excited state in s. The coherence factor $g^{(2)}$ for two-photon absorption is 1 if the molecule is excited with coherent light and 2 for chaotic light[94,95]. We employ two extreme cases of this model to estimate the two-photon absorption strength. In the first extreme detection is very efficient, so we have $k_2 \gg k_3$ and the number of detected OH^+ molecules $\#[\text{OH}^+] \propto k_1$. In the other extreme, decay is faster than detection and we have $\#[\text{OH}^+] \propto k_1 k_3^{-1}$. We assume a constant measurement time for all observations and an abundance of OH-molecules in the molecular beam such that no saturation occurs. In the case of fast ionization we obtain

$$\#[\text{OH}^+] \propto g^{(2)}(I/\hbar\omega)^2\hat{\sigma}^{(2)}, \tag{2.14}$$

and in the case of fast decay:

$$\#[\text{OH}^+] \propto g^{(2)}(I/\hbar\omega)^2\tau_{\text{OH}^*}^{-1}\hat{\sigma}^{(2)}, \tag{2.15}$$

where $\hat{\sigma}^{(2)}$ is the integrated line cross section for two-photon absorption[96]:

$$\hat{\sigma}^{(2)} = \int \text{d}\omega\,\sigma^{(2)}(\omega). \tag{2.16}$$

Two-photon absorption

The generalized two-photon absorption cross section $\sigma_{fi}^{(2)}$ in rationalized MKS[97] units is given by[94,95,98,99]:

$$\sigma_{J'M_{J'}f;J''M_{J''}i}^{(2)}(\omega) = \frac{(2\pi)^3\alpha^2\omega^2}{e^4}S_{J'M_{J'}f;J''M_{J''}i}^{(2)}\delta(\omega_i - \omega_f + 2\omega), \quad (2.17)$$

where ω is the excitation angular frequency, α the fine-structure constant, and e the elementary charge. Labels i and f indicate initial and final quantum numbers v, Ω, L, Λ, S, and Σ for a Hund's case (a) function and v, N, L, Λ, and S for a Hund's case (b) function. Here, we suppress the parity label p. The two-photon line strength $S^{(2)}$ is given by:

$$S_{J'M_{J'}f;J''M_{J''}i}^{(2)} = \hbar^2 \lim_{\varepsilon\downarrow 0}\left|\sum_{E}\!\!\!\!\!\!\!\!\int \frac{\langle\psi_f^{J'M_{J'}}|\boldsymbol{\varepsilon}\cdot\hat{\boldsymbol{\mu}}|\psi_E\rangle\langle\psi_E|\boldsymbol{\varepsilon}\cdot\hat{\boldsymbol{\mu}}|\psi_i^{J''M_{J''}}\rangle}{E_{ph} + E_i - E + i\varepsilon/2}\right|^2, \quad (2.18)$$

where $E_{ph} = \hbar\omega$ is the one-photon energy. The complete set of intermediate states ψ_E includes both continuum (dissociative) states and discrete (bound) states. The symbol $\sum_{E}\!\!\!\!\!\!\int$ signifies the integration over the continuum intermediate states and a summation over the discrete intermediate states. We take the propagation direction of the molecular beam as the space-fixed z-axis. The laser polarization $\boldsymbol{\varepsilon}$ and the electronic dipole operator $\hat{\boldsymbol{\mu}}$ are defined in this frame. The spherical components of $\boldsymbol{\varepsilon}$ are given by

$$\varepsilon_q = \sum_p D_{qp}^{(1)*}(\phi,\theta,\chi)\tilde{\varepsilon}_p, \quad (2.19)$$

where (ϕ,θ,χ) are the zyz-Euler angles of the laser frame with respect to the space-fixed frame and $\tilde{\boldsymbol{\varepsilon}}$ is the polarization vector in the laser frame.

Applying the Wigner-Eckart theorem[77] and recoupling the angular momenta, we rewrite [Eq. (2.18)] as follows:

$$\sum_{E}\!\!\!\!\!\!\!\!\int \frac{\langle\psi_f^{J'M_{J'}}|\boldsymbol{\varepsilon}\cdot\hat{\boldsymbol{\mu}}|\psi_E\rangle\langle\psi_E|\boldsymbol{\varepsilon}\cdot\hat{\boldsymbol{\mu}}|\psi_i^{J''M_{J''}}\rangle}{E_{ph} + E_i - E + i\varepsilon/2}$$

$$= \sum_{Jkq}(-1)^{J''+M_{J''}}\sqrt{[k]}\mathcal{E}_q^{(k)}\left\{\begin{matrix} J'' & 1 & J \\ 1 & J' & k \end{matrix}\right\}$$

$$\times\begin{pmatrix} J' & k & J'' \\ -M_{J'} & -q & M_{J''} \end{pmatrix}\sum_{E}\!\!\!\!\!\!\!\!\int \frac{\langle\psi_f^{J'}||\hat{\mu}^{(1)}||\psi_E^J\rangle\langle\psi_E^J||\hat{\mu}^{(1)}||\psi_i^{J''}\rangle}{E_{ph} + E_i - E + i\varepsilon/2}, \quad (2.20)$$

where $\mathcal{E}^{(k)} = [\boldsymbol{\varepsilon}\otimes\boldsymbol{\varepsilon}]^{(k)}$ is the two-photon polarization tensor[77]. Since the $X^2\Pi$ ground state approaches the Hund's case (a) limit, we need both the

reduced matrix elements for a Hund's case (b)←(a) transition as well as the reduced matrix element for a Hund's case (b)←(b) transition. The Hund's case (b)←(a) reduced matrix element reads:

$$\langle \psi_b^J || \hat{\mu}^{(1)} || \psi_{a'}^{J'} \rangle = \langle \chi_v^b | \hat{d}_{\Lambda-\Lambda'}^{(1)} | \chi_{v'}^{a'} \rangle \delta_{SS'} (-1)^{2J} \sqrt{[N][J][J']}$$
$$\times \sum_{\Omega t} \begin{pmatrix} J & 1 & J' \\ -\Omega & t & \Omega' \end{pmatrix} \begin{pmatrix} J & S & N \\ -\Omega & \Sigma' & \Lambda \end{pmatrix}, \tag{2.21}$$

while the Hund's case (b)←(b) reduced matrix element is given by:

$$\langle \psi_b^J || \hat{\mu}^{(1)} || \psi_{b'}^{J'} \rangle = \langle \chi_v^b | \hat{d}_{\Lambda-\Lambda'}^{(1)}(r) | \chi_{v'}^{b'} \rangle \delta_{SS'} (-1)^{J'+S-\Lambda+1}$$
$$\times \sqrt{[N][N'][J][J']} \begin{Bmatrix} J & N & S \\ N' & J' & 1 \end{Bmatrix} \begin{pmatrix} N & 1 & N' \\ -\Lambda & \Lambda-\Lambda' & \Lambda' \end{pmatrix}. \tag{2.22}$$

The body-fixed dipole operator $\hat{\mathbf{d}}$ is implicitly defined by

$$\hat{\mu}_p^{(1)} = \sum_q D_{pq}^{(1)*}(\alpha, \beta, 0) \hat{d}_q^{(1)}. \tag{2.23}$$

Since the experiments described in Greenslade *et al.*[60] are performed on rotationally cold molecules, we neglect rotational effects on the radial wave functions in the calculation of the two-photon transition strengths. The dominant terms in the coherent sum are the states which are (nearly) resonant with the one-photon energy, so we estimate the relative two-photon line strength by taking into account the electronic states computed in this work. The optically allowed intermediate states are the $X^2\Pi$, $2^2\Pi$, $1^2\Sigma^-$, $D^2\Sigma^-$, and $3^2\Sigma^-$ states. We neglect the contributions of vibrational levels of the initial and final electronic states, as well as contributions of the $2^2\Pi$ state which has a small Frank-Condon overlap with the final states. The remaining two intermediate states $[(1^2\Sigma^-, D^2\Sigma^-)$ or $(1^2\Sigma^-, 3^2\Sigma^-)]$ are of $^2\Sigma^-$ symmetry, so the cross section factorizes in a radial factor $\sigma_{fi}^{(2)}$ and a dimensionless angular factor $\mathcal{S}$:

$$\sigma_{J'M_{J'}f;J''M_{J''}i}^{(2)}(\omega) = \sigma_{fi}^{(2)}(\omega) \mathcal{S}_{J''M_{J''}\Omega''\Lambda''}^{J'M_{J'}N'\Lambda'} \delta(\omega_i - \omega_f + 2\omega), \tag{2.24}$$

where $\sigma_{fi}^{(2)}(\omega)$ is found from Eqs. (2.17) to (2.24):

$$\sigma_{fi}^{(2)}(\omega) = \frac{\hbar^2 (2\pi)^2 \alpha^2 \omega^2}{e^4} \left| \sum_{Em} \frac{\langle \chi_{v'}^f | \hat{d}_{\Lambda'-\Lambda} | \chi_E^m \rangle \langle \chi_E^m | \hat{d}_{\Lambda-\Lambda''} | \chi_{v''}^i \rangle}{E_{ph} + E_{iv''} - E + i\varepsilon/2} \right|^2, \tag{2.25}$$

where we added the vibrational quantum numbers for clarity. The summation is over the vibrational levels of the $3^2\Sigma^-$ state for transition to the $D^2\Sigma^-$

state and vice versa, and the integration is over the $1^2\Sigma^-$ nuclear continuum. The angular factor for a Hund's case (b)$\leftarrow$(b)$\leftarrow$(a) two-photon transition can be written as:

$$
\begin{aligned}
\mathcal{S}_{J''M_{J''}\Omega''\Lambda''}^{J'M_{J'}N'\Lambda'} = [N'][J'][J''] & \Bigg| \sum_{JN} (-1)^\varphi [N][J] \\
& \times \sum_{kq} \sqrt{[k]} \mathcal{E}_{pq}^{(k)} \begin{pmatrix} J' & k & J'' \\ -M_{J'} & -q & M_{J''} \end{pmatrix} \begin{Bmatrix} J'' & 1 & J \\ 1 & J' & k \end{Bmatrix} \\
& \times \begin{Bmatrix} J' & N' & S \\ N & J & 1 \end{Bmatrix} \begin{pmatrix} N' & 1 & N \\ -\Lambda' & \Lambda'-\Lambda & \Lambda \end{pmatrix} \\
& \times \sum_{\Omega t} \begin{pmatrix} J & 1 & J'' \\ \Omega & t & \Omega'' \end{pmatrix} \begin{pmatrix} J & S & N \\ -\Omega & \Sigma'' & \Lambda \end{pmatrix} \Bigg|^2,
\end{aligned} \tag{2.26}
$$

where $\varphi = J'' + M_{J''} - J + S - \Lambda' + 1$.

Numerical treatment

The bound state nuclear wave functions are represented on a grid using the sinc-function discrete variable representation (sinc-DVR)[100,101]. The contributions of the optically active bound intermediate states to the two-photon transitions are computed using the relevant transition dipole moments depicted in Fig. 2.2. Summing over five vibrational levels of the intermediate Rydberg $^2\Sigma^-$ states converges the calculations. Evaluating the contribution of the dissociative $1^2\Sigma^-$ intermediate state poses two problems: first, there is an integral over nuclear states and second, the integrand is singular at the one-photon resonance. However, a numerical treatment is possible when the resolvent is rewritten as follows:

$$
\begin{aligned}
\hat{G}(E^*) = & \\
\int \mathrm{d}E \frac{|\chi_E^{1^2\Sigma^-}\rangle\langle\chi_E^{1^2\Sigma^-}|}{E^* - E + i\varepsilon/2} & = \lim_{\varepsilon\downarrow 0}[E^* - (T_\mathrm{r} + \hat{V}_{1^2\Sigma^-}) + i\varepsilon/2]^{-1}, \quad (2.27)
\end{aligned}
$$

where $\hat{G}$ is the Green operator, $E^* = E_{ph} + E_{iv''}$ and we used (neglecting spin-orbit coupling):

$$
[\hat{T}_\mathrm{r} + \hat{V}_{1^2\Sigma^-}]|\chi_E^{1^2\Sigma^-}\rangle = E|\chi_E^{1^2\Sigma^-}\rangle. \tag{2.28}
$$

The Green operator can be represented on a grid when we impose absorbing boundary conditions[73–75]. This is achieved by augmenting the potential $\hat{V}_{1^2\Sigma^-}$ with a negative imaginary potential, which is equivalent to replacing $\varepsilon/2$ by

an r-dependent function. Here, we choose the Woods-Saxon potential as a functional form:

$$\lim_{\varepsilon \downarrow 0} \varepsilon/2 \to \varepsilon(R) = \frac{2\lambda}{1 + \exp\left[(R_{\max} - R)/\eta\right]}, \tag{2.29}$$

where λ and $R_{\max}$ are parameters to be adjusted so that the artificial potential does not penetrate the physically relevant region, while η is adjusted so that no significant reflection off the imaginary potential takes place. In this work this is accomplished by setting $\lambda = 0.2 E_h$, $R_{\max} = 12 a_0$, and $\eta = 0.4 a_0$.

Decay Processes

The Rydberg $^2\Sigma^-$ states may decay radiatively to the $X^2\Pi$ and $1^2\Sigma^-$ states or through a radiationless process to the $2^2\Pi$, $B^2\Sigma^+$, or $1^4\Pi$ states. The Einstein A-coefficient in s^{-1} for a radiative transition is given by[94]:

$$A_{J'f;J''i}(\omega) = \frac{4\alpha\omega^3}{3c^2 e^2 [J'']} |\langle \psi_f^{J'} || \hat{\mu}^{(1)} || \psi_i^{J''} \rangle|^2, \tag{2.30}$$

where the reduced matrix element is given in Eqs. (2.21) and (2.22) for Hund's case (b)→(a) and Hund's case (b)→(b) transitions, respectively, and ω is the angular frequency of the emitted photon. The total radiative lifetime τ_r of a state $\psi_i^{J''}$ is given by

$$\tau_r^{-1} = \sum_f A_{fi} + \int dE\, A_{fi}(E)\rho(E), \tag{2.31}$$

where the summation is over all final discrete states and integration is over final continuum states, with $\rho(E)$ the density of final states at energy E. The integral over continuum states is approximated by $\sum_E A_{fi}(E)\Delta E$, where the energy step ΔE is determined by dividing the integration domain for each initial state into 100 integration steps.

Several perturbative processes cause the Rydberg $^2\Sigma^-$ states to predissociate. Here, we distinguish heterogeneous predissociation, caused by the gyroscopic coupling from the $\hat{\mathbf{J}} \cdot \hat{\mathbf{L}}$ operator, and homogeneous predissociation, caused by spin-electronic ($\hat{\mathbf{L}} \cdot \hat{\mathbf{S}}$) and spin-orbit coupling ($\hat{H}_{so}$).

The predissociation lifetime τ_{so} associated with spin-orbit coupling is given by:

$$\tau_{so}^{-1} = \frac{2\pi}{\hbar} \sum_f |\langle \psi_f^{JM_J} | \hat{H}_{so} | \psi_i^{JM_J} \rangle|^2, \tag{2.32}$$

where the summation runs over all permitted rotronic $B^2\Sigma^+$, $2^2\Pi$, and $1^4\Pi$ states. The calculation of the spin-orbit matrix elements $\langle f|\hat{H}_{\text{so}}|i\rangle$ is described in Sec. 2.2.1. These matrix elements are computed near the crossing of the two adiabatic Born-Oppenheimer potentials and are assumed constant. The spin-orbit coupling couples the Rydberg states with both the $1^4\Pi_{1/2}(\Lambda = 1, \Sigma = -\frac{1}{2})$ and the $1^4\Pi_{1/2}(\Lambda = -1, \Sigma = \frac{3}{2})$ states.

Since the $^2\Sigma^-$ and the $2^2\Pi$ Rydberg states dissociate adiabatically into different atomic limits, $\hat{L}_\pm$-type couplings between these states are asymptotically zero. However, in the bound region, the $\hat{L}_\pm$ operator has nonzero matrix elements so that spin-electronic and gyroscopic coupling contribute to the decay of the Rydberg $^2\Sigma^-$ states through the $2^2\Pi$ state. Calculation of these matrix elements is described in section 2.2.1. We take the matrix elements constant and compute them at a single point near the crossing of two states.

In order to accurately compute the bound state and dissociative wave functions, the adiabatic potential energy curves are augmented with the relevant centrifugal terms for Hund's case (a) or (b)[102]. Bound state wave functions are computed with the sinc-DVR method[100,101] and energy normalized dissociative wave functions are computed with the renormalized Numerov method with photodissociation boundary conditions[103].

The total lifetime τ is given by $\tau^{-1} = \tau_{\text{r}}^{-1} + \tau_{\text{so}}^{-1} + \tau_{\text{se}}^{-1} + \tau_{\text{gy}}^{-1}$, where τ_{se} and τ_{gy} are the lifetimes associated with spin-electronic and gyroscopic predissociation.

2.3 Results and Discussion

2.3.1 Electronic structure

Figure 2.1 depicts the potential energy curves computed in this work. The quality of the ground state curve is tested by comparing vibrational levels G_v and rotational constants B_v with recent experimental values by Colin *et al.*[104] and Mélen *et al.*[105] We find errors in G_v which are $< 0.1\%$ for $v = 0 \ldots 5$ and errors $< 0.2\%$ for $v = 6 \ldots 10$. The errors in B_v are $< 0.06\%$ for $v = 0 \ldots 8$ and $< 0.2\%$ for $v = 9$ and $v = 10$. The computed and available experimental values for the Rydberg $(D, 3)^2\Sigma^-$ states for OH and OD are shown in Table 2.2. The scaling parameters (c_1, c_2, c_3) [see Eq. (2.9)] obtained from the fit are $(1.2173 \times 10^{-4}, 0.99199, 1.006)$ for the $D^2\Sigma^-$ state and $(1.6856 \times 10^{-4}, 0.99515, 1.0065)$ for the $3^2\Sigma^-$ state. Although the potentials are changed only very little by these corrections, the improvement in calculated G_v and B_v is substantial. The relative errors for the $D^2\Sigma^-$ state

.

Table 2.2: Vibrational spacings G_v and rotational constants B_v for the OH/D Rydberg $^2\Sigma^-$ states (in cm^{-1}), computed with *ab initio* potentials, scaled *ab initio* potentials, and compared with experimental data of Greenslade *et al.* [60]

| OH		$G(v)$			B_v		
	v	*ab initio*	scaled	Exp.	*ab initio*	scaled	Exp.
	0	0	0	0	15.62	15.37	15.0
	1	2583.05	2570.80	2566	14.86	14.63	14.8
	2	5088.44	5064.70	5067	14.29	14.08	14.2
$D\,^2\Sigma^-$	3	7519.55	7486.56	7487	13.69	13.49	13.6
	4	9839.70	9799.37	-	13.10	12.92	-
	5	12054.94	12008.95	-	12.52	12.36	-
	0	0	0	0	14.83	14.69	14.9
$3\,^2\Sigma^-$	1	2643.48	2640.00	2640	14.43	14.30	14.1
	2	5171.56	5165.85	-	13.91	13.79	-
	3	7579.54	7572.85	-	13.35	13.23	-
	4	9864.45	9858.03	-	12.76	12.66	-
	5	12025.17	12020.22	-	12.17	12.08	-
OD							
	0	0	0		8.34	8.20	
	1	1902.15	1893.05		8.02	7.90	
$D\,^2\Sigma^-$	2	3750.35	3732.41		7.78	7.66	
	3	5573.35	5547.26		7.56	7.45	
	4	7346.96	7314.07		7.33	7.22	
	5	9064.85	9026.15		7.09	6.70	
	0	0	0		7.89	7.82	
$3\,^2\Sigma^-$	1	1944.55	1941.80		7.75	7.68	
	2	3830.53	3825.66		7.57	7.50	
	3	5655.03	5648.70		7.36	7.30	
	4	7416.20	7409.07		7.14	7.08	
	5	9112.11	9104.85		6.92	6.86	
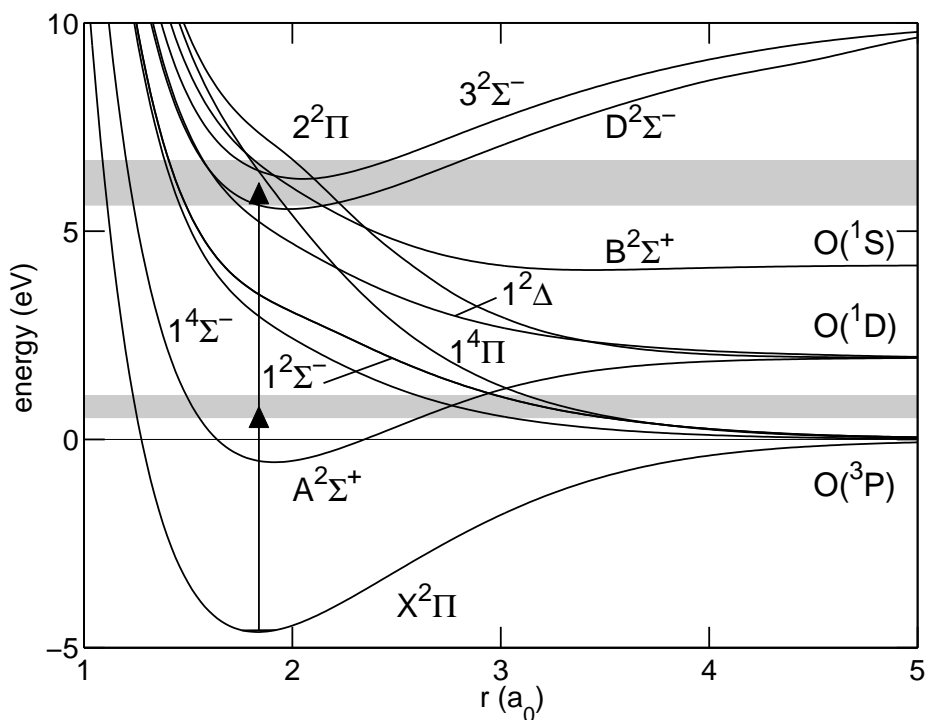
Figure 2.1: *Ab initio* potential energy curves for OH/D (in eV). The gray areas indicate the one-photon and two-photon energy range corresponding to the experiments in Greenslade *et al.* [60]

decrease by an order of magnitude to a mean deviation from the experimental G_v to $\sim 0.07\%$. The improvement in G_v and B_v for the $3^2\Sigma^-$ state is large, mainly because of the small number of experimental data available. This implies that extrapolation to $v \geq 2$ should be done with care.

In 1983 Van Dishoeck and Dalgarno [106] stated that the Rydberg $^2\Sigma^-$ states might predissociate through the $2^2\Pi$ or $B^2\Sigma^+$ states. Apart from these two, the $1^4\Pi$ potential energy curve also crosses with the $(D,3)^2\Sigma^-$ curves, which yields an extra predissociation process driven by spin-orbit coupling.

Figure 2.2 shows the r-dependent electronic transition dipole moments calculated in this work. The transition moments were obtained in separate calculations. We took care to have consistent relative signs since this is essential in the calculation of the two-photon absorption strength [Eq. (2.25)]. The most prominent feature in the structure of the transition moments that connect $D^2\Sigma^-$ and $3^2\Sigma^-$ states with other states or with each other are the drastic changes around $r = 1.5 - 3$ a_0.

Inspection of the coefficients of the most important configurations in the CI wave functions shows that the electronic structure of the $X^2\Pi$ and $1^2\Sigma^-$
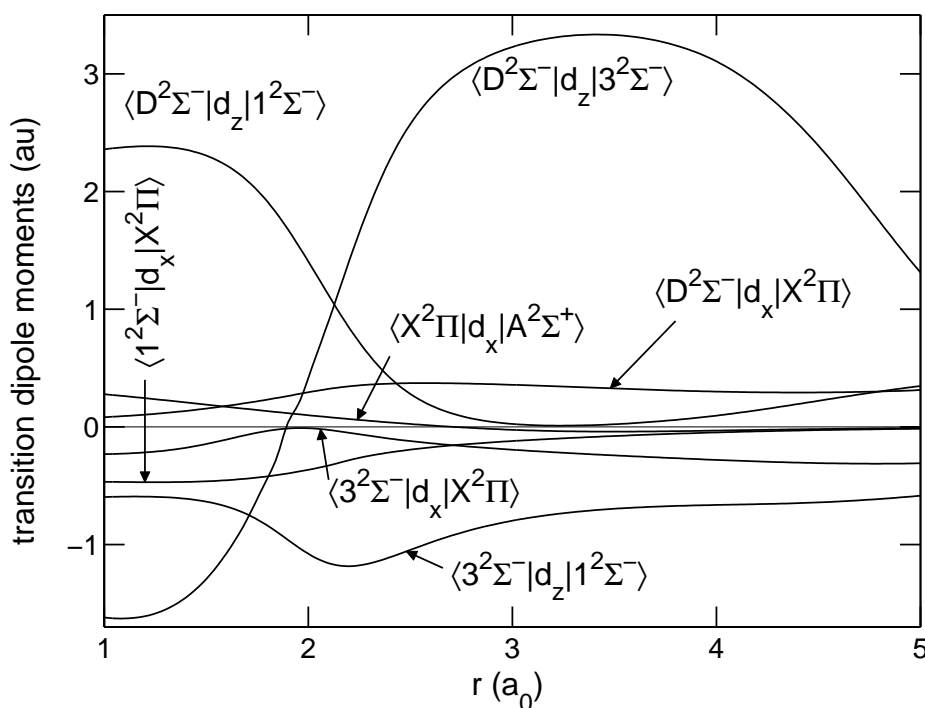
Figure 2.2: *Ab initio* Cartesian components of the electronic transition dipole operator for doublet states of OH/D (in au).

states do not vary significantly. However, the Rydberg $^2\Sigma^-$ states show a profound structure change.

Up to $r = 1.5$ a_0, the $D^2\Sigma^-$ state is mainly described as a $|\pi_x\pi_y5\bar{\sigma}|$ configuration. From 1.5 to 2.0 a_0 the contribution of the $|\pi_x\pi_y5\bar{\sigma}|$ configuration decreases sharply to about 50% of the initial value, while the contribution of the $|\pi_x\pi_y6\bar{\sigma}|$ configuration rises until it is the most important contribution, and the second most important contribution comes from the $|\pi_x\bar{\pi}_y6\sigma| + |\bar{\pi}_x\pi_y6\sigma|$ linear combination. For interatomic distances larger than 2 a_0 the situation reverses and around 3 a_0 the $D^2\Sigma^-$ state is again described almost exclusively by the $|\pi_x\pi_y5\bar{\sigma}|$ configuration. From 4 to 6 a_0 the coefficient of this configuration drops to zero and the doubly excited $|3\sigma\pi_x\pi_y4\bar{\sigma}5\bar{\sigma}|$ and $|3\sigma\pi_x\pi_y4\bar{\sigma}6\bar{\sigma}|$ configurations become the most important.

In the short range (1-1.5 a_0), the $3^2\Sigma^-$ state is almost completely described by the $|\pi_x\pi_y6\bar{\sigma}|$ configuration. The importance of this contribution decreases rapidly from 1.5 to 2.0 a_0, while the $|\pi_x\pi_y5\bar{\sigma}|$ and $|\bar{\pi}_x\pi_y5\sigma| + |\pi_x\bar{\pi}_y5\sigma|$ configurations rise in importance. From 2-3.5 a_0, the contribution of $|\pi_x\pi_y6\bar{\sigma}|$ increases, while the contribution of the $|\pi_x\pi_y6\bar{\sigma}|$ configuration decreases. At 3.5 a_0 the $3^2\Sigma^-$ state is described for $\sim 60\%$ by the $|\pi_x\pi_y6\bar{\sigma}|$
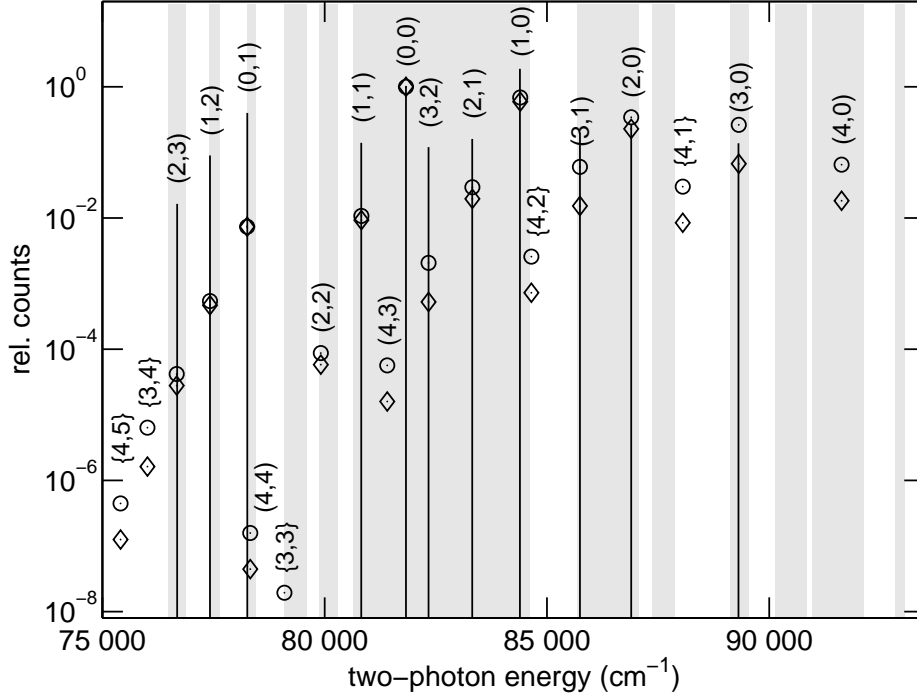
Figure 2.3: Experimental[108] and computed relative (2+1)REMPI intensities, scaled to the $(v', v'') = (0, 0)$ transition. The gray areas indicate scanned regions[108]. Sticks: experimental $S_1(1)$ lines for OH$[D^2\Sigma^-(v', J') \xleftarrow{2h\nu} X^2\Pi(v'', J'' = 3/2)]$ transitions, $\circ$: efficient detection, $\diamond$: rapid decay model, (v', v''): observed and calculated, $\{v', v''\}$: predicted but not scanned. The $(v', v'') = (3, 2)$ transition is marked "very weak" in the accompanying paper[60].

configuration and for $\sim 15\%$ by the $|\overline{\pi}_x \pi_y 5\sigma| + |\pi_x \pi_y 5\overline{\sigma}|$ configuration. From 3.5-6 a_0 the $|\pi_x \pi_y 5\overline{\sigma}|$ contribution increases at the cost of the $|\pi_x \pi_y 6\overline{\sigma}|$ configuration until it is slightly more important (35% against 30%).

All potential energy curves and transition dipole moments are made available through EPAPS[107].

2.3.2   (2+1) REMPI spectra

Figures 2.3 and 2.4 show the simulated and observed two-photon spectra for the $D^2\Sigma^-(v') \xleftarrow{2h\nu} X^2\Pi(v'')$ and $3^2\Sigma^-(v') \xleftarrow{2h\nu} X^2\Pi(v'')$ transitions, respectively. The sticks indicate the relative number of experimental OH$^+$ detector counts[108] for $^2\Sigma^-(v'J'F_1) \xleftarrow{2h\nu} X^2\Pi_{3/2}(v'', J'' = 3/2) \, S_1(1) \, (J' - J'' = 2)$ transitions. The circles and diamonds represent the fast ionization model [Eq. (2.14)] and the rapid decay case [Eq. (2.15)], respectively. Both experimental
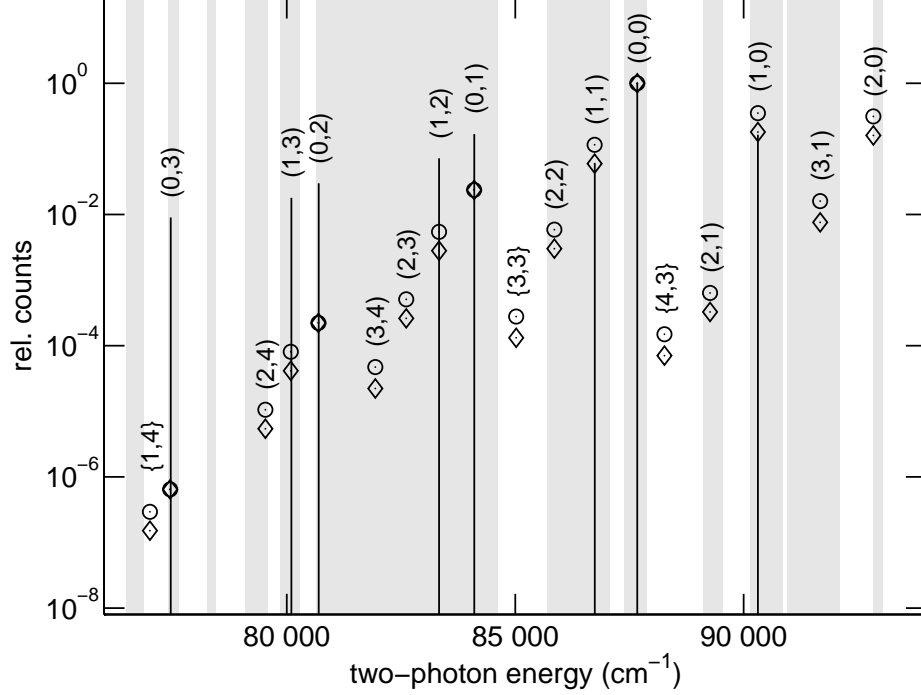
Figure 2.4: As in Fig. 2.3, but for the $OH[3^2\Sigma^-(v',J') \xleftarrow{2h\nu} X^2\Pi(J''=3/2,v'')]$ $S_1(1)$ transitions. The assignment of the $(v',v'')=(0,3)$ line was experimentally tentative due to an overlapping water line.[60]

and theoretical intensities were scaled relative to the $(v',v'')=(0,0)$ transitions. We find an integrated line cross section $\hat{\sigma}^{(2)} = \frac{1}{105} \times 0.27 \times 10^{-35}$ cm^4 for the $D^2\Sigma^-(v'=0) \leftarrow X^2\Pi_{3/2}(v''=0)$ transition and $\hat{\sigma}^{(2)} = \frac{1}{105} \times 0.17 \times 10^{-35}$ cm^4 for the $3^2\Sigma^-(v'=0) \leftarrow X^2\Pi_{3/2}(v''=0)$ transition, where the factor $\frac{1}{105}$ is the angular factor [Eq. (2.26), Table 2.3] for this transition. However, these numbers are crude estimates due to the limited number of intermediate states that were used. The gray areas in Figs. 2.3 and 2.4 indicate the wavelengths where actual scans have been performed[108]. Theoretically predicted transitions which lie outside of the scanned regions are indicated with curly brackets $\{v',v''\}$. In a previous combined experimental and theoretical study, where OH/D was produced in a similar way, we estimated the vibrational temperature to be around 1700K[109], so the spectrum is simulated at that temperature. The spectrum was simulated under the assumption that the experimental circumstances were constant throughout the spectrum. However, this is certainly not the case due to experimental difficulties such as

Table 2.3: Rotational factors $\mathcal{S}$ [Eq. (2.26)] for the $^2\Sigma^-(J') \xleftarrow{2h\nu} X^2\Pi_{3/2}(J'' = |M_{J''}| = 3/2, p'')$ transitions.

J''	p''	$O_1(1)$	$P_1(1)$	$Q_1(1)$	$R_1(1)$	$S_1(1)$
$\frac{3}{2}$	e	0	$\frac{1}{150}$	0	$\frac{9}{350}$	0
	f	0	0	$\frac{2}{75}$	0	$\frac{4}{525}$

deterioration of the dyes during measurement, the use of different dyes, variations in OH production and it's vibrational temperature, and variations in the alignment of the molecular beam with respect to the excitation laser[60,108]. This means that the relative experimental line strengths are order of magnitude estimates at best, so we only compare the line strengths locally. That is, we compare line strengths of transitions that are close in energy since we expect the effect of variations in experimental circumstances to be less important over short energy intervals.

We see in Fig. 2.3 that the calculated line strengths follow the trends in the observed line strengths very well. For instance, the observed increasing line strength for the $D^2\Sigma^-(v') \leftarrow X^2\Pi(v''), (v', v'') = (2, 3) - (1, 2) - (0, 1)$ transition series is predicted by both extremes of the rate model. Also, we see that all unobserved transitions that lie in scanned regions, have a lower predicted cross section than neighboring transitions that have been observed. For instance, the $(v', v'')=(4,4)$ and $(2,2)$ have much lower cross sections than the neighboring $(v', v'')=(0,1)$ and $(1, 1)$ transitions. Overall, for the $D^2\Sigma^- \xleftarrow{2h\nu} X^2\Pi$ transitions both models give equally good qualitative correspondence with experimental intensities.

For the $3^2\Sigma^- \xleftarrow{2h\nu} X^2\Pi$ transitions (Fig. 2.4) we see similar results: both extremes predict local trends equally well and we also find that unobserved transitions in scanned regions have much lower cross sections than observed ones.

In Table 2.3 we give the rotronic line strength factors $\mathcal{S}$ relevant for the $(D/3)^2\Sigma^-(J', F_1) \xleftarrow{2h\nu} X^2\Pi_{3/2}(J'' = 3/2, \mathrm{f})$ transitions. In the experimental setup (see[60]), a vertically polarized laser beam was put at a $90°$ angle with the molecular beam axis so we have $(\phi, \theta, \chi) = (0, \pi/2, 0)$ [See Eqs. (2.19-2.26)]. Furthermore, molecules were aligned with $|M_{J''}| = 3/2$ and we sum over $M_{J'}$ states. We obtain an intensity ratio for the $Q_1(1)/S_1(1)$ lines of $3\frac{1}{2}$. This is in good agreement with the experimentally observed ratios (based on the peak surface areas), which we estimated from Figs. 3 and 5 in Greenslade *et al.*[60] to be between about 2 and 4.
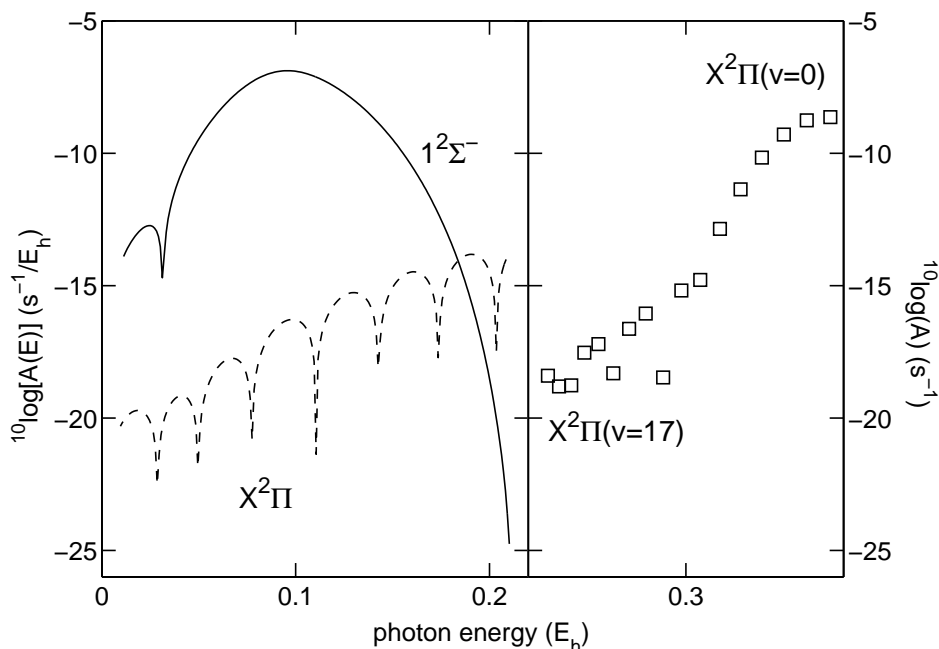
Figure 2.5: Einstein A-coefficients for radiation of the OH $D^2\Sigma^-(v=0)$ state to the dissociative $1^2\Sigma^-$, bound $X^2\Pi$, and dissociative $X^2\Pi$ states.

2.3.3 Lifetimes

Figure 2.5 shows the Einstein A-coefficients for the decay of the $D^2\Sigma^-(v=0)$ into different continuum and discrete states. The A-coefficient for decay into continuum states is in units of s^{-1}/E_h while the unit of A for transition to discrete states is s^{-1}. Hence, we may only compare the integral over the continuum A-coefficients with the bound-bound decay rates. As shown by Smith[110] and Allison *et al.*[111] for the case of photodissociation, the continuum A-coefficient for radiative decay into the $X^2\Pi$ state connects continuously with the discrete part if it is divided by the density of vibrational states at the threshold. However, since we also wish to compare radiative decay into the continua of two different electronic states ($1^2\Sigma^-$ and $X^2\Pi$), we do not follow this procedure here.

When radiating, the Rydberg $^2\Sigma^-$ states decay predominantly into the $1^2\Sigma^-$ state. A small contribution comes from the lower vibrational levels of the $X^2\Pi$ ground state, while the continuum plays no important role in decay of the $(D,3)^2\Sigma^-$ states. The patterns for the $D^2\Sigma^-$ and $3^2\Sigma^-$ state are much alike, albeit that for the $3^2\Sigma^-$ state, radiation into the $X^2\Pi$ vibrational levels is relatively less important than for the $D^2\Sigma^-$ state.

In Tables 2.4 and 2.5 we compare lifetimes of the Rydberg $^2\Sigma^-(J'' =$

Table 2.4: Lifetimes of the $OH(D,3)^2\Sigma^-(v, J = 3/2, F_1)$ states (τ), with the radiative (τ_r), the heterogeneous (gyroscopic) (τ_{he}), and the homogeneous (spin-orbit and spin-electronic) (τ_{ho}) contributions (in ns).

$D^2\Sigma^-(v)$	τ_r	$2^2\Pi$		$B^2\Sigma^+$	$1^4\Pi$	τ
		τ_{he}	τ_{ho}	τ_{ho}	τ_{ho}	
0	2.63	1.36	0.19	1.36	0.34	0.1024
1	2.88	3.00	0.39	430.01	0.18	0.1188
2	3.09	1.72	0.23	11.59	0.65	0.1537
3	3.28	4.03	0.56	6.23	3.43	0.4021
4	3.46	15.25	2.25	5.65	0.48	0.3635
$3^2\Sigma^-(v)$						
0	2.56	0.20	0.25	0.12	0.13	0.0397
1	2.03	0.98	0.69	0.10	73.42	0.0770
2	1.71	30.15	3.63	0.10	0.37	0.0773
3	1.47	28.44	22.41	0.11	0.32	0.0839

$3/2, F_1$) states associated with the several decay processes. In order to facilitate comparison with future experiments, we report predissociation and radiative lifetimes separately, and we distinguish the lifetime associated with heterogeneous processes $\tau_{he} = \tau_{gy}$ and that with homogeneous processes: $\tau_{ho}^{-1} = \tau_{so}^{-1} + \tau_{se}^{-1}$.

As first conjectured by Van Dishoeck[106], we find that predissociation is indeed the most important line-broadening effect. The $D^2\Sigma^-$ state predissociates mainly by spin-orbit coupling with the $2^2\Pi$ and $1^4\Pi$ states. Heterogeneous processes are less important at these low rotational levels. The $\hat{L}_\pm$ coupling matrix element is about 1 to 2 cm^{-1} in the bound region and thus contributes less than the spin-orbit coupling matrix elements which are about twice as large (see Table 2.6). The $3^2\Sigma^-$ state also predissociates into the $2^2\Pi$ and $1^4\Pi$ states, but because of a stronger spin-orbit coupling with the $B^2\Sigma^+$ state the lifetime of the $3^2\Sigma^-$ state is shorter than the lifetime of the $D^2\Sigma^-$ state.

The $2^2\Pi$, $B^2\Sigma^-$, and $1^4\Pi$ states correlate with O(^1D), O(^1S), and O(^3P), respectively. All states correlate with the H(^1S) limit. The lifetimes reported here could therefore be probed experimentally by measuring the $O(^1D,^1S,^3P)$ branching ratios.

There are no accurate measurements (yet) of the lifetime of the OH[$D^2\Sigma^-$ ($v'' = 0$)] state. McRaven *et al.*[66] reported an 8 ns upper limit based on the experimental laser pulse duration. De Beer *et al.*[64] "roughly estimate" the

Table 2.5: As in table 2.4, but for OD.

$D^2\Sigma^-(v)$	τ_r	$2^2\Pi$		$B^2\Sigma^+$	$1^4\Pi$	
		τ_he	τ_ho	τ_ho	τ_ho	τ
0	2.59	5.84	0.23	1.37	0.51	0.1382
1	2.78	4.34	0.17	14.82	0.13	0.0710
2	2.95	9.64	0.38	2.65	55.92	0.3189
3	3.10	432.08	13.52	2.55	0.26	0.2336
4	3.24	14.12	0.53	3.37	0.43	0.2179
$3^2\Sigma^-(v)$						
0	2.65	0.61	0.24	0.12	0.12	0.0437
1	2.21	10.18	0.92	0.08	1.73	0.0701
2	1.91	9.71	44.82	0.08	0.22	0.0583
3	1.69	2.86	4.05	0.09	0.47	0.0722

Table 2.6: Spin-orbit ($\langle f|\hat{H}_\mathrm{so}|i\rangle$) and $\langle f|\hat{L}_+|i\rangle$ coupling matrix elements relevant for predissociation of the Rydberg $^2\Sigma^-$ states. The matrix elements were computed at the crossing of the Rydberg states with the dissociative states.

$\langle f|$	$\langle f|\hat{H}_\mathrm{so}|^2\Sigma^-\rangle$ (cm^{-1})	
	$D^2\Sigma^-$	$3^2\Sigma^-$
$2^2\Pi$	4.50	2.50
$B^2\Sigma^+$	1.10	4.60
$1^4\Pi(\Sigma=\frac{3}{2})$	4.00	4.02
$\langle f|$	$\langle f|\hat{L}_+|^2\Sigma^-\rangle$ (E$_\mathrm{h}$)	
	$D^2\Sigma^-$	$3^2\Sigma^-$
$2^2\Pi$	0.048682	0.080789

lower lifetime limit to be $5 \times 10^{-10}[J(J+1)]^{-1}$, for the $D^2\Sigma^-(v = 0 \ldots 2)$ states, which yields about 31.75 ps for the $J = 3/2$ state. Here we find a lifetime of 102.4 ps which lies in between the current experimental limits, and within a factor of 3 from De Beer's estimate.

2.4 Summary and conclusions

We computed a new set of high-quality potential energy curves for OH/D, up to and including the Rydberg $3^2\Sigma^-$ state. Vibrational energy splittings and rotational constants for the $D^2\Sigma^-$ and $3^2\Sigma^-$ states based on these *ab initio* potentials show excellent agreement with experiment. The agreement is improved after a minor scaling of the potentials. We also report the vibrational constants G_v and rotational constants B_v for a set of unobserved levels and for the OD isotope. A new set of transition dipole moments for the doublet states of OH/D was computed and used in a calculation of the observed (2+1)REMPI spectra reported in Greenslade *et al.*[60]. To obtain the spectra, we include the effect of the $1^2\Sigma^-$ intermediate state by using the Seideman-Miller discrete variable representation-absorbing boundary condition method, which was originally derived for scattering and photodissociation calculations. The reason some transitions were scanned but not observed is that the two-photon cross section of these transitions is much lower than those of the observed transitions. Furthermore, relations were derived for the relative line strengths for aligned molecules at different experimental geometries and a good numerical agreement with experiment is obtained. We compute the radiative and predissociative lifetimes of the Rydberg $(D,3)^2\Sigma^-$ states including the effect of spin-orbit coupling, spin-electronic-, and gyroscopic predissociation. We find that predissociation occurs much faster than radiation, and we find the total lifetime of the $D^2\Sigma^-(v = 1, J = 3/2, F_1)$ state to be 102.4 ps, which lies in between currently known experimental limits.

Theoretical transition probabilities for the OH Meinel system

We present a new potential energy curve, electric dipole moment function, and spin-orbit coupling function for OH in the $X^2\Pi$ state, based on high-level *ab initio* calculations. These properties, combined with a spectroscopically parametrized lambda-type doubling Hamiltonian, are used to compute the Einstein A coefficients and photoabsorption cross sections for the OH Meinel transitions. We investigate the effect of spin-orbit coupling on the lifetimes of rovibrationally excited states. Comparing our results with earlier *ab initio* calculations, we conclude that our dipole moment and potential energy curve give the best agreement with experimental data to date. The results are made available *via* the EPAPS system.

3.1   Introduction

The emission lines arising from rovibrationally excited hydroxyl radicals in the electronic ground state were first identified in the late 1940's by Meinel[112] in the airglow emission spectrum of the night sky. The Meinel emission lines have been used as a tool to study many phenomena, including atmospheric temperature[113], chemical lifetime of atmospheric OH[114], atmospheric gravity waves[115–117], extraterrestrial atmospheres[118,119], and stellar oxygen abundance[120].

Recently, we took part in a project[121,122] where the lifetime of vibrationally excited OH was for the first time measured directly by electrostatically decelerating and trapping OH radicals in the excited $X^2\Pi[v = 1, J = 3/2, f(+)]$ state, and following the exponential decay in time. We computed the lifetime of excited OH based on a new *ab initio* dipole moment, took into account spin-orbit coupling and lambda-type doubling, and found good agreement with experiment. In the present work we extend our calculations to higher rovibrational levels, and investigate the effect of including OH bond length dependent spin-orbit coupling. We compare our dipole moment function with several earlier ones, and report a new set of Einstein A coefficients and photoabsorption cross sections for the OH Meinel system.

Experimentally, the emission rates are usually determined indirectly using nuclear wave functions computed from a parametrized potential, and an electric dipole moment function which is fitted so that relative emission rates arising from different excited levels are reproduced. The electric dipole moment function is generally expanded in powers of the interatomic distance $(r - r_e)^n$, where r_e is the equilibrium distance, and $n \geq 1$. Such a procedure was first followed by Shklovskii[123], Chaimberlain and Smith[124], and Kvifte[125]. They all took a linear dependence $(n = 1)$ for the electric dipole moment functions. Heaps and Hertzberg[126], and Wallace[127] used a quadratic function and Garvin *et al.*[128] a cubic function. In 1962, Ferguson and Parkingson[129] used a Morse potential, combined with experimental data from Krassovsky[130] to fit a fifth order polynomial for the electronic dipole moment function. Murphy[131] improved on this model in 1971 using new experimental data. From 1982 onwards, the standard emission rates in spectroscopic databases[132] were those reported by Gillis, Goldman, and Coxon[133–135], which were essentially based on a calculation by Mies[136]. In 1989, Turnbull and Lowe[137] reported emission rates based on a new empirical dipole moment function. However, it was recently noted by Cosby and Slanger[138], that the experimental data of Krassovsky *et al.*[139] underlying part of that fit is seriously flawed by modern standards. A new set of emission rates was published by Goldman *et al.*[140] in 1998, based on a Rydberg-Klein-Rees (RKR) potential of Nelson[141]. The dipole moment function was obtained by combining an experimentally determined electric dipole moment function of Nelson[142] with an *ab initio* dipole moment of Chackerian[140]. An empirical spin-orbit coupling function by Coxon and Foster[143] was also included in that calculation. It was recently pointed out by Cosby *et al.*[144] and Colin *et al.*[104] that the spectroscopic constants used to generate the energy levels in Goldman's calculations are flawed at higher vibrational $(v > 3)$ and rotational levels $(J > 19/2)$, producing difference with experiment up to 0.14 cm^{-1}. Both authors performed an improved fit of existing spectroscopic

data by Abrams *et al.*[145]. The main disadvantage of experimentally determined electric dipole moment functions is that the regions outside the range of experimentally probed internuclear distances are badly described. Thus, extrapolation to higher rovibrational levels, which probe larger and smaller interatomic distances, is hardly possible.

The first extensive *ab initio* calculation of emission rates was done by Mies[136], who used the electric dipole moment function of Stevens *et al.*[146] and an RKR potential of Albritton[136]. Extensive *ab initio* calculations of the electric dipole moment function of OH in the electronic ground state have been performed in the 1980's by Werner *et al.*[147] and Langhoff *et al.*[148,149]. In 1986, Langhoff, Werner, and Rosmus[150] reported theoretical emission coefficients which were computed using a shifted version of the dipole moment function of Werner[147]. Nuclear wave functions were computed using an RKR potential, extended with *ab initio* calculations to describe the potential at large internuclear separations, and the Hill and van Vleck approximation was applied[151] to compute the transition probabilities. In all *ab initio* calculations and experimental fits mentioned here, the lambda-type doubling was neglected. Spin-orbit coupling effects were based on spectroscopic data and taken independent of the OH-distance, except in the calculation by Goldman *et al.*[140].

3.2 Theory

3.2.1 Hamiltonian and basis functions

The nuclear Hamiltonian for the OH molecule in the $X^2\Pi$ state can be written as:

$$H = \frac{-\hbar^2}{2\mu r} \frac{\partial^2}{\partial r^2} r + T_{\text{rot}} + V(r) + H_{\text{so}}(r) + H_\Lambda, \tag{3.1}$$

where the first term is the radial part of the nuclear kinetic energy operator with r the internuclear distance, μ is the reduced mass, and T_{rot} is the rotational Hamiltonian for OH in the $X^2\Pi$ state:

$$T_{\text{rot}} = \frac{1}{2\mu r^2} \left[\mathbf{J}^2 + \mathbf{S}^2 + L_z(2S_z + L_z) - 2J_z(S_z + L_z) \right. $$
$$\left. - (J_-S_+ + J_+S_-) \right], \tag{3.2}$$

where $\mathbf{J}$ is the total angular momentum operator apart from nuclear spin, L_z the body-fixed z-component of the electronic orbital angular momentum operator $\mathbf{L}$, and $\mathbf{S}$ is the the electronic spin operator. The full rotation

Hamiltonian [given by $(\mathbf{J}-\mathbf{L}-\mathbf{S})^2$] also contains terms that couple the $X^2\Pi$ state with Δ and Σ states. These contributions are treated by the effective lambda-type doubling Hamiltonian H_Λ, in the unique perturber approximation[152,153]. The third term in Eq. (3.1) is the electronic potential energy curve in the clamped-nuclei approximation and $H_{\mathrm{so}}(r)$ is the r-dependent spin-orbit coupling operator.

We represent the Hamiltonian in a Hund's case (a) basis with basis functions:

$$|JM_J\,{}^2\Pi_{|\Omega|}p\rangle = \tfrac{1}{\sqrt{2}}[|JM_J\,{}^2\Pi_\Omega\rangle + \eta(-1)^{J-S}|JM_J\,{}^2\Pi_{-\Omega}\rangle], \qquad (3.3)$$

where

$$|JM_J\,{}^2\Pi_\Omega\rangle = \sqrt{\frac{2J+1}{4\pi}}D^{(J)*}_{M_J\Omega}(\alpha,\beta,0)|{}^2\Pi_\Omega\rangle. \qquad (3.4)$$

Here, J is the total angular momentum quantum number, M_J the projection of $\mathbf{J}$ on the laboratory-frame Z-axis, $\Omega = \pm 1/2, \pm 3/2$ the total electronic angular momentum projection on the molecular axis, and $\eta = \pm 1$ is the eigenvalue of the parity operator. We also introduce here the spectroscopic parity $p = \eta(-1)^{J-S}$, and we label wave functions with parity e or f for $p = 1$ or $p = -1$, respectively. Furthermore, $\sqrt{(2J+1)/4\pi}D^{(J)*}_{M_J\Omega}(\alpha,\beta,0)$ is a two-angle normalized Wigner D function, and $|{}^2\Pi_\Omega\rangle$ denotes the electronic basis functions.

Spin-orbit coupling lifts the degeneracy of states with different $|\Omega|$. The transition probabilities depend on spin-orbit coupling because it affects the rovibronic energy level structure of the molecule and alters the shape of the nuclear vibrational wave functions. Spin-orbit coupling can be taken into account, either by computing the electronic expectation values of the r-dependent spin-orbit coupling operator $\hat{H}_{\mathrm{so}}(r)$, or by using a parametrized Hamiltonian matrix in the Hund's case (a) basis, of which the matrix elements $H^{\mathrm{so}}_{|\Omega|,|\Omega'|}$ are given by[153]:

$$H^{\mathrm{so}}_{3/2,3/2} = \frac{A_v}{2} + \frac{A_{D_v}}{2}(z-1) + \frac{A_{H_v}}{4}[3(z-1)^2+z] \qquad (3.5)$$

$$H^{\mathrm{so}}_{1/2,3/2} = \frac{z^{1/2}}{2}A_{H_v} \qquad (3.6)$$

$$H^{\mathrm{so}}_{1/2,1/2} = -\frac{A_v}{2} + -\frac{A_{D_v}}{2}(z+1) + \frac{A_{H_v}}{4}[3(z+1)^2+z], \qquad (3.7)$$

where $z = (J+1/2)^2 - 1$ and the A_n are spectroscopic constants, given in Table 3.1. The spectroscopic spin-orbit Hamiltonian of Eq. (3.7) reproduces

the energy level structure, but does not affect the shape of nuclear wave functions, since terms dependent on r are averaged out. Thus, the Frank-Condon overlap between different nuclear states is affected when Eqs. (3.5)-(3.7) are used in stead of the r-dependent spin-orbit coupling. The calculation of the r dependent spin-orbit coupling is described in section 3.2.2.

The lambda-type doubling Hamiltonian lifts the degeneracy of states with different parity, and it is parametrized by spectroscopic constants. Its matrix elements $H^\Lambda_{|\Omega|,|\Omega'|}$ are given by[153]:

$$H^\Lambda_{3/2,3/2} = \frac{z}{2}\left[q_v + x(q_{D_v} + xq_{H_v})\right] \tag{3.8}$$

$$H^\Lambda_{1/2,3/2} = z^{1/2}\left\{\frac{1 \mp (J+1/2)}{2}\left[q_v + x(q_{D_v} + xq_{H_v})\right] + \frac{1}{4}(p_v + xp_{D_v})\right\} \tag{3.9}$$

$$H^\Lambda_{1/2,1/2} = \frac{z + 2 \mp 2(J+1/2)}{2}\left[q_v + x(q_{D_v} + xq_{H_v})\right] + \frac{1 \mp (J+1/2)}{2}(p_v + x)$$
$$+ \frac{A_v(p_v + xp_{D_v})}{8B_v}, \tag{3.10}$$

where p_v and q_v are lambda-type doubling constants, B_v rotational constants and $x = J(J+1)$. When two signs are given, the upper sign refers to e-states and the lower sign to f-states. We note that the last term in Eq. (3.10) is often labeled o_v.

3.2.2 Electronic structure and nuclear wave functions

The calculation of the electronic Born-Oppenheimer potential with the `MOLPRO`[79] program package was described earlier by us[155]. Briefly, the electronic wave functions are obtained from an internally contracted multi-reference configuration interaction calculation with single and double excitations (MRS-DCI)[80,81]. The orbitals were obtained from a complete active space self consistent field[82,83] (CASSCF) calculation with an extended active space consisting of five σ, two π_x, and two π_y orbitals, obtained from a large (aug-cc-pV6Z) one-electron basis set of Dunning[86]. Although our potential energy curve already gives accurate vibrational transition frequencies, with deviations from experiment on the order of 0.1%, we decided to further increase the accuracy by replacing the potential with a scaled potential $V_{sc}(r)$ given by

$$V_{sc}(r) = c_3 V(c_0 + c_1 r + c_2 r^2). \tag{3.11}$$

Here, c_1, c_2, and c_3 are nonlinear scaling parameters, fitted to minimize the difference between the experimental and calculated vibrational levels G_v.

Table 3.1: Spectroscopic constants[154] in cm^{-1} used in this work, see Eqs. (3.5)-(3.13).

v	A	$10^4 A_D$	$10^5 A_H$	B	q	$10^4 q_D$	$10^8 q_H$	p	$10^4 p_D$
0	-139.2729	-3.1626	-0.0285	18.550404	-0.038770	0.14693	-0.24306	0.235608	-0.2483
1	-139.5410	-2.8334	-0.0275	17.838640	-0.037013	0.14385	-0.22756	0.225097	-0.2548
2	-139.8057	-2.4002	-0.0285	17.136383	-0.035254	0.14181	-0.22578	0.214261	-0.2555
3	-140.0608	-1.9303	-0.0248	16.440990	-0.033471	0.13999	-0.22273	0.203253	-0.2604
4	-140.2964	-1.5181	-0.0255	15.749203	-0.031653	0.13811	-0.19475	0.191693	-0.2684
5	-140.4982	-1.1026	-0.0247	15.056955	-0.029763	0.13396	-0.10096	0.179474	-0.2806
6	-140.6433	-0.3809	-0.0238	14.359026	-0.027833	0.13435	-0.07881	0.166648	-0.3187
7	-140.6984	0.4120	-0.0230	13.648656	-0.025786	0.13308	0.00000	0.152240	-0.3574
8	-140.6137	2.4558	-0.0222	12.917024	-0.023621	0.13683	0.00000	0.136138	-0.4360
9	-140.3060	5.8954	-0.0214	12.152199	-0.021267	0.14147	0.00000	0.117007	-0.5361
10	-139.6458	11.7745	-0.0206	11.337856	-0.018522	0.12778	0.00000	0.093326	-0.6915

Since the vibrational levels are not sensitive to the position of the minimum of the potential, r_e, we introduce a shift c_0 so that r_e matches the experimentally determined value[154] of 1.8324 a_0. This method ensures that high quality nuclear wave functions are obtained for all rotational levels.

We compute the dipole moment as the expectation value of the electronic dipole operator for the MRSDCI wave functions. The r-dependent spin-orbit coupling is obtained as the expectation value of the Breit-Pauli spin-orbit Hamiltonian, using wave functions obtained from MRSDCI calculations. The orbitals were obtained from a CASSCF calculation, using the aug-cc-pVQZ one-electron basis set and an active space formed by one π_x, one π_y, and six σ orbitals. The potential energy curve, spin-orbit coupling, and electric dipole moment function are computed at 30 points ranging from 1 to 16 a_0, and are made available *via* the EPAPS[156] system.

The potential energy curve and electronic properties are interpolated using the reproducing kernel Hilbert space method[157] on an equidistant grid of 751 points between 1 and 16 a_0. The nuclear wave functions are obtained with the sinc-function DVR method[100,101] employing this grid. The lambda-type doubling Hamiltonian is parametrized separately for every vibrational, rotational, and parity level, so we compute a new Hamiltonian matrix for every rovibrational- and parity level. Furthermore, since the rotational and lambda-type doubling part of the Hamiltonian couple states of different Ω, the dimension of each Hamiltonian matrix doubles to 1502. After each diagonalization, 34 (17 for each Ω) or less bound state eigenfunctions are obtained. Only two of the eigenfunctions correspond to the rovibronic level for which the Hamiltonian was set up. These can be written as:

$$|\psi_{vF_np}^{JM_J}\rangle = \sum_{|\Omega|} r^{-1} f_{vF_np}^{J|\Omega|}(r)|JM_J{}^2\Pi_{|\Omega|}p\rangle, \tag{3.12}$$

where the $r^{-1}f_{vF_np}^{\Omega}(r)$ are the vibrational wave functions. The functions $|\psi_{vF_np}^{JM_J}\rangle$ are linear combinations of states with $|\Omega| = 3/2$ and $|\Omega| = 1/2$, such that, especially for higher rotational levels, Ω is not a good quantum number anymore. However, in the low-J limit, Ω is an approximately good quantum number, and a wave function is labeled with F_1 when it corresponds to $|\Omega| = 3/2$ and with F_2 when it corresponds with $|\Omega| = 1/2$.

3.2.3   Line intensities and Einstein A-coefficients

The line intensity $S_{\mathbf{ul}}(T)$ in cm^2/(s·molecule) for a photoabsorption transition $|\mathbf{u}\rangle \leftarrow |\mathbf{l}\rangle$ from a lower state $|\mathbf{l}\rangle$ to an upper state $|\mathbf{u}\rangle$ is given by[132]:

$$S_{\mathbf{ul}}(T) = \frac{e^{-E_{\mathbf{l}}/k_{\mathrm{b}}T} - e^{-E_{\mathbf{u}}/k_{\mathrm{b}}T}}{Q(T)} I_a g_{\mathbf{l}} \bar{\sigma}_{\mathbf{ul}}(\omega_0). \tag{3.13}$$

Here, the exponentials are Boltzmann factors for lower and upper states at temperature T, $Q(T)$ is the molecular partition function, $g_{\mathbf{l}}$ the degeneracy of the lower state, and $I_a = 0.997473$ the ^{16}OH isotope abundance. The transitions are labeled with $\mathbf{u}$ and $\mathbf{l}$, which denote the set of quantum numbers in upper and lower state that are resolved in experiment or calculation. Here, we have $\mathbf{u} = \{v, J, F_n, p\}$ and $\mathbf{l} = \{v', J', F_{n'}, p'\}$. The integrated line photoabsorption cross section $\bar{\sigma}(\omega_0)$ (cm^2/s) at the angular transition frequency ω_0 (s^{-1}) is given by

$$\bar{\sigma}_{\mathbf{ul}}(\omega_0) = \frac{4\pi^2 \alpha \omega_0}{(2J'+1)e^2} \sum_{M_J M_{J'}} |\langle \psi_{vF_np}^{JM_J} | \boldsymbol{\varepsilon} \cdot \boldsymbol{\mu} | \psi_{v'F_{n'}p'}^{J'M_{J'}} \rangle|^2, \tag{3.14}$$

where we average over lower, and sum over upper degenerate states. Furthermore, α is the fine-structure constant, e the elementary charge, $\boldsymbol{\varepsilon}$ the photon polarization vector and $\boldsymbol{\mu}$ the electronic dipole operator given by $\mu_q^{(1)} = \sum_t d_t^{(1)} D_{qt}^{(1)*}(\alpha, \beta, 0)$, where $\mathbf{d}$ is the electronic dipole operator in the molecular frame. Choosing the laboratory Z-axis along the photon polarization, integrating over angles α and β, and completing the sum over M_J and $M_{J'}$, gives

$$\bar{\sigma}_{\mathbf{ul}}(\omega_0) = \frac{4\pi^2 \alpha \omega_0}{3(2J'+1)e^2} |\langle \psi_{vF_np}^{J} || d^{(1)} || \psi_{v'F_{n'}p'}^{J'} \rangle|^2, \tag{3.15}$$

where the reduced matrix element reads

$$\langle \psi_{vF_np}^{J} || d^{(1)} || \psi_{v'F_{n'}p'}^{J'} \rangle =$$
$$(2J+1)^{1/2} \sum_{\Omega=1/2,3/2} \langle J\Omega 10 | J'\Omega \rangle \langle f_{vF_np}^{J|\Omega|} | d_0^{(1)} | f_{v'F_{n'}p'}^{J'|\Omega|} \rangle_r. \tag{3.16}$$

The Einstein A coefficient in s^{-1} for the spontaneous emission process $|\mathbf{u}\rangle \rightarrow |\mathbf{l}\rangle$ is connected to the line intensity by

$$S_{\mathbf{ul}}(T) = \frac{e^{-E_{\mathbf{l}}/k_{\mathrm{b}}T} - e^{-E_{\mathbf{u}}/k_{\mathrm{b}}T}}{Q(T)} \frac{I_a \pi^2 c^2 g_{\mathbf{u}}}{\omega_0^2} A_{\mathbf{ul}}, \tag{3.17}$$

where c is the speed of light, and it follows that $A_{\mathbf{ul}}$ is given by

$$A_{\mathbf{ul}} = \frac{2J' + 1}{2J + 1} \frac{\omega_0^2}{c^2 \pi^2} \bar{\sigma}_{\mathbf{ul}}(\omega_0). \tag{3.18}$$

The radiative lifetime $\tau_{\mathbf{u}}$ (in s) of an upper state $|\mathbf{u}\rangle$ reads

$$\tau_{\mathbf{u}}^{-1} = \sum_{\mathbf{l}} A_{\mathbf{ul}}, \tag{3.19}$$

where the sum is over al states $|\mathbf{l}\rangle$ with $E_{\mathbf{l}} < E_{\mathbf{u}}$. Finally, we note that line strengths S are often given in $\mathrm{cm}^2/(\mathrm{cm} \cdot \mathrm{molecule})$, in stead of $\mathrm{cm}^2/(\mathrm{s} \cdot \mathrm{molecule})$. In that case ω_0 in Eqs. (3.13) and (3.14) must be replaced by the wave number ν_0 given by: $\nu_0 = \omega_0/(100 \cdot 2\pi c)$.

3.3 Results

3.3.1 Potential energy curve

In Table 3.2, the computed and experimental vibrational band origins G_v are shown. The coefficients we found for the scaling procedure [see Eq. (3.11)] are shown in Table 3.3. Even though the scaling has a small effect on the shape of the potential [the case of no scaling is equivalent to coefficients $(c_0, c_1, c_2, c_3) = (0, 1, 0, 1)$], the reduction in error is large. The relative errors are reduced by at least two orders of magnitude with respect to the fully *ab initio* potential, yielding relative errors on the order of 10^{-5} or less. The difference between experimental and computed vibrational levels is $0.14 \ \mathrm{cm}^{-1}$ for $v = 1$, and less than $0.07 \ \mathrm{cm}^{-1}$ for $v = 2 \ldots 10$. This is about an order of magnitude more accurate than the vibrational levels computed by Langhoff *et al.*[148] who used the RKR potential of Coxon and Foster[158], extended with a scaled *ab initio* potential to describe the potential at large interatomic separations. In total, we find 17 bound vibrational levels, where Langhoff *et al.* find 16. Our *ab initio* potential energy curve has an r_e value of 1.8334 a_0, which differs only by $9.8 \times 10^{-3} \ a_0$ from the experimental value[154] of 1.8324 a_0 After fitting c_1, c_2, and c_3, but keeping $c_0 = 0$, the potential has a slightly shifted r_e value of 1.8314 a_0, yielding a c_0 value of $-1.0 \times 10^{-3} \ a_0$.

3.3.2 Dipole moment function

In Fig. 3.1, five dipole moment functions from the literature are compared with ours. The dipole moment functions are in general very similar except in the outer regions where the fitted curves of Murphy[131] and Nelson[142] decrease

Table 3.2: Experimental and computed vibrational energy levels G_v in cm^{-1}. Computed results are shown for the scaled potential $V_{sc}(r)$ [see Eq. (3.11)] and for the original *ab initio* potential $V(r)$. The coefficients are given in Table 3.3.

v	Exp. G_v[154]	*ab initio* G_v	err. %	scaled G_v	err. %
0	0	0	0	0.	0
1	3569.6415	3573.2426	0.101	3569.4944	-4.121×10^{-3}
2	6973.6790	6981.1031	0.107	6973.6800	1.501×10^{-5}
3	10214.0371	10225.0300	0.108	10214.0972	5.884×10^{-4}
4	13291.8106	13305.9995	0.107	13291.8158	3.873×10^{-5}
5	16207.1007	16224.1848	0.105	16207.1571	3.477×10^{-4}
6	18958.7928	18978.0894	0.102	18958.7717	-1.114×10^{-4}
7	21544.2632	21565.0051	0.096	21544.1885	-3.468×10^{-4}
8	23958.9883	23980.2775	0.089	23959.0303	1.754×10^{-3}
9	26196.0203	26216.2050	0.077	26196.0135	-2.607×10^{-5}
10	28245.2835	28262.3640	0.060	28245.2872	1.308×10^{-5}

Table 3.3: Coefficients for the scaled potential $V_{sc}(r)$ in Eq. (3.11).

	scaling constants
c_0	$-9.84300000 \times 10^{-4}$
c_1	1.00512315
c_2	$-2.20223846 \times 10^{-3}$
c_3	1.00389925

too fast as a function of r. This is a consequence of the functional form used to determine these functions: a fifth order polynomial for Murphy's, and a third order polynomial for Nelson's electric dipole moment function. Nelson *et al.* state that their electric dipole moment function is valid between 1.32 and 3.33 a_0, the classical turning points of the $v = 9$ level. The dipole moment computed in this work follows Nelson's empirical function most closely in the inner region. This is shown more clearly in Fig. 3.2, where we plot the difference between Nelson's dipole moment function and a number of *ab initio* computed functions. It can be seen that in the inner region, both the dipole moments by Langhoff and by Werner cross the empirical function, whereas ours remains slightly above the empirical one. Using a cubic spline
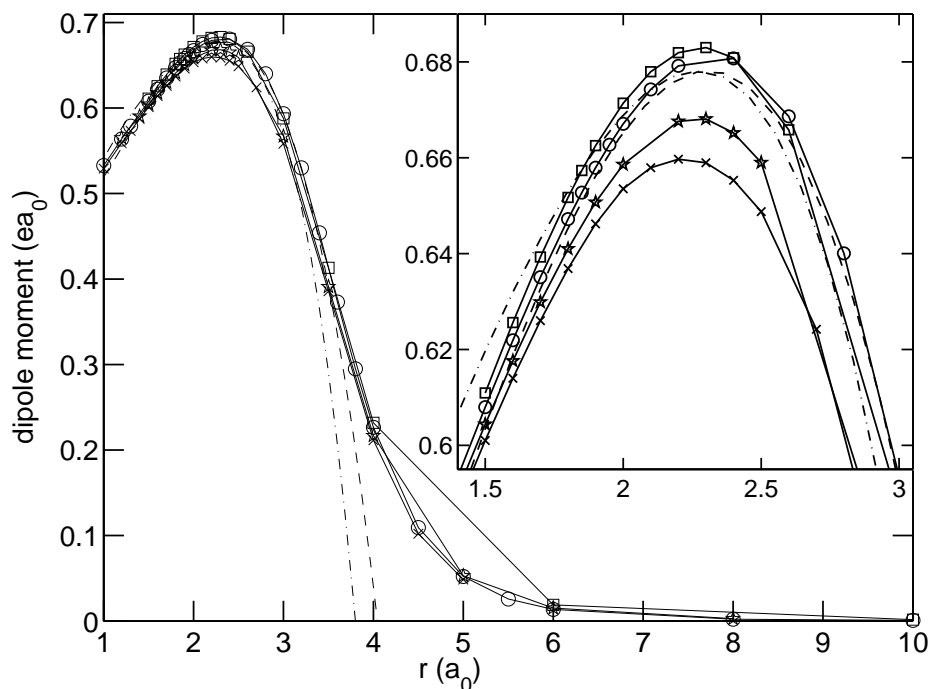
Figure 3.1: Dipole moment functions of OH compared. *Ab initio* points are connected here by straight lines, in our calculations we use an interpolation scheme. This work ($\odot$), Langhoff *et al.*[149](1989) ($\square$), Langhoff *et al.*[148](1986) ($\times$), Werner *et al.*[147] ($\star$), experimental curve by Nelson *et al.*[142] (- -), and experimental curve by Murphy[131] (−.). The curve of Murphy is determined up to a constant, and was shifted up by about 0.85 ea_0 for graphical reasons.

interpolation procedure, we find that the maximum of our dipole moment lies at exactly the same interatomic distance as Nelson's: 2.300 a_0, whereas Langhoff's electric dipole moment function has a maximum at 2.2850 a_0 and Werner's at 2.2670 a_0. A scaled and shifted form of Werner's dipole moment function was used in the last extensive fully *ab initio* calculation on the OH-Meinel system in 1986[148].

One of the most stringent tests on the quality of the *ab initio* calculated dipole moment function is comparing vibrationally averaged dipole moments with the very accurate measurements of Peterson *et al.*[159]. The experimentally determined dipole moments are accurate up to 10^{-5} ea_0 for $v = 0$ and $v = 1$ and 10^{-4} ea_0 for $v = 2$. In all references cited here, the comparison of experimental with *ab initio* computed dipole moments was done after shifting and/or scaling the *ab initio* dipole moment functions. Here, we compute the vibrationally averaged dipole moments without any scaling of the dipole
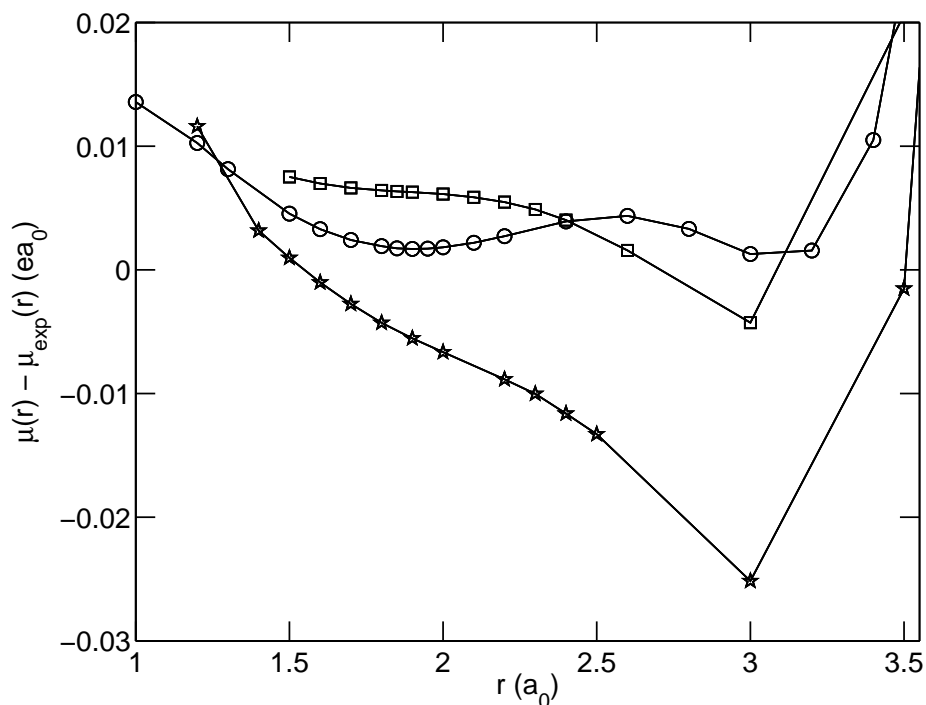
Figure 3.2: Difference between *ab initio* electric dipole moment functions and the "experimental" dipole moment function of Nelson *et al.*[142]. This work ($\odot$), Langhoff *et al.*[149] (1989) ($\square$), and Werner *et al.*[147]($\star$).

moment function. For comparison, we also computed this property using some previously published dipole moment functions. The results are shown in Table 3.4. It can be seen that our dipole moment function yields values in very close agreement with the experimental results, with differences between experiment and *ab initio* results of about 0.0020 ea_0. for the $v = 0$ and $v = 1$ levels, and 0.034 ea_0 for $v = 3$.

3.3.3   Lifetimes

In the first and second column of Table 3.5 we show the lifetime of the $OH(v = 1, J = 3/2, F_1, p)$ states, which are the only states of which the lifetimes have been determined directly by experiment[122]. The lifetimes have been computed using different dipole moment functions and methods and are compared with the two best-known current values: the direct measurement of Meerakker *et al.*[122], and the value which can be extracted from the HITRAN 2004 database Eqs. (3.17) and (3.19). The HITRAN values we use here are ultimately based on the calculation by Goldman[140].

Table 3.4: Computed and experimental vibrationally averaged dipole moments of OH in ea_0.

v	Exp.[a]	Present	L89[b]	WRR[c]
0	0.65120(4)	0.6527	0.6570	0.6457
1	0.65411(6)	0.6561	0.6598	0.6481
2	0.6550(4)	0.6582	0.6611	0.6490
3		0.6585	0.6605	0.6479
4		0.6567	0.6578	0.6446
5		0.6522	0.6524	0.6386
6		0.6444	0.6437	0.6291
7		0.6324	0.6311	0.6157
8		0.6153	0.6136	0.5974
9		0.5919	0.5901	0.5731

[a] Peterson *et al.*[159]. Converted from Debye using 1 Db = 0.39343031369 ea_0.
[b] Langhoff *et al.*[149]
[c] Werner *et al.*[147]

The dipole moment functions by Langhoff *et al.* (L86), Murphy (M71), and Werner *et al.* (WRR) give lifetimes which differ from the experimental values by about 15 to 30 ms. The dipole moment of Langhoff (L89), Nelson (N90), and from this work all give values which are within the experimental errors. Since our dipole transition moment is slightly higher than the experimental values in Table 3.4, we also compute the lifetimes after scaling our dipole (μ_{sc}). The scaling factor (0.9966) is the avarage ratio between the experimental and our *ab initio* expected values for the dipole moment. The effect is an increase in lifetime of about 0.41 ms.

To investigate the effect of scaling the potential, we also compute the lifetimes using wave functions from our potential without scaling it (labeled nosc). We also compute the lifetimes using our wave functions and the transition frequencies taken from HITRAN (labeled ω_H) to distinguish overlap effects from energy level effects. The difference in lifetime for these two methods is about 0.05 ms. This indicates that rovibrational wave functions are well represented in our calculation. Thus, we expect the error in lifetimes caused by the error in calculated transition frequencies to be on the order of 0.05%.

In Fig. 3.2, we show the r-dependent spin-orbit coupling $H_{\mathrm{so}}(r)$. The spin-orbit coupling matrix element rises steeply between 2.8 and about 5.5 a_0. At 7.0 a_0 the spin-orbit coupling is within one cm^{-1} of its asymptotic value, -100.74 cm^{-1} at 16 a_0. The vibrationally averaged spin-orbit splitting
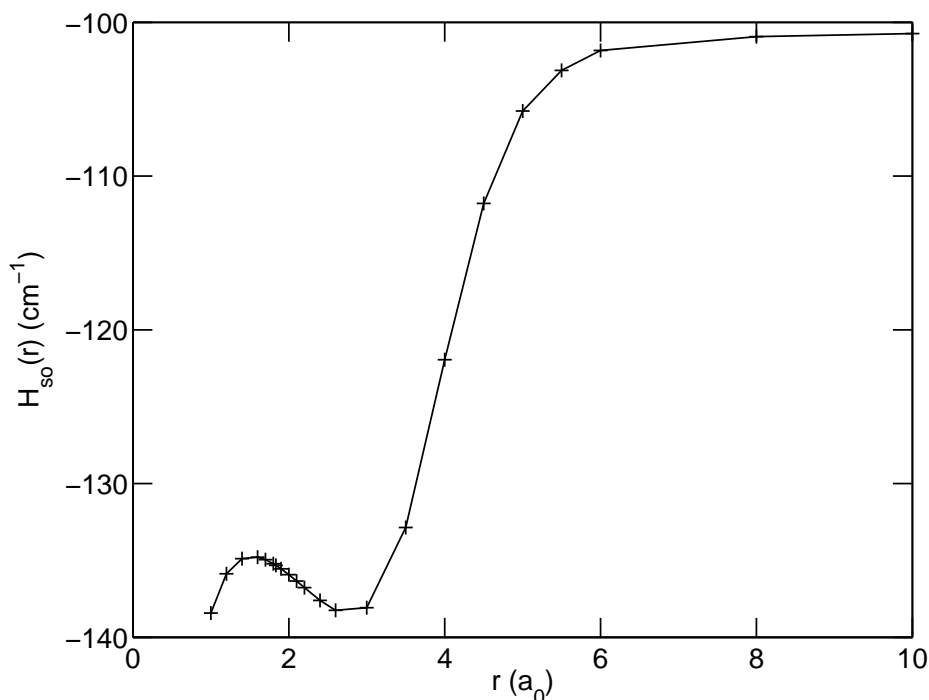
Figure 3.3: *r*-dependent spin-orbit coupling computed in this work.

is 135.48 cm^{-1} for $v = 0$, which is close to the experimental spectroscopic A constant shown in Table 3.1. From $v = 1$ to $v = 8$ the vibrationally averaged spin-orbit splitting increases from 135.79 to 137.09 cm^{-1}. For $v = 9 - 10$ the splitting decreases again to 136.63 cm^{-1} for $v = 10$. This behavior is consistent with the spin-orbit A constants, shown in Table 3.1.

In the third and fourth column of Table 3.5 we compare the lifetimes computed using the r-independent spin-orbit Hamiltonian [$H^{\text{so}}_{|\Omega|,|\Omega'|}$, Eq. (3.7)] with the values obtained using $H_{\text{so}}(r)$. Since the transition frequencies are slightly different when $H^{\text{so}}_{|\Omega|,|\Omega'|}$ is used in stead of $H_{\text{so}}(r)$, we also compare with the ω_H calculation. We conclude that replacing the r-dependent spin-orbit coupling with the parametrized Hamiltonian decreases the computed lifetime of OH[$X^2\Pi(v = 1, J = 3/2)$] by about 0.001 ms. Calculations for higher rovibrational levels show that this effect decreases exponentially as the rotational or vibrational level increases. The effect that the approximate $H^{\text{so}}_{|\Omega|,|\Omega'|}$ Hamiltonian yields better results for higher excited states can be explained by the notion that higher excited rovibrational states probe larger internuclear distances, where the spin-orbit coupling becomes constant. Also, higher excited vibrational levels have more kinetic energy, so the approximation of a vibrationally averaged spin-orbit coupling becomes better at higher

Table 3.5: Lifetime of the OH($v = 1, J = 3/2, F_1, p$) states, computed using various dipole moment functions and methods.

Exp.	$e(-)$	$f(+)$	error bars	
Direct[a]	59.0		± 2 ms	
HITRAN[b]	56.6113	56.6244	$\pm 10 - 20\%$	
	$H_{so}(r)$		$H^{so}_{\|\Omega\|,\|\Omega'\|}$	
Calc.	$e(-)$	$f(+)$	$e(-)$	$f(+)$
μ_{sc}[c]	57.2246	57.2253	57.2235	57.2242
present[d]	56.8364	56.8371	56.8354	56.8360
nosc[e]	56.8835	56.8842	56.8824	56.8831
ω_H[f]	56.8359	56.8366	56.8272	56.8278
N90[g]	55.7004	55.7011	55.6989	55.6996
L89[h]	57.7759	57.7766	57.7742	57.7749
WRR[i]	71.6343	71.6352	71.6319	71.6328
L86[j]	81.3144	81.3154	81.3104	81.3114
M71[k]	85.6512	85.6522	85.6480	85.6490

[a] Experiment by Meerakker *et al.*[122]
[b] Computed from the HITRAN 2004[160] database.
[c] Scaled potential and scaled dipole moment.
[d] This work, using the scaled potential.
[e] This work, using the *ab initio* potential.
[f] This work, using HITRAN transition frequencies.
[g] Fitted dipole moment function by Nelson.[142]
[h] *Ab initio* dipole moment function by Langhoff *et al.*[149](1989).
[i] *Ab initio* dipole moment function by Werner *et al.*[147]
[j] *Ab initio* dipole moment function by Langhoff *et al.*[148] (1986).
[k] Fitted dipole moment function by Murphy[131] (1971).

excited rovibrational states. Using our transition dipole moment and scaled potential energy curve, we computed a total of 42356 photoabsorption cross sections and Einstein A coefficients, which can be retrieved *via* the EPAPS[156] system in ASCII format. The file contains the cross sections $\bar{\sigma}_{ul}$ as defined in Eq. (3.14), the Einstein A coefficients defined in Eq. (3.19), the full set of quantum numbers $\{v, J, F_n, p\}$ for upper and lower state, the transition energy and the energy of the lower state with respect to the dissociation energy D_e. We include vibrational levels $v = 0 - 10$ and rotational levels up to and including $J = 121/2$. The potential energy curve, electric dipole
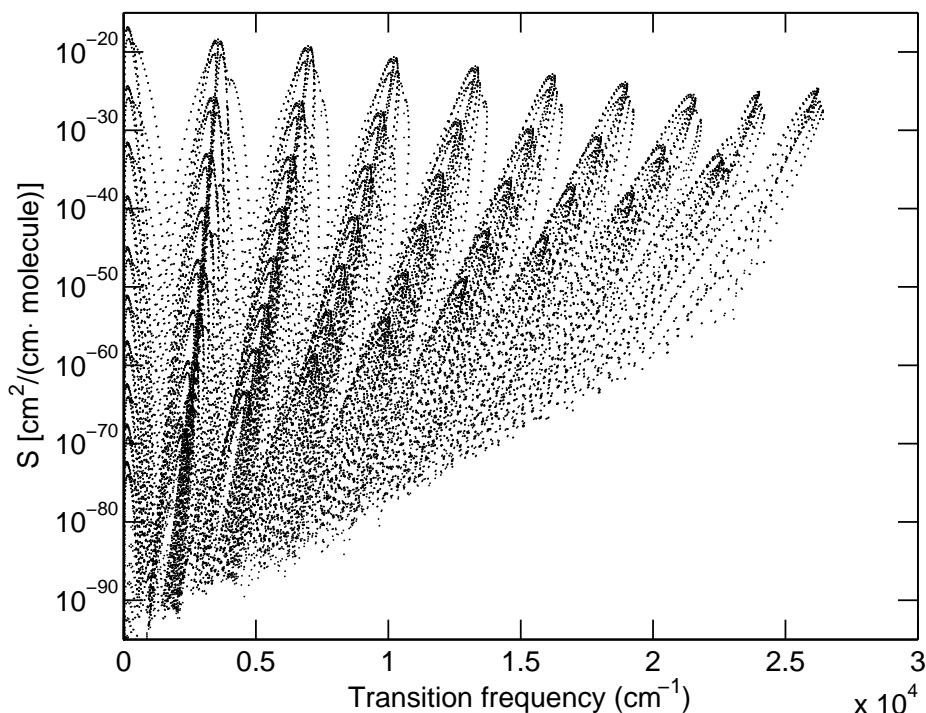
Figure 3.4: Rovibrational line strengths for all transitions up to and including $v = 10, J = 121/2$, computed at a temperature of 296 K.

moment function and spin-orbit coupling function are also included in the EPAPS data.

As an illustration, we plot the line intensity S_{ul} for all rovibrational bands of OH in the $X^2\Pi$ state in Fig. 3.4, at a temperature of 296 K. The line intensities are computed using Eq. (3.13), where the partition function $Q(296) = 80.362$ is taken from the HITRAN database.

3.4   Conclusion

We computed a new, accurate *ab initio* potential energy curve, electric dipole moment function, and spin-orbit coupling function for $OH(X^2\Pi)$. Both the calculated permanent vibrationally averaged dipole moments and spin-orbit couplings are computed with unprecedented precision. The effect of the OH bond length dependence of the spin-orbit coupling is investigated and we conclude that the maximum variation in lifetimes is on the order of 0.001 ms (about 0.0001%). The effect decreases exponentially as the rotational or vibrational quantum number increases. The effect of lambda-type doubling

on the mixing of states with different Ω quantum number is incorporated for the first time. We report a new set of accurate photoabsorption cross sections and Einstein A coefficients, available *via* the EPAPS[156] system.

3.4.1 Acknowledgements

Appendix: Einstein A and B coefficients, Degeneracy, Line intensity and HITRAN

In the course of this work, we found an error in a preliminary version of the HITRAN 2004 database, which could be traced back to an overcounting of spin- and electronic degeneracies in the equation for the line intensity. Here, we summarize a derivation of Eqs. (3.13) and (3.17) and discuss the effects of (near) degeneracy on the line intensity.

Einstein A and B coefficients

The chance to find a particle in a fully specified single quantum state $|\alpha\rangle$ at a given temperature is given by the Boltzmann distribution:

$$P_\alpha = \frac{e^{-\beta E_\alpha}}{Q(T)}, \tag{3.20}$$

where $\beta = 1/k_\mathrm{b}T$, $Q(T) = \sum_\alpha e^{-\beta E_\alpha}$ the internal partition sum of the molecule and E_α is the total energy of the state. The chance to find a particle with some energy E_n is given by:

$$P_{E_n} = \frac{\sum_{i=1}^{g_n} e^{-\beta E_n}}{Q(T)} = \frac{g_n e^{-\beta E_n}}{Q(T)}, \tag{3.21}$$

where the sum runs over g_n linear independent state functions with eigenvalue E_n. In spectroscopy, often only states which differ in energy are resolved. Consider the transition

$$|2\rangle \xleftarrow{h\nu} |1\rangle, \tag{3.22}$$

between states of energy E_1 and E_2. The rate of state $|2\rangle$ production is given by Einstein's differential equation[a]:

$$\frac{\partial N_2}{\partial t} = -\frac{\partial N_1}{\partial t} = N_1 \overline{W} B_{12} - N_2 \overline{W} B_{21} - N_2 A_{21}, \tag{3.23}$$

where $\overline{W}$ is the energy density of radiation at the transition frequency ω in $\text{J}/(\text{m}^3\text{s}^{-1})$. Solving this equation for thermal equilibrium, using Boltzmann statistics and Planck's radiation law, the following relations are obtained[95]:

$$g_1/g_2 B_{12} = B_{21} \quad \text{m}^3/(\text{Js}^2) \tag{3.24}$$

$$A_{21} = \hbar\omega^3/(\pi^2 c^3)B_{21} \quad \text{s}^{-1}, \tag{3.25}$$

where we are using rationalized MKS (Giorgi) units.

Line Intensity

Consider the change of intensity $d\bar{I}$ of a beam traversing a dilute gaseous sample of volume V as a function of traversed length dz:

$$d\bar{I} = -(N_1 B_{12} - N_2 B_{21})\frac{\hbar\omega}{Vc}\bar{I}\Phi(\omega)dz, \tag{3.26}$$

where $\Phi(\omega)$ is the frequency normalized line profile of the transition, $\bar{I} = c\overline{W}$ and N_1 and N_2 are the number of particles respectively in states $|1\rangle$ and $|2\rangle$ in the volume traversed by the beam. Comparing this equation with Beer's law:

$$d\bar{I}(z) = -\kappa(\omega)\bar{I}(z)dz, \tag{3.27}$$

we get:

$$\kappa(\omega) = (\bar{N}_1 B_{12} - \bar{N}_2 B_{21})\frac{\hbar\omega}{c}\Phi(\omega) \quad (\text{m}^{-1}), \tag{3.28}$$

where the number density $\bar{N}_i = N_i/V$ depends on temperature according to the Boltzmann distribution:

$$\bar{N}_i = \bar{N}g_i e^{-\beta E_i}/Q(T) \quad i = 1, 2. \tag{3.29}$$

Notice that the unit of Φ is s. The HITRAN line intensity is defined as the integrated absorption coefficient divided by the total number density $\bar{N}$:

$$S_{2\leftarrow 1}^{\text{obs}}(T) = \bar{N}^{-1}\int \kappa(\omega)d\omega \quad (\text{s}^{-1}\text{m}^2/\text{molecule}). \tag{3.30}$$

---

[a]The Einstein absorption B_{12} coefficient for a transition $2 \leftarrow 1$ is labeled in the order 1,2. This is opposite of the spectroscopic convention, which is to use the upper state as the first label.

For a narrow transition $\Phi(\omega)$ is replaced by the Dirac delta function, centered at the transition frequency ω_0, and we get:

$$S_{2\leftarrow 1}^{\text{obs}}(T) = \bar{N}^{-1}(\bar{N}_1 B_{12} - \bar{N}_2 B_{21})\frac{\hbar\omega_0}{c}. \tag{3.31}$$

The quantum mechanical expression for the Einstein B_{12} coefficient reads:

$$B_{12} = \frac{\pi}{\epsilon_0 \hbar^2} \frac{1}{g_2} \sum_{n_1=1}^{g_1} \sum_{n_2=1}^{g_2} |\langle 2|\boldsymbol{\varepsilon} \cdot \boldsymbol{\mu}|1\rangle|^2, \tag{3.32}$$

where we sum over initial, and avarage over final states. Combining Eq. (3.24) with Eqs. (3.29), (3.31) and (3.32), using the expression for the fine-structure constant $\alpha = e^2/(4\pi\epsilon_0\hbar c)$, and introducing the isotope abundance I_a, Eqs. (3.13) and (3.14) can be derived. With the help of Eq. (3.25), Eq. (3.17) can be written down as well.

(Near) Degeneracy

So far we discussed transitions between states which are defined up to degeneracy. That is, the transition strength $S_{2\leftarrow 1}^{\text{obs}}$ is labeled by all quantum numbers of state $|1\rangle$ and $|2\rangle$ that determine the total energy and g_2 represents the number of degenerate (unresolved) states of energy E_2. Often experimental conditions are such that transitions between a number of nearly degenerate states are observed simultaneously. If we make the approximation that nearly degenerate states have the same energy E_f and E_i respectively, the nearly degenerate states will be equally occupied and we can still use Eq. (3.17) to compute the observed line intensity:

$$S_{\mathbf{ul}}^{\text{obs}}(T) = \frac{e^{-\beta E_{\mathbf{u}}} - e^{-\beta E_{\mathbf{l}}}}{Q(T)} \frac{\pi^2 c^2 I_a g_{\mathbf{u}}}{\omega_0^2} A_{\mathbf{ul}}, \tag{3.33}$$

with the difference that $g_{\mathbf{u}}$ now corresponds to the total number of unresolved degenerate and nearly degenerate final states. Another way of stating this is that $g_{\mathbf{u}}$ is determined by all quantum numbers of the upper state that do not label the transition $S_{\mathbf{ul}}^{\text{obs}}$.

The type and number of different quantum numbers one can assign to a state function depend directly on the symmetry properties of the system. However in general we can distinguish electronic, vibrational, spin, parity, and rotation-like quantum numbers, in various coupling schemes. We will consider as example two cases of experimental resolution.

Hyperfine structure fully resolved   If the hyperfine structure is fully resolved, the degeneracy factor is given by:

$$g_{\mathbf{u}} = g_2 = (2F' + 1), \tag{3.34}$$

where F' is the total angular momentum in the upper state, including nuclear spin. Here, the transition is specified up to all quantum numbers except the total conserved angular momentum projection quantum number $M_{F'}$.

Hyperfine structure not resolved   Suppose hyperfine structure is not resolved in a spectrum, and the transitions are specified up to the J quantum number, which includes all rotation except nuclear spin. $g_{\mathbf{u}}$ is than given by:

$$g_{\mathbf{u}} = \prod_n (2I'_n + 1)(2J' + 1), \tag{3.35}$$

where n labels the nuclei, and I' represents upper state nuclear spin. The reason behind this factor is that the transition is now labeled with all quantum numbers except projection of J' and for each J' substate there are $\prod_n (2I'_n + 1)$ nuclear spin states.

CHAPTER 4

Raman association of H$_2$

We investigate the formation of molecular hydrogen by an inelastic Raman scattering process which can take place in astrophysical environments. In the Raman process that we study, a photon is scattered by a pair of colliding hydrogen atoms leaving a hydrogen molecule that is stabilized by the transfer of kinetic and binding energy to the photon. We use a formulation for calculating the photon scattering cross section in which an infinite sum of matrix elements over rovibrational levels of dipole accessible electronic states is replaced by a single matrix element of a Green's function. We evaluate this matrix element by using a discrete variable representation.

4.1 Introduction

The formation of H$_2$ from a pair of neutral hydrogen atoms in the presence of a radiation field can be brought about by a Raman association process. Its efficiency depends on the spectrum and the intensity of the radiation field and it varies as the square of the hydrogen atom density. The process is likely to contribute to H$_2$ formation in dense atomic gas subjected to intense radiation fields at wavelengths longer than the threshold wavelengths for absorption in the Lyman and Werner band systems. In photon-dominated regions the

ultraviolet photons may dissociate the molecules but with increasing depth into the gas the corresponding optical depths become large and the H_2 molecules are self-shielding. The optical depth for Raman association is small. Raman association may also contribute to the formation of H_2 in the high atmospheres of hot Jupiters and generally in regions of atomic hydrogen subjected to strong Lyman alpha radiation.

When the incident photon has a large wavelength the scattering cross section and the corresponding rate of association for the production of molecular hydrogen can be calculated from the polarizability of the hydrogen molecule[161,162]. However at wavelengths close to and smaller than Lyman α, resonant excitation of the bound rovibrational levels of dipole accessible excited electronic states of the molecule enhances the cross sections and the association rates[162].

4.2   Theory

The Raman association process involves the inelastic scattering, from energy $\hbar\omega$ to $\hbar\omega_{\text{sc}}$, of electromagnetic radiation by a pair of hydrogen atoms colliding on the $X^1\Sigma_g^+$ ground state surface of molecular hydrogen:

$$\text{H}(^2S) + \text{H}(^2S) + \hbar\omega \rightarrow \text{H}_2(^1\Sigma_g^+) + \hbar\omega_{\text{sc}}. \tag{4.1}$$
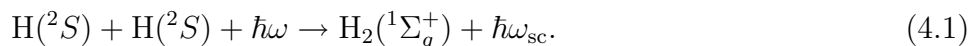
The cross section in cm^2J^{-1} associated with this process is given by:

$$\sigma_{fi}(\omega) = \frac{8\pi\alpha^2\omega\omega_{\text{sc}}^3}{9c^2e^4} S_{fi}(\omega), \tag{4.2}$$

where α is the fine-structure constant, c is the speed of light and e is the electronic charge. In Eq. (4.2) the Raman scattering matrix $S_{fi}(\omega)$ is given by the Kramers-Heisenberg equation[95]:

$$S_{fi}(\omega) = \sum_{st} \left| \sum_m \frac{\langle f|\hat{\mu}_s|m\rangle\langle m|\hat{\mu}_t|i\rangle}{\omega_{mi} - \omega + i\Gamma_m/2} + \frac{\langle f|\hat{\mu}_s|m\rangle\langle m|\hat{\mu}_t|i\rangle}{\omega_{fi} + \omega} \right|^2, \tag{4.3}$$

where the coherent sum is over all the intermediate states $|m\rangle$, $\omega_{xy} = \omega_x - \omega_y$, Γ_m is the inverse lifetime of the intermediate state $|m\rangle$ and $\hat{\mu}_s$ and $\hat{\mu}_t$ are components of the dipole moment operator. In the calculation of Federman and Frommhold[162] the sum over intermediate states in Eq. (4.3) was evaluated explicitly but only partially. The sum may be evaluated implicitly in terms of dipole response functions[163–168] which may be expressed in terms of Green's functions[166,167]. We discuss below a method to evaluate the matrix

elements of the Green's functions. The first term in Eq. (4.3) can give rise to resonances where the second term can be neglected. In the off-resonant case, where $\omega_{mi} \gg \omega$, the scattering matrix is given by the polarizability theory of Placzek and Teller[161] as:

$$S_{fi}^{\mathrm{PT}}(\omega) = \frac{1}{9}|\langle f|\alpha_\parallel + 2\alpha_\perp|i\rangle|^2 \delta_{J''J'} + B_{J'}^{J''}|\langle f|\alpha_\parallel - \alpha_\perp|i\rangle|^2, \qquad (4.4)$$

where $\alpha_\parallel$ and $\alpha_\perp$ are the parallel and perpendicular components, respectively, of the polarizability of a hydrogen molecule in its ground state, and $B_{J'}^{J''}$ depends on the initial and final rotational quantum numbers (J'' and J', respectively) of the system:

$$B_{J'}^{J''} = \begin{cases} \frac{3}{2}\frac{J''(J''-1)}{(2J''-1)(2J''+1)} & J' = J'' - 2 \\ \frac{J''(J''+1)}{(2J''-1)(2J''+3)} & J' = J'' \\ \frac{3}{2}\frac{(J''+1)(J''+2)}{(2J''+1)(2J''+3)} & J' = J'' + 2. \end{cases} \qquad (4.5)$$

We apply the usual Born-Oppenheimer approximation and we represent the wave functions in Eq. (4.3) in the Hund's case (a) basis $\{|\psi_{(a)p}^{JM_J}\rangle\}$:

$$|\psi_{(a)p}^{JM_J}\rangle = \frac{1 + (-1)^p \hat{i}}{\sqrt{2 + 2\delta_{\Lambda 0}\delta_{\Sigma 0}}}\sqrt{[J]/4\pi}D_{M_J\Omega}^{(J)*}(\alpha, \beta, 0)|v; n\Lambda S\Sigma\rangle, \qquad (4.6)$$

where Λ, S, Σ, and Ω are the usual Hund's case (a) quantum numbers, p denotes parity, $\hat{i}$ is the parity operator, n is the electronic primary quantum number, $\sqrt{[J]/4\pi}D_{M_J\Omega}^{(J)*}(\alpha, \beta, 0)$ is a two-angle normalized Wigner D-function, and v the vibrational quantum number, which is replaced by the kinetic energy E for continuum states. We use the parity convention defined by Van Vroonhoven and Groenenboom[78]. We denote $2J + 1$ by $[J]$ throughout.

Neglecting the second term in Eq. (4.3) and integrating over the angular variables we find that the rotationally resolved scattering matrix for relative collision energies E'' in the parity-unadapted basis can be written as:

$$S_{J'v'\Omega';J''E''\Omega''}(\omega) = \frac{1}{[J'']}\sum_{M_{J''}M_{J'}}\left|\sum_{J\Omega}\mathcal{S}_{J'M_{J'}\Omega'}^{J''M_{J''}\Omega''}(J\Omega)\mathcal{M}_{v'J'\Omega'}^{E''J''\Omega''}(J\Omega)\right|^2. \quad (4.7)$$

The angular factor $\mathcal{S}$ is given by:

$$\mathcal{S}_{J'M_{J'}\Omega'}^{J''M_{J''}\Omega''}(J\Omega) =$$

$$(-1)^{J+\Omega+J'-M_{J'}+J-M_J}[J]\sqrt{[J'][J'']}\sum_{M_J}\begin{pmatrix} J' & 1 & J \\ -M_{J'} & 0 & M_J \end{pmatrix}$$

$$\times \begin{pmatrix} J & 1 & J'' \\ -M_J & 0 & M_{J''} \end{pmatrix}\begin{pmatrix} J' & 1 & J \\ 0 & -\Omega & \Omega \end{pmatrix}\begin{pmatrix} J & 1 & J'' \\ -\Omega & \Omega & 0 \end{pmatrix}, \quad (4.8)$$
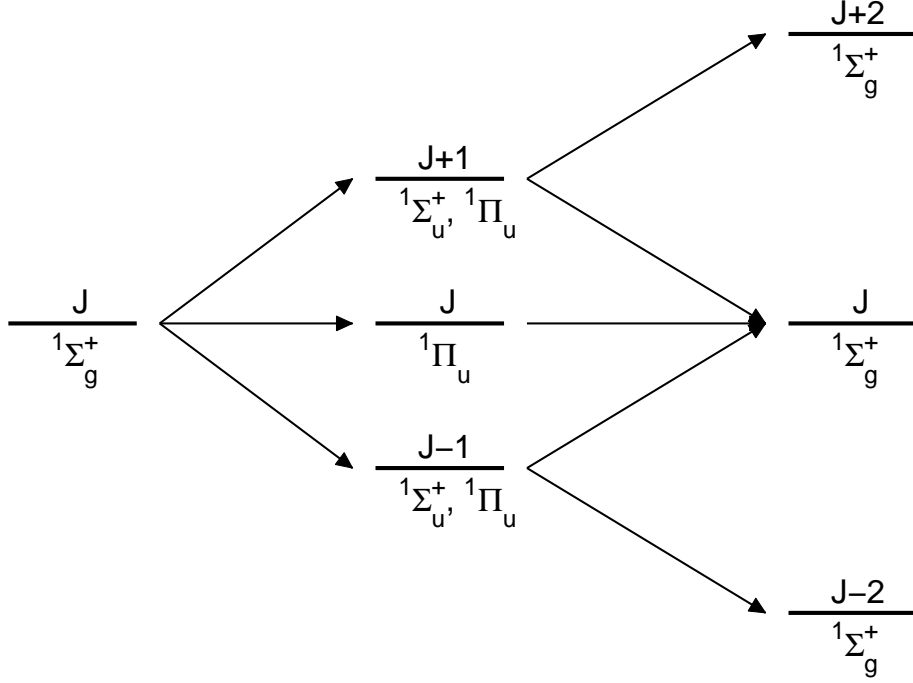
Figure 4.1: The possible pathways for rotational changes in Raman association. The path $J \rightarrow J \rightarrow J$ is not possible for $^1\Sigma_u^+$ intermediate states.

where we used that in the $X^1\Sigma_g^+$ state we have $\Omega' = \Omega'' = 0$. The angular factor predicts electronic and rotational selection rules for the Raman association process, schematically represented in Fig. 4.1; the selection rules also reduce the number of candidates in the coherent sum over intermediate states in Eq. (4.3). In Raman association, the system starts in the continuum of levels with rotational quantum number J'' of the $X^1\Sigma_g^+$ ground electronic state and finishes as a bound level, with rotational quantum number J'' or $J'' \pm 2$, of the $X^1\Sigma_g^+$ electronic state; transitions to final levels with rotational quantum number $J'' \pm 1$ are forbidden. Fig. 4.1 signifies that the only allowed intermediate states in Eq. (4.3) are levels of electronic states of $^1\Sigma_u^+$ and $^1\Pi_u$ symmetries, and that the rotational quantum numbers are restricted to $J'' \pm 1$ for the $^1\Sigma_u^+$ intermediate levels and J'' and $J'' \pm 1$ for the $^1\Pi_u$ intermediate levels. The dynamical part $\mathcal{M}$ is given by:

$$\mathcal{M}_{v'J'\Omega'}^{E''J''\Omega''}(J\Omega) = \hbar \sum_n \langle v'; J'n'\Omega' | \hat{d}_{-\Omega} \hat{G}_{nJ\Omega} \hat{d}_{\Omega} | E''; J''n''\Omega'' \rangle_r, \qquad (4.9)$$

where integration is over the nuclear coordinate r, the $\hat{d}_x$ are the relevant components of the body-fixed dipole operator given by $\hat{\mu}_s = \sum_x \hat{d}_x D_{sx}^{(1)*}(\alpha, \beta, 0)$,

and $\hat{G}$ is the Green operator associated with the Schrödinger equation for nuclear motion in the adiabatic Born-Oppenheimer hydrogen atom r-dependent potential, $V_{n\Omega}(r)$, of the relevant electronic intermediate state:

$$\hat{G}_{nJ\Omega}(\omega) = \left[\left(\frac{-\hbar^2}{2\mu r}\frac{d^2}{dr^2}r + V_{n\Omega}(r) + \frac{f^{\Omega}(J)}{2\mu r^2}\right) - E'' - \hbar\omega + i\Gamma/2\right]^{-1}, \quad (4.10)$$

where r is the nuclear separation, μ is the reduced mass for the motion and

$$f^{\Omega}(J) = \begin{cases} J(J+1) & \Omega = 0 \\ J(J+1) - 1 & |\Omega| = 1. \end{cases} \quad (4.11)$$

Here we have neglected terms in the Hamiltonian that couple different electronic states.

In practice, the infinite sum over electronic states in Eq. (4.3) is truncated so as not to include any contributions from distant electronic states. However the contribution of distant electronic states to the scattering matrix can be considered to be independent of ω[168]. We write

$$S_{fi}(\omega) = S_{fi}^{\text{KH}}(\omega) + S_{fi}^{\text{corr}}, \quad (4.12)$$

where S_{fi}^{KH} is the scattering matrix element obtained when the sum in Eq. (4.3) is truncated and S_{fi}^{corr} is a constant correction term that accounts for the distant states' contribution which can be estimated by examining scattering matrix elements in the off-resonance region, where the Placzek-Teller approximation holds. The correction is

$$S_{fi}^{\text{corr}} = S_{fi}^{\text{PT}}(\omega) - S_{fi}^{\text{KH}}(\omega) \qquad \omega \ll \omega_{mi}, \quad (4.13)$$

where S_{fi}^{PT} is expressed in terms of the polarizabilities, $\alpha_{\perp}$ and $\alpha_{\parallel}$, by Eq. (4.4) and the calculation of the polarizabilities includes all intermediate electronic states. We evaluate the correction from Eq. (4.13) with $S_{fi}^{\text{PT}}(\omega)$ and $S_{fi}^{\text{KH}}(\omega)$ computed at energy $\hbar\omega = 2.401 \times 10^4$ cm^{-1}.

In the calculation by Federman and Frommold[162], the term $\alpha_{\parallel} + 2\alpha_{\perp}$ of Eq. (4.1) was replaced by $\alpha_{\parallel} + 2\alpha_{\perp} - 6\alpha_0$, where α_0 is the polarizability of the hydrogen atom. Similarly, the r-dependent dipole transition moments $d(r)$ were replaced by $d(r) - d(\infty)$. However, since nuclear eigenstates on the $X^1\Sigma_g^+$ electronic surface are orthogonal, the extra term $\langle f|\alpha_0|i\rangle$, arising from the subtraction, vanishes and is therefore unnecessary for rovibrational Raman scattering.
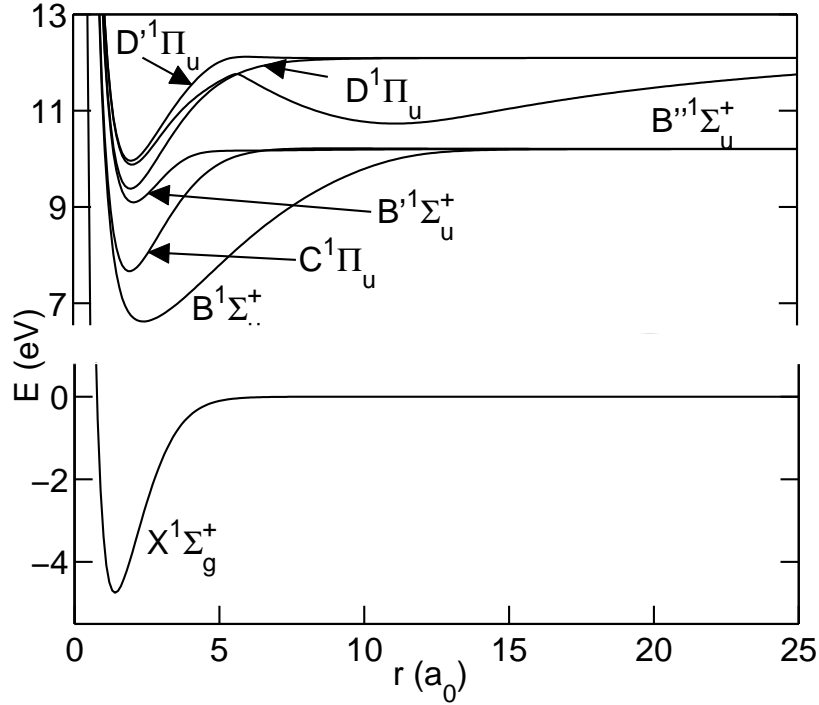
Figure 4.2: The lowest singlet potential energy curves[169–172] of H_2; the $B''^1\Sigma_u^+$ and the $D'^1\Pi_u$ states each have a double well structure.

4.3 Numerical Methods

The central part of our calculation is the evaluation of Eq. (4.9). We choose a grid-based representation. The nuclear Hamiltonian matrix and final nuclear bound states are represented using the sinc-function discrete variable representation[100] (sinc-DVR). The numerical initial state nuclear wave functions are obtained by using the renormalized Numerov method to propagate them on the $X^1\Sigma_g^+$ potential energy curve and then matching them to scattering boundary conditions. We restrict the sum over intermediate electronic states to a sum over 6 optically allowed states; 3 are of $^1\Sigma_u^+$ symmetry and 3 are of $^1\Pi_u$ symmetry (See Fig. 4.2). The *ab initio* potential energy curves and electronic dipole transition moments are taken from calculations by Wolniewicz and Staszewska[169–172]. We use the vibrationally resolved lifetimes from the work by Fantz and Wünderlich[173] to estimate the inverse lifetime Γ_m of each intermediate state. In the case where $E'' + \hbar\omega > V_{n\Omega}(r \to \infty)$, that is where the sum of the initial state energy and the energy of the incoming photon exceeds the dissociation limit of an intermediate electronic state, we use the Green function absorbing boundary condition (ABC) method[73–75] to prevent

the matrix in Eq. (4.10) from becoming singular. The ABC-method consists of replacing the constant $\frac{1}{2}\Gamma_m$ by an r-dependent function $\gamma(r)$, thus effectively augmenting the potential $V_{n\Omega}(r)$ with a negative imaginary potential which absorbs the wave function in the physically non-relevant outer region. Here we choose the Woods-Saxon potential:

$$\gamma(r) = \frac{2\lambda}{1 + \exp\left(r_{\max} - r\right)/\eta}, \tag{4.14}$$

where λ and $r_{\max}$ are to be chosen such that sufficient absorption takes place and η is to be chosen small enough to ensure that no significant reflection occurs.

The main computational task is to solve the linear systems of equations associated with the representation of the term $\hat{G}_{nJ\Omega}\hat{d}_\Omega|E''; J''n''\Omega\rangle$ in Eq. (4.9). Since the potential energy curves of intermediate electronic states have different r-dependences, we save computational time by adapting the grid and minimizing the number of basis functions for each intermediate state. That is, we keep the grid spacing constant and minimize the range of the grid. The linear systems can than be solved on each grid separately, and the solutions projected so that the inner product with the final state $\langle v; J'n'\Omega'|\hat{d}_{-\Omega}$ can be taken. Table 4.1 shows the different grids used in this work. At the resonances the matrix in Eq. (4.10) is singular and we represent the term $\hat{G}_{nJ\Omega}\hat{d}_\Omega|E''; J''n''\Omega\rangle$ in Eq. (4.9) by $\chi_v^{nJ\Omega}(r)\langle v; nJ\Omega|d_\Omega|E''; n''J''\Omega''\rangle/(i\Gamma_m/2)$, where $\chi_v^{nJ\Omega}(r)$ is the rovibrational nuclear wave function associated with the resonance. Inspection of the resonances shows that the two methods of calculation are consistent with each other. The Raman association cross section is

Table 4.1: Number of grid points used for each intermediate state potential. The grid points are given by $0.2, 0.3, \ldots, 0.2 + 0.1N$.

	$X^1\Sigma_g^+$	$B^1\Sigma_u^+$	$B'^1\Sigma_u^+$	$B''^1\Sigma_u^+$	$C^1\Pi_u$	$D^1\Pi_u$	$D'^1\Pi_u$
N	118	198	198	398	118	198	398

computed for a grid of photon frequencies. Because the cross section is very sharply peaked around resonances we do not use a grid that is linear in photon energy $\hbar\omega$ but choose instead a grid that is logarithmically spaced around each resonance. The grid is cut off at 13.6 eV. Extensive experimentation showed that choosing 50 logarithmically spaced points around every resonance while leaving out redundant points gives a satisfactory description of the spectral features. In total there are about 350 rovibrational resonances in each spectrum depending on the initial rotational quantum number, yielding about $12,300$ points on average to be computed per spectrum.
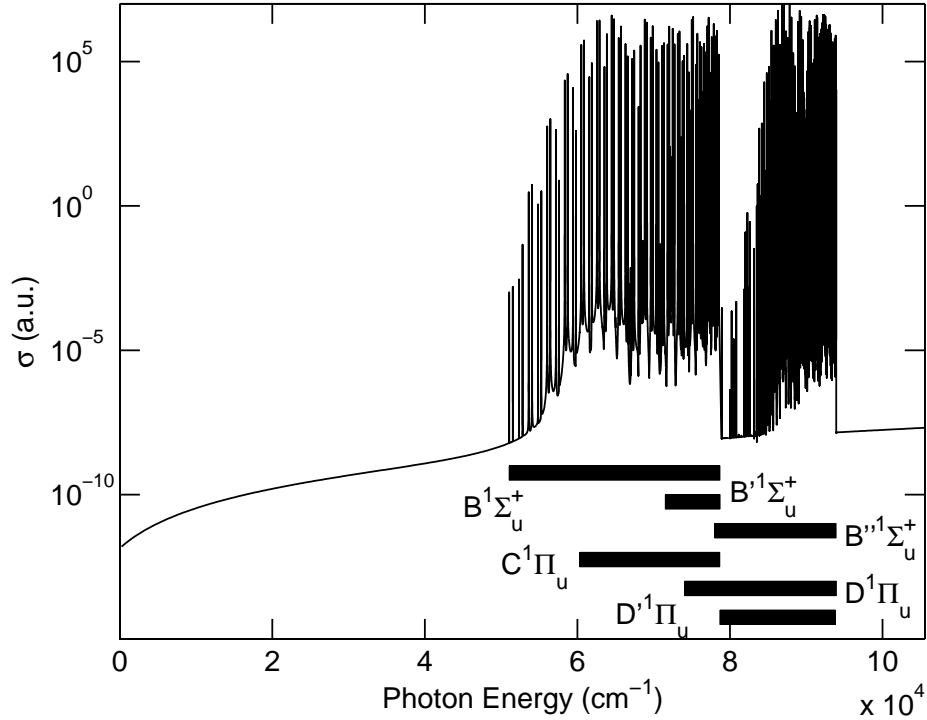
Figure 4.3: Total Raman association cross section in atomic units of area/energy, as a function of photon energy. The collision energy is 0.448 eV, and initial rotational quantum number $J'' = 6$. The bars indicate the occurrence of rovibrational resonances associated with the indicated excited electronic state.

For comparison we compute cross sections according to the theory of Placzek and Teller. The matrix elements in Eq. (4.1) are evaluated using the r-dependent polarizability of molecular hydrogen in the ground state computed by Wolniewicz[172]. The initial (scattering) and final (bound) states are evaluated on the grid as described above.

4.4   Results

Fig. 4.3 shows the total Raman association cross section as a function of photon energy for two hydrogen atoms, colliding at an energy of $E = 0.448$ eV. The cross section shown is computed with the truncated Kramers-Heisenberg equation, and the corrections from Eqs. (4.12) and (4.13) are applied. The (initial) rotational quantum number is $J'' = 6$; this is appropriate to the most abundant rotational state in the early Universe at a matter and radiation temperature of about 4,000 K. The bars show where rovibrational

resonances of the various intermediate states occur. The cross section increases smoothly with photon energy, until the resonance region is reached. At higher photon energies, in the resonance region, the cross section increases significantly. The off-resonance background cross section increases with about four orders of magnitude compared with the low photon energy region. At a resonance, the cross section may be five to ten orders of magnitude larger than the background cross section. At about $78,770$ cm^{-1} the cross section in this spectrum decreases rapidly. The reason is that at these photon energies the second dissociation continuum of the $B^1\Sigma_u^+$, $B'^1\Sigma_u^+$, and $C^1\Pi_u$ states is reached, and there are not many bound state resonances in this energy region. At higher energies the number of resonances, and thus the cross section, increases significantly again. The sharp cutoff at $93,950$ cm^{-1} occurs where the sum of the photon energy and the collision energy exceeds the dissociation limit of the $B'''^1\Sigma_u^+$, $D^1\Pi_u$, and $D'^1\Pi_u$ states.

In Fig. 4.4 we show the resonances associated with intermediate states, specifically the $v = 0, J = 5$, and $v = 0, J = 7$ levels of the $B^1\Sigma_u^+$ electronic state; absence of a resonance at the $v = 0, J = 6$ level is consistent with the selection rules depicted in Fig. 4.1. The dashed lines indicate the cross sections, $\sigma_{J' \leftarrow J''} \equiv \sum_{v'} \sigma_{v'J';E''J''}$, associated with transitions from an initial state whose rotational quantum number is $J'' = 6$ in the $X^1\Sigma_g^+$ continuum to the various final rovibrational levels of the $X^1\Sigma_g^+$ state. In the $\sigma_{6 \leftarrow 6}$ cross section we find the two resonances at the $v = 0, J = 5$ and $v = 0, J = 7$ levels of the $B^1\Sigma_u^+$ state, showing the contributions *via* the two paths for intermediate $^1\Sigma_u^+$ electronic state depicted in Fig. 4.1. We find one resonance in each of the $\sigma_{4 \leftarrow 6}$ and $\sigma_{8 \leftarrow 6}$ cross sections associated, respectively, with the $v = 0, J = 5$ and $v = 0, J = 7$ levels of the $B^1\Sigma_u^+$ state.

We also calculated the vibrationally resolved cross sections $\sum_{J'} \sigma_{v'J' \leftarrow E''J''}$. In Fig. 4.5 the relative vibrational distributions at different photon scattering energies, $\hbar\omega$, are compared. The black bars indicate results obtained with the Kramers-Heisenberg formula, Eq. (4.3), and the white bars indicate results obtained from from the Placzek-Teller approximation. The photon angular frequencies are presented relative to the position of the angular frequency, denoted ω_0, of the $B^1\Sigma_u^+(v = 0, J = 5)$ resonance. In the off-resonance region, where $\omega - \omega_0$ is equivalent to an energy shift from resonance of about $-40,265$ cm^{-1} (and $\hbar\omega = 2.401 \times 10^4$ cm^{-1}), the vibrational distributions predicted by the Kramers-Heisenberg formula and the Placzek-Teller approximation are very similar although the total cross sections differ significantly; the higher lying vibrational levels (with vibrational quantum number $v = 10 - 13$) are populated preferentially. When the photon energy increases to about 2.2 cm^{-1} below the resonance, the distribution predicted by the Kramers-Heisenberg equation starts to differ from the Placzek-Teller
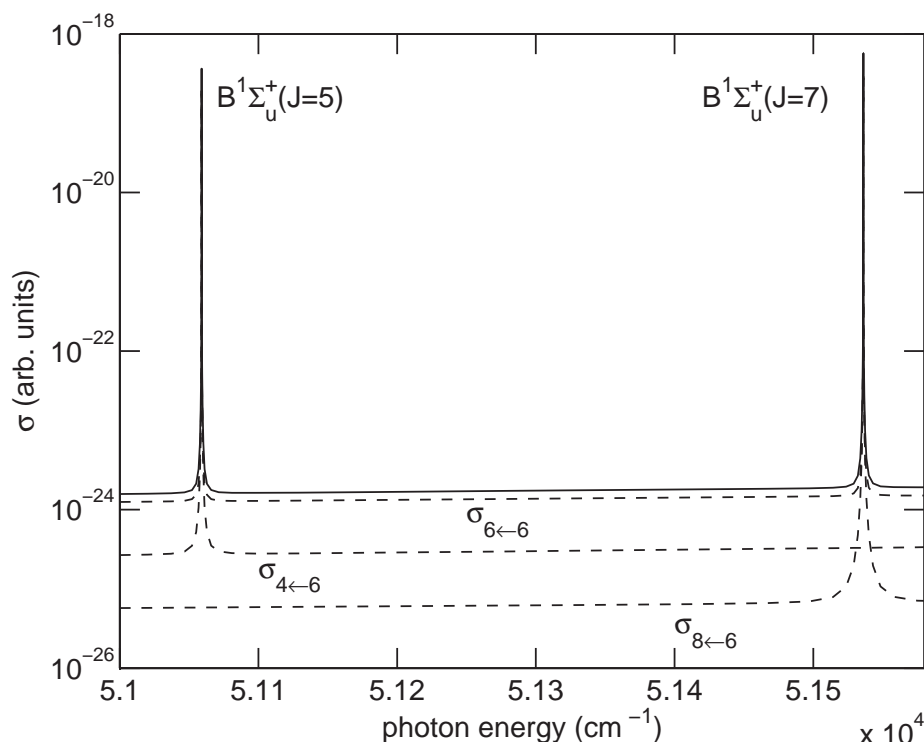
Figure 4.4: Raman association cross sections at the resonances associated with the $B^1\Sigma_u^+(v=0)$, $J=5$ and $J=7$ states. The dashed lines indicate the cross sections for the $J'=4 \leftarrow J''=6$, $J'=6 \leftarrow J''=6$ and $J'=8 \leftarrow J''=6$ transitions, respectively.

distribution; within 2.2 cm^{-1} of the resonance a significant number of lower-lying vibrational states, mainly with $v=1-7$, become populated while the vibrational distribution predicted by the Placzek-Teller approximation remains largely unaltered. At the resonance, the Kramers-Heisenberg equation predicts no significant population of the levels with $v=10-14$. The distribution is completely different from that predicted by the Placzek-Teller approximation which fails to take proper account of the resonance contributions. The distribution predicted by the Kramers-Heisenberg equation is similar to that obtained from consideration of spontaneous or stimulated emission from the $B^1\Sigma_u^+(v=0, J=1)$ state to the ground state levels.

4.5   Conclusion and outlook

We pointed out that molecular hydrogen may be formed by Raman scattering by a pair of hydrogen atoms colliding in the $X^1\Sigma_g^+$ state and we presented a
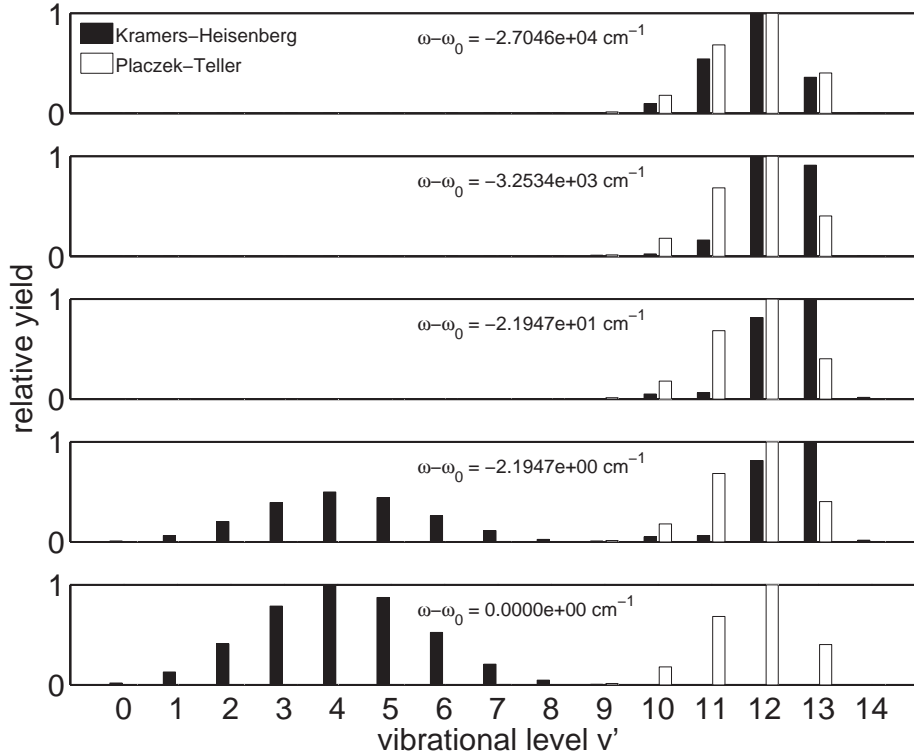
Figure 4.5: Relative yield of $X^1\Sigma_g^+$ vibrational states upon Raman association of H-atoms, colliding with a relative collision energy of 0.448 eV and $J'' = 6$ as a function of photon angular frequency ω. Here, ω_0 is the frequency associated with the $B^1\Sigma_u^+(v = 0, J = 5)$ resonance.

method for the accurate evaluation of the Raman cross sections in a radiation field. We carried out a direct evaluation of the Kramers-Heisenberg equation *via* a Green operator formalism. We used a grid-based representation. We presented the first full calculation of photon-energy dependent Raman association cross sections including all rovibrational resonances associated with the intermediate states, based on the accurate electronic potential energy surfaces and properties computed by Wolniewicz *et. al*[169–172]. We compared the exact results with those of the Placzek-Teller approximation and we showed that final state vibrational distributions obtained with the Placzek-Teller approximation and with the Kramers-Heisenberg expression are comparable except in the region of the resonances where they differ significantly. Future work will include thermal averaging over the collision energies of hydrogen atom pairs and calculations of Raman association rate constants with application to the formation of molecular hydrogen in astrophysical environments.

Recombination of H_2 by Raman association in the early universe

We investigate the contribution that Raman association makes to H_2-production in the early universe at redshifts $10 \leq z \leq 10^4$. The Raman process involves inelastic scattering of electromagnetic radiation off two colliding hydrogen atoms, taking away kinetic and binding energy and leaving bound H_2. We calculate the inelastic cross sections and rate coefficients for this process and determine the Raman association rate in the cosmic background radiation field present during the early stages of the universe. A comparison with other H_2-forming reactions in the early universe is made.

5.1   Introduction

According to the current standard cosmology, the universe began in an intensly hot, dense state which cooled and expanded ever since. After a brief inflationary and nucleosynthesis period, nucleons and electrons became stable and the universe cooled adiabatically, with thermal equilibrium between radiation and matter. After about 2×10^5 years (redshift $z \approx 5 \times 10^5$) the temperature had dropped to about 5000 K, and the first atoms began to

form, mostly H, He and a trace of Li and their ions. At this point, matter and radiation became thermally decoupled and matter cooled faster than radiation. As there were no heavy elements, and star formation had not yet occured, there was no dust and all chemistry that took place was necessarily gas-phase (photo) chemistry.

The formation of molecules was an important event in the evolution of the early universe. The chemistry and formation of molecules in the early universe have been reviewed recently by Lepp *et al.*[51], Dalgarno[52], and Galli and Palla[53]. The presence of molecular hydrogen is believed to have played an important role in the early cosmological structure formation[174].

The mechanisms that have been explored for the formation of molecular hydrogen are the reaction sequences initiated by the radiative association of H^+ and He and H^+ and H and the direct formation of H_2 by associative detachment in collisions of H^- and H and the radiative association of ground and excited hydrogen atoms. In this paper we focus on the formation of hydrogen molecules from hydrogen atoms. Symmetry arguments show that direct association of a pair of ground state hydrogen atoms to form a hydrogen molecule that is stabilised by the emission of a photon is not possible; the symmetry is broken for a collision of a hydrogen atom and a deuterium atom and direct association can proceed slowly[53,175,176]. We investigate the possibility that a contribution to the formation of molecular hydrogen in astrophysical environments arises from Raman scattering of photons where a transition occurs from a point in the vibrational continuum of the ground electronic state, $X^1\Sigma_g^+$, of molecular hydrogen (that describes a pair of colliding hydrogen atoms) to a bound vibrational level of the $X^1\Sigma_g^+$ state; the excess energy (kinetic and binding) is removed by the scattered photons. In this work we calculate the contribution of Raman association to the formation of H_2 and compare it to those of other processes that have been taken into account in models of the evolution of the universe[51,53].

5.2   Theory and method

Raman association is an inelastic scattering process, where electromagnetic radiation of energy $\hbar\omega$ scatters off two colliding $H(^2S)$ atoms, and causes a transition from the continuum to a bound state of $H_2(^1\Sigma_g^+)$. Kinetic and binding energy $\hbar(\omega_{sc} - \omega)$ is transfered to the radiation field in the process:

$$H(^2S) + H(^2S) + \hbar\omega \rightarrow H_2(^1\Sigma_u^+) + \hbar\omega_{sc}. \tag{5.1}$$
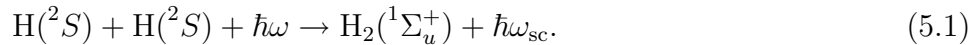
The H_2 production rate for this processes is given by an Arrhenius-type equation:

$$\frac{dn(H_2)}{dt} = k(T_m, T_r)n(H)^2,\tag{5.2}$$

where the rate constant k depends on the matter temperature T_m and radiation temperature T_r, and the $n(X)$ are number densities in cm^{-3}. The rate constant is related to the Raman scattering cross section σ *via* the following relation:

$$k(T_m, T_g) = \frac{gcV}{2}$$
$$\times \sum_f \iint dEd\omega\, P_{T_m}(E)\rho_{T_r}(\omega)\sigma_{fi}(E,\omega),\tag{5.3}$$

where $g = 1/4$ takes into account that $3/4$ of all collisions take place on the $H_2(^3\Sigma_g^+)$ surface, and do not add to the Raman association rate. In Eq. (5.3), c is the speed of light, V is unit volume, and the factor $1/2$ is introduced because the rate of association [Eq. (5.2)] is expressed in H-atom density, rather than H-H pair density. The matter temperature dependence is determined by the Boltzmann distribution

$$P_{T_m} = \frac{\lambda_0^3}{V}(2J + 1)e^{-E/k_b T_m},\tag{5.4}$$

with J the rotational quantum number and $\lambda_0 = \sqrt{2\pi\hbar^2/\mu k_b T_m}$ the thermal De Broglie wavelength, while μ is the reduced mass of the hydrogen molecule. The dependence on radiation temperature is determined by the Planck photon number density distribution:

$$\rho_{T_r}(\omega) = \frac{\omega^2}{2\pi c^3}\frac{1}{e^{\hbar\omega} - 1}.\tag{5.5}$$

The cross section depends on the collision energy E, and the photon energy ω, and is given by:

$$\sigma_{fi}(E,\omega) = \frac{8\pi\alpha^2\omega\omega_{sc}^3}{9c^2e^4}S_{fi}(E,\omega),\tag{5.6}$$

where α is the fine-structure constant, e the elementary charge, and S is the Raman scattering matrix, given by the Kramers-Heisenberg equation [See Eq. (4.3)]. The computational method we use to calculate the cross sections is described in detail in the previous chapter.

Table 5.1: Processes contributing to the formation of H_2 in the early universe. All reaction rates from Stancil *et al.* [175], except (2d) taken from Sauval and Tatum [177], and (4) from this work. All reaction rates are given in cm^3s^{-1} except (2d) in s^{-1}.

	Reaction			rate constant (cm^3s^{-1} or s^{-1})
(1)	$H^- + H$	$\rightarrow$	$H_2 + e^-$	$1.5 \times 10^{-9}(T_m/300)^{-0.1}$
(2a)	$H^+ + H$	$\rightarrow$	$H_2^+ + \hbar\omega$	$6 \times 10^{-19}(T_m/300)^{1.8}e^{20/T_r}$
(2b)	$H_2^+ + H$	$\rightarrow$	$H_2 + H^+$	6.4×10^{-10}
(2c)	$H_2^+ + e^-$	$\rightarrow$	$H + H$	$1.2 \times 10^{-8}(T_m/300)^{-0.4}$
(2d)	$H_2^+ + \nu$	$\rightarrow$	$H^+ + H$	$1.63 \times 10^7 e^{-32400/T_r}$
(3)	$H^* + H$	$\rightarrow$	$H_2 + \hbar\omega$	$2.09 \times 10^{-14}(T_m/300)^{0.24}e^{-T_r/37800}$
(4)	$H + H + \hbar\omega$	$\rightarrow$	$H_2 + \hbar\omega_{sc}$	This work

The large number of rovibrational resonances [see Fig. 4.3] in the cross section as a function of photon- and H-H scattering energy complicates numerical evaluation of the double integral in Eq. (5.3). In order to ensure convergence of the integral $\int d\omega \rho_{T_r}(\omega)\sigma(E,\omega)$ in Eq. (5.3), we increased the number of points in the cross section as a function of ω. We did this by taking the logarithm (base 10) of the cross sections and use cubic spline interpolation from resonance to resonance, after which the interpolated values are exponentiated. This way, a stable interpolation without oscillations was obtained. We also checked if the number of computed cross sections is large enough to be fitted by cubic splines by leaving out 50% of the *ab initio* points and fitting again. We find that the results have converged to within 1 %.

After integration over the photon energy ω, a smooth function of the collision energy E is obtained. We constructed a satisfactory representation by evaluating it at 20 logarithmically spaced collision energies E, in the range $10^{-6} - 10^{-2}$ a.u.. We use cubic spline interpolation again to converge the integral over E in Eq. (5.3).

5.3   Early universe

We investigate the importance of Raman association of H_2 in the early universe, after electron-nucleon recombenation (2×10^5 years, $z \approx 5 \times 10^3$), but before the first star formation (10^8 years, $z \approx 10$) by comparing the rate of association with a number of other important H_2-forming processes.

We considered (see Table 5.1) associatiative detachment of H^- and H, radiative association of H^+ and H followed by reaction with H, competing with dissociative recombination, photodissociation of H_2^+, and reaction of

H_2^+ with H^-, radiative association of excited and ground state hydrogen, and Raman association. The total H_2 density as a function of time in this model is given by:

$$n(H_2) = \sum_{s=1}^{4} \int_{t_0}^{t} d\tau \, R_s(\tau), \qquad (5.7)$$

where the R_s are the production rates $dn(H_2)/dt$ for the different processes in Table 5.1, and $t_0 = 1.367 \times 10^{12}$ s. Here, we also neglect that reaction products arising from the destruction of H_2 enter the expressions for R_1 to R_4. For processes (1), (3) and (4) in Table 5.1 the production rates in cm^{-3}/s are given by:

$$R_s = k_s(T_m, T_r)n(x)n(y), \qquad (5.8)$$

where $n(x)$ and $n(y)$ are the number densities of the relevant reactants, and the reaction rate constants k are given in Table 5.1. To compute the production rate of processes running *via* the H_2^+ intermediate, we incorporate the strongest H_2^+-destroying processes [labeled (2c) and (2d)]. Using a steady-state model for H_2^+, we get:

$$R_2 = \frac{k_{2a}n(H^+)n(H) \times k_{2b}n(H)}{k_{2b}n(H) + k_{2c}n(e^-) + k_{2d}}. \qquad (5.9)$$

We use densities of H, H^-, H^*, H^+, and gas and radiation temperature as a function of redshift, as computed by Stancil *et al.*[175]. The electron density $n(e^-)$ is assumed to be equal to the proton density. During the early stages of the universe, after recombination but before formation of the first stars the radiation temperature decreases from about 10^4 K at $z \approx 10^4$ to 10 K at $z \approx 10$ and the gas temperature decreases from about 10^3 to 10^{-3} K. The total gas density decreases from approximately 10^3 to 10^{-3} cm^{-3}.

5.4   Results

Figure 5.1 shows the Raman association rate constant as a function of matter temperature (T_m) and radiation temperature (T_r). The rate constant decreases with increasing matter temperature because although the collision rate increases with temperature, the shorter H-H interaction time per collision reduces the cross section for Raman association significantly. The rate constant drops about four orders of magnitude as the gas temperature increases from 10 to 10^4 K. The dependence on radiation temperature is much
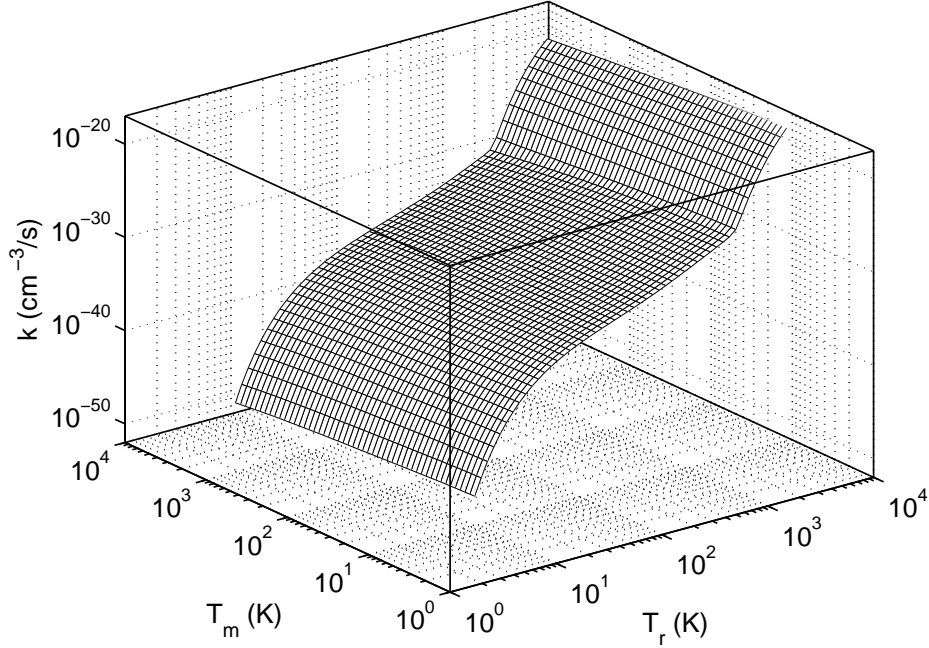
Figure 5.1: Raman association rate constant as function of matter temperature T_m and radiation temperature T_r.

stronger, the rate constant increases steeply as the radiation temperature becomes higher. From 10 to ~ 2700 K, the rate constant increases by as much as twenty orders of magnitude. At $T_r \approx 2700$ K the increase with temperature becomes stronger: from $2700 - 10^4$ K, the rate constant increases by about ten orders of magnitude. The reason is that at high radiation temperatures high-energy photons become available so that the cross sections, and thus the rate constants are significantly enhanced by the resonances.

In Fig. 5.2 the H$_2$ production rates for the processes in Table 5.1 are shown as a function of redshift. The Raman association rate (dashed line) has a maximum at $z \approx 1385$, when both the radiation and matter temperature are about 3800 K. At this time, the Raman association rate is comparable with the other H$_2$-producing processes. The maximum is due to the competition between the increasing availability of atomic hydrogen, caused by the recombination of protons with electrons, and the decreasing radiation temperature. At $z \approx 10^3$, the Raman association rate starts decreasing more slowly with time. Although both radiation and matter temperature drop below 2750 K here, it is the decrease in T_r that causes the change in behaviour. At later times the H$_2$-production is completely taken over by the H$^+$-catalysed process and the associative detachment of H$^-$ and H.
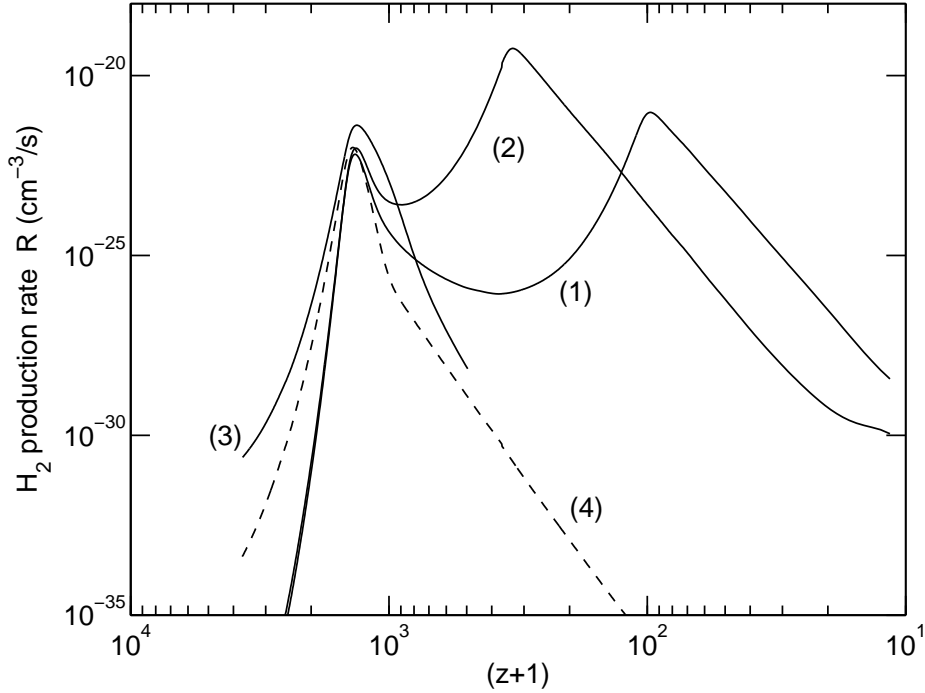
Figure 5.2: H_2 production rates as a function of redshift z in the early universe. For the meaning of (1)-(4), see Table 5.1. The dashed line indicates the Raman association rate in cm^{-3}/s. The redshift z corresponds to a time scale running from 4.33×10^4 to 2.35×10^8 yrs.

In Fig. 5.3 we show the fractional H_2 abundance $n_s(H_2)/n_H$, where n_H is the total H-density, produced by the different processes. It can be seen that at $400 \lesssim z \lesssim 2600$, a significant amount of the existing H_2 was produced by Raman association, although the total H_2 abundance was still small. At $z \approx 1600$, as much as 25% of H_2 present at that time was produced by Raman association, the remaining 75% mainly came from radiative association of excited H with H. The result for the total fractional abundance $n(H_2) = \sum_{s=1}^{4} n_s(H_2)$ as a function of z agrees well with calculations performed by Stancil et al.[175] and Galli and Palla[53]. Although we necessarily overestimate the total fractional abundance $n(H_2)/n_H$ since we neglect H_2 destroying processes, we do reproduce the freeze-out time for H_2 at $z \approx 100$. The effect of H_2-destruction is especially important at high redshift mainly because of the high efficiency of H photoionisation[175]. If we assume that the destruction rate of H_2 is independent of how the molecules were formed, it is not important for this comparison.

In Table 5.2, we show the fractional abundances for different processes, at
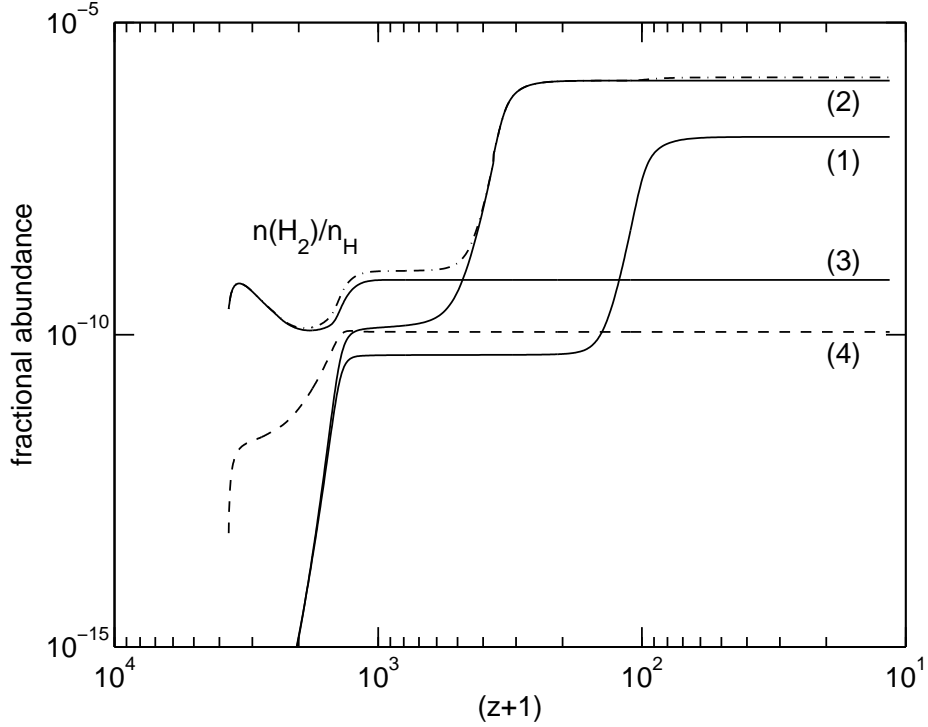
Figure 5.3: Relative contributions to H$_2$ density in the early universe. For the meaning of (1)-(4) see Table 5.1. The dashed line depicts the contribution of Raman association.

redshift $z = 10.5$. We find a total fractional abundance of about 1.3×10^{-6}, where Stancil *et al.*[175] and Galli and Palla[53] find about 1.1×10^{-6}. Of all

Table 5.2: Integrated contributions to H$_2$ production at $z = 10.5$ for the processes in this model.

Process	$n_s(\mathrm{H_2})/n_{\mathrm{H}}$
(1)	1.4711×10^{-7}
(2)	1.1718×10^{-6}
(3)	7.5352×10^{-10}
(4)	1.1071×10^{-10}
Total	1.3197×10^{-6}

molecular hydrogen ever produced up to $z = 10.5$ about 0.01% was produced by Raman association, which is not much less than the contribution made by radiative association of excited with ground state hydrogen ($\sim 0.08\%$).

5.5   Conclusion

We investigate the rate of association of molecular hydrogen *via* a Raman scattering process. We present the first calculation of the corresponding inelastic scattering cross section over a wide range of photon- and collision energies, in which all relevant rovibrational resonances are included. From these cross sections we obtain the Raman association rate constant as a function of matter-, and gas temperature and we use these rate constants to evaluate the rate of Raman association under conditions present in the early universe. We show that the contribution to H_2 production around $z \approx 1600$ is significant. The total contribution to the H_2 production up to $z = 10$ is comparable to the contribution made by radiative association of excited and ground state H-atoms: on the order of 0.01%. We show that it is crucial to take into account the effect of resonances at high radiation temperatures in various astrophysical circumstances.

Acknowledgements.

Validation of long-range interaction models for photofragment polarization of an N_2O-like molecule

The validity of an analytical long-range interaction model which has been used to interpret recent molecular photodissociation experiments is investigated. The experiments involve a determination of photofragment electronic polarization parameters using molecular beam techniques. In the model, adiabatic behaviour is assumed in the short range, and a frame transformation from the molecular to the atomic states is used to model the product state distribution in the long range, where the dynamics are considered to be purely diabatic. Validity of the model is investigated by developing model potential energy surfaces, electronic dipole moment surfaces and nonadiabatic couplings for an N_2O-like molecule for which the long-range interaction model should hold. Detailed photodissociation calculations involving five adiabatic Born-Oppenheimer states are performed for the $N_2O + \hbar\omega \rightarrow N_2(^1\Sigma_g^+) + O(^1D_{\lambda\omega_\lambda})$ reaction using these model properties. The oxygen $|\omega_\lambda|$ distribution is obtained as a function of N_2 rotational state and photodissociation energy. The calculations are compared with the model and with experimental results by Teule *et al.*[58]. Qualitative agreement between experimental and calculated N_2 rotational distributions is obtained. The calculations do not reproduce the experimental photofragment polarization, mainly due to differences between the modeled and experimental excitation step and because of the form of the nonadiabatic interactions in the model. A study of convergence behaviour as a function of the photodissociation grid reveals that assumptions behind the long-range interaction model are only partly valid.

6.1   Introduction

Photodissociation processes are the motor behind chemical processes in planetary atmospheres[178–182], and are important in many astrophysical circumstances such as the interstellar medium[183,184], protoplanetary disks[185,186] and interstellar molecular clouds[187–190]. It was also an important process for chemistry of the early universe[191].

The study of photodissociation processes is interesting in itself since it they offer a sensitive experimental probe of interactions between atoms and molecules. In the past quarter century, the developments in molecular beam techniques, laser spectroscopy, cold molecule research[34,38], and imaging methods[37] have made it possible to start studying photodissociation processes in tremendous detail. Recently, production of cold fragments by photodissociation of Stark decelerated SO_2 molecules was proposed by Jung *et al.*[192,193].

By controlling the initial state of molecules before dissociation, and determining the recoil velocity and internal state distribution of the photofragments, in principle the full photodissociation cross section can be obtained. Some of the most detailed information one can extract from these experiments is the distribution of projection quantum numbers (polarization) associated with the rotation of the photofragments and the rotation of the electrons about the photofragments with respect to the molecular- or laboratory frame.

Recently, photofragment electronic angular momentum polarizations have been measured for a number of triatomic systems such as N_2O (Teule *et al.*[58], 2000), NO_2 (Coroiu *et al.*[194], 2006), SO_2 (Brouard *et al.*[59], 2004) and ozone (Brouard *et al.*[195], 2006). In these cases, the velocity map imaging[35,36] technique was employed, and a theoretical model based on the sudden limit approximation and long-range interaction was used to interpret the data.

In the subsequent sections, the experiment on N_2O by Teule *et al.* will be used as an example. In that experiment, a hexapole state selector was used to prepare a beam of neutral quantum state-selected N_2O molecules in the electronic ground $X^1\Sigma^+$ state. The selected molecules were in the rovibrational ground state, with $N_2 - O$ bending quantum number $\nu = 1$. The molecules were subsequently dissociated using a laser at 203-205 nm yielding the reaction:

$$N_2O(X^1\Sigma^+; v_{N_2}, \nu, v) + \hbar\omega \rightarrow N_2(^1\Sigma_g^+; j, v'_{N_2}) + O(^1D_2), \qquad (6.1)$$
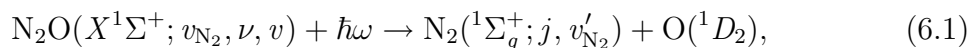
where v_{N_2} is the $N - N$ stretching, ν the $N_2 - O$ bending, v the $N_2 - O$

stretching, and j the N_2 fragment's rotational quantum number. The $O(^1D_2)$ fragments are produced in the $\lambda = 2$ state with electronic photofragment projection quantum numbers ω_λ distributed over $\omega_\lambda = -2, -1, \ldots 2$, where ω_λ is defined here with respect to the Jacobi vector which connects the center of mass of the N_2 fragment with the oxygen fragment. The $N_2(j, v'_{N_2})$ and $O(^1D_2)$ fragments were quantum state-selectively detected using velocity mapped imaging, which allowed for a determination of the $O(^1D_2)$ electronic polarization as a function of N_2 rovibrational state (j, v'_{N_2}). The resulting N_2 molecules that are produced are vibrationally cold ($v'_{N_2} = 1$ for less than 2% of the molecules[196]) but rotationally highly excited. The rotational state distribution has a single maximum at $j = 74$. The dependence of the $O(^1D_2)$ polarization on j was interpreted in terms of the long-range interaction model mentioned above.

In the following subsection the long range interaction model and its underlying assumptions is explained. In the subsequent sections these assumptiones are checked by developing a model interaction Hamiltonian for N_2O for which a long range interaction model can also be applied. Next, fully quantum mechanical photodissociation calculations for this system are presented and compared with the model. Although the model system of our choice here is N_2O, the conclusions about the validity of the model can be expected to hold more generally.

6.1.1 Long-range interaction model

Consider the photodissociation process from Eq. (6.1). In principle there are five adiabatic electronic potential energy surfaces involved in the excitation step: three of $^1A'$ symmetry, and two of $^1A''$ symmetry. In the long range, these surfaces correspond to degenerate linear combinations of the ω_λ-states in the $O(^1D_2)$ limit [see also Sec. 6.2.2]. In the experiment by Teule *et al.*[58] the excitation energy is such that excitation mainly takes place to the $2^1A'$ surface (97%) with a small contribution of the $1^1A''$ surface (3%). Both excitations are allowed only upon bending of the molecule and are forbidden in the linear geometry.

The excitation step from the electronic ground state in the can be represented as:

$$|1^1A'\rangle + \hbar\omega \rightarrow \alpha_1|2^1A'\rangle + \alpha_2|1^1A''\rangle, \tag{6.2}$$

where $|1A'\rangle$ represents the adiabatic electronic ground state, and the α_i are expansion coefficients of the adiabatic electronic wave function after excitation.

In the model description nuclear dynamics is not included explicitly. It is further assumed that in the short range, dissociation proceeds adiabatically on the $2^1A'$ and $1^1A''$ surfaces. However, in the long range the nonadiabatic couplings between the five asymptotically degenerate electronic states become significant, so all five states can be occupied by the system. In the long range, the interaction between the $O(^1D_2)$ and N_2 fragments is given by the quadrupole-quadrupole interaction Hamiltonian [given in Eq. (6.24) below]. It is also assumed that in the long range, the electronic states evolve adiabatically and are determined completely by the quadrupole-quadrupole interaction. The electronic eigenstates in the long range are thus obtained by diagonalizing the 5×5 quadrupole-quadrupole interaction Hamiltonian $\hat{V}_Q(\theta)$ with matrix elements $\langle \lambda \omega'_\lambda | \otimes \langle \Sigma_g^+ | \hat{V}_Q(\theta) | \Sigma^+ \rangle \otimes | \lambda \omega_\lambda \rangle$, where $|\Sigma^+\rangle$ is the electronic wave function of N_2, and the $|\lambda \omega_\lambda\rangle$ are the five degenerate $O^1(D_2)$ states with $\omega_\lambda = -2, -1, \ldots 2$. This interaction is anisotropic and thus the eigenstates depend parametrically on the Jacobi angle (θ) between the $N - N$ axis and the Jacobi dissociation vector, pointing from the center of mass of N_2 to the oxygen atom. The diagonalisation yields five eigenstates: three of A', and two of A'' symmetry. The ω_λ populations in these states are given by the absolute squares of the components $c_{\omega_\lambda}^\gamma(\theta)$ (γ labeling the symmetry) of the eigenvectors. Neglecting coherent contributions (motivated by the fact that excitation occurs mostly onto the $2^1A'$ surface), the chance $P_{\omega_\lambda}(\theta)$ to find the $O(^1D_2)$ atom in some angular momentum state ω_λ is given by:

$$P_{\omega_\lambda}(\theta) = \alpha_1^2 |c_{\omega_\lambda}^{2^1A'}(\theta)|^2 + \alpha_2^2 |c_{\omega_\lambda}^{1^1A''}(\theta)|^2. \tag{6.3}$$

If it is assumed that a higher rotational quantum number j of the N_2 fragment corresponds to a larger dissociation angle θ, it is possible to analyze experimental data where ω_λ populations are measured against the molecular rotational state. In the work by Teule *et al.* this was done, and qualitative agreement between the model and the experiment was obtained.

The validity of the model depends on the ratio between the timescale on which the molecule rotates, and the time it takes for the dissociating fragments to reach the long-range limit. The model is plausible in the limit where the recoil velocity is high enough so that the atom and molecule have reached the long-range interaction limit before the molecule completes half a turn. In the case of the N_2O photodissociation experiments by Teule *et al.*, most of the N_2 fragments are produced in rotational levels with $j = 66 - 82$, with the maximum at $j = 74$. This corresponds to rotational frequencies of $\sim 4 \times 10^{13}$ s^{-1}. Less than 50% of the dissociation energy (which is ~ 0.05 au) is released as recoil kinetic energy, which corresponds to about 5×10^{13} Å/s. Thus, assuming direct dissociation, the N_2 molecule

has rotated about four times before the oxygen atom reaches the long-range interaction region (around 5 Å). If the whole rotational distribution of N_2 is taken into account, on average more than 90% of the dissociation energy is transferred to rotational motion of the N_2 fragment. These arguments lead to the central question of this chapter:

> At which fragment separation does the photofragment electronic angular momentum polarization become fixed in lab space, and how does this depend on dissociation conditions, such as the total dissociation energy and rotational state?

In the following sections, this question is studied explicitly for an N_2O-like molecule by developing model interaction- and electric dipole (transition) surfaces, and performing detailed quantum mechanical photodissociation calculations.

In section 6.2 the Hamiltonian of the N_2O molecule is given and a symmetry-adapted basis set expansion for the potential energy operator is derived for the short-range (Sect. 6.2.1 and 6.2.2) as well as the asymptotic long-range (Sect. 6.2.3). In all calculations the N-N distance is frozen at its equilibrium distance of 2.13199 a_0. Next, in Sections 6.2.4 and 6.3 the model potential energy surfaces and model dipole (transition) moment surfaces are developed. Both the potential energy surfaces and the dipole moment surfaces are constructed to yield a computationally feasible photodissociation problem while obeying all the symmetry restrictions of the molecule. Also, the angular dependence is chosen so that upon bending, the degeneracies of the $B^1\Delta$ and $C^1\Pi$ states are lifted as in the real molecule. The potential energy operator derived here also reproduces the analytical long-range potential energy surfaces. In Sections 6.4 and 6.5, the details of the calculations of the bound states, dissociative states, and photodissociation cross section are given. Section 6.6 gives parametrization of the model surfaces and the results of the calculations. A summary and outlook is given in section 6.7.

6.2   Hamiltonian

The N_2O molecule is described using the Jacobi coordinates $(\mathbf{r}, \mathbf{s})$, where $\mathbf{r}$ is the vector connecting the nitrogen atoms and $\mathbf{s}$ points from the center of mass of N_2 to the oxygen atom. A sketch of the coordinate system is given in Figure 6.1. In polar coordinates, the Jacobi vectors can be written as:

$$\mathbf{s} = s\mathbf{R}(\alpha, \beta, 0)\mathbf{e}_Z \equiv s\hat{\mathbf{s}} \tag{6.4}$$

$$\mathbf{r} = r\mathbf{R}(\alpha, \beta, 0)\mathbf{R}(\phi, \theta, 0)\mathbf{e}_Z \equiv r\mathbf{R}(\phi', \theta', 0)\mathbf{e}_Z \equiv r\hat{\mathbf{r}}, \tag{6.5}$$
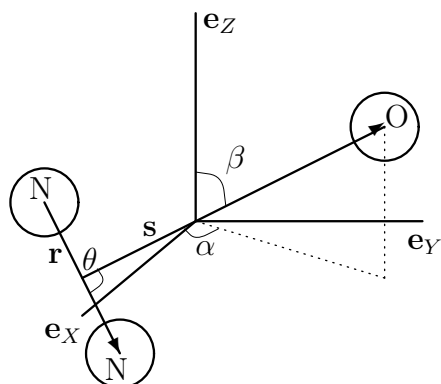
Figure 6.1: A sketch of the Jacobi coordinate system in the center of mass laboratory frame. The angle ϕ is the azimuthal angle of the $N-N$ axis in the 2-angle embedded body fixed frame and is not depicted here.

where $\mathbf{e}_Z$ is the unit vector pointing in the direction of the laboratory Z axis, α and β are the azimuthal and polar angle of the scattering coordinate $\mathbf{s}$ in the space fixed frame, $\theta = \cos^{-1}(\mathbf{s}\cdot\mathbf{r})/(sr)$ is the angle between $\mathbf{s}$ and $\mathbf{r}$ and ϕ is the azimuth of the N-N axis in the two-angle embedded body-fixed frame. We also defined $s = ||\mathbf{s}||$ and $r = ||\mathbf{r}||$, and the $\mathbf{R}(\cdot,\cdot,\cdot)$ are rotation matrices in the Euler parametrization. If the distance between the nitrogen atoms is kept fixed at r_0, the generalized Born-Oppenheimer Hamiltonian operator in this coordinate system can be written as:

$$\hat{H} = \frac{-\hbar^2}{2\mu s}\frac{d^2}{ds^2}s + \frac{\hat{\mathbf{j}}^2}{2mr_0^2} + \frac{\hat{\mathbf{l}}^2}{2\mu s^2} + \hat{V}(\mathbf{r},\mathbf{s}). \tag{6.6}$$

The term "generalized" signifies that the potential energy operator $\hat{V}(\mathbf{r},\mathbf{s})$ can couple different electronic states[197]. Furthermore, $\hat{\mathbf{j}}$ is the end-over-end angular momentum operator for the nitrogen molecule, acting on angles ϕ' and θ', $\hat{\mathbf{l}}$ is the nuclear angular momentum operator acting on α and β, m is the reduced mass of N_2, and $\mu = m_O m_{N_2}/(m_O + m_{N_2})$.

Here, the fragmentation of N_2O into $N_2(^1\Sigma^+)$ and $O^1(D_2)$ is studied. Both fragments have zero total spin and the electronic state of the nitrogen molecule is spatially nondegenerate. It follows that there are five adiabatic Born-Oppenheimer potentials correlating with the $O(^1D_2)$ limit. Namely one for each diabatic oxygen state $|\lambda\mu\rangle$, where $\lambda = 2$ is the total orbital angular momentum quantum number of the electrons of the oxygen atom after dissociation, and $\mu = -2, -1, \ldots, 2$ it's projection quantum number on the laboratory Z-axis. For future reference, we note that the electronic

wave functions $\varphi_{\lambda\mu}(\mathbf{v}) = \langle \mathbf{v}|\lambda\mu\rangle$ have the following property under change of coordinate system:

$$\varphi_{\lambda\mu}(\mathbf{v}') = \hat{R}^\dagger(\alpha,\beta,0)\varphi_{\lambda\mu}(\mathbf{v}) = \sum_{\omega_\lambda} \varphi_{\lambda\omega_\lambda}(\mathbf{v})D^{(\lambda)*}_{\mu\omega_\lambda}(\alpha,\beta,0), \qquad (6.7)$$

or:

$$\hat{R}^\dagger(\alpha,\beta,0)|\lambda\mu\rangle = \sum_{\omega_\lambda} |\lambda\omega_\lambda\rangle D^{(\lambda)*}_{\mu\omega_\lambda}(\alpha,\beta,0). \qquad (6.8)$$

Here, $\hat{R}(\cdot,\cdot,\cdot)$ are rotation operators in Euler parametrization, $\mathbf{v}$ and $\mathbf{v}'$ are (spin)coordinate vectors represented in the body fixed and space fixed frames respectively, and ω_λ is the projection of λ on the molecule fixed z-axis. The $\mathbf{D}^{(\lambda)}$ is Wigner's rotation matrix of order λ. Using the above notation, the potential energy operator can be written as

$$\hat{V}(\mathbf{r},\mathbf{s}) = \sum_{\mu\mu'} V^{(\lambda)}_{\mu\mu'}(\mathbf{r},\mathbf{s})|\lambda\mu\rangle\langle\lambda\mu'|. \qquad (6.9)$$

In the next section, an explicit basis set expansion for $V^{(\lambda)}_{\mu\mu'}$ is developed.

6.2.1 Potential energy operator

In the absence of external fields, the interaction $\hat{V}(\mathbf{r},\mathbf{s})$ between the atom and diatom depends only on the relative positions of the fragments, and not on the overall orientation of the system. So we demand that

$$\hat{V}(\mathbf{R}\mathbf{r},\mathbf{R}\mathbf{s}) = \hat{R}^\dagger\hat{V}(\mathbf{r},\mathbf{s})\hat{R} = \hat{V}(\mathbf{r},\mathbf{s}). \qquad (6.10)$$

Note that rotation of $\mathbf{r}$ and $\mathbf{s}$ on the left hand side of Eq. (6.10) implies a rotation of the electronic coordinates, [*via* Eq. (6.9)].

A tensor operator basis which obeys property (6.10) can be constructed by generating a complete tensor product basis for operators acting on $\hat{\mathbf{r}}$, $\hat{\mathbf{s}}$ [See Eqs. (6.4, 6.5)], and the electronic coordinates, and coupling this basis to tensors of rank zero:

$$\left[\left[\mathbf{C}^{(j)}(\hat{\mathbf{r}}) \otimes \mathbf{C}^{(l)}(\hat{\mathbf{s}})\right]^{(L)} \otimes \mathbf{T}^{(k)}(\mathbf{v}',\mathbf{w}')\right]^{(0)}_0$$
$$= \sum_{Mq} \left[\mathbf{C}^{(j)}(\hat{\mathbf{r}}) \otimes \mathbf{C}^{(l)}(\hat{\mathbf{s}})\right]^{(L)}_M \hat{T}^{(k)}_q(\mathbf{v}',\mathbf{w}')\langle LMkq|00\rangle, \qquad (6.11)$$

where $\langle\cdots\cdots|\cdots\rangle$ is a Clebsch-Gordan coefficient. We introduce the notation $\mathbf{C}^{(l)} = \{C_{lm_l}; m_l = -l, -l+1\ldots l\}$, and likewise for $\mathbf{C}^{(j)}$ and $\mathbf{T}^{(k)}$.

The C_{lm} are spherical harmonics in Racah normalization, and $\mathbf{v}'$ and $\mathbf{w}'$ are (spin)electronic coordinates in the space-fixed frame as defined in the previous paragraph. Furthermore, we have

$$\left[\mathbf{C}^{(j)}(\hat{\mathbf{r}}) \otimes \mathbf{C}^{(l)}(\hat{\mathbf{s}})\right]_M^{(L)} = \sum_{m_j m_l} C_{jm_j}(\hat{\mathbf{r}})C_{lm_l}(\hat{\mathbf{s}})\langle jm_j lm_l|LM\rangle. \tag{6.12}$$

The electronic part of the tensor operator basis is given by $\hat{T}_q^{(k)}(\mathbf{v}', \mathbf{w}') = \langle \mathbf{v}'|\hat{T}_q^{(k)}|\mathbf{w}'\rangle$ with

$$\hat{T}_q^{(k)} = \sum_{\mu\mu'} |\lambda\mu\rangle\langle\lambda\mu'|(-1)^{k-\mu'}\langle\lambda\mu\lambda-\mu'|kq\rangle. \tag{6.13}$$

Using Eqs. (6.4), (6.5), and (6.7) and the transformation property of a tensor operator, we can separate overall from internal rotation:

$$\left[\left[\mathbf{C}^{(j)}(\hat{\mathbf{r}}) \otimes \mathbf{C}^{(l)}(\hat{\mathbf{s}})\right]^{(L)} \otimes \mathbf{T}^{(k)}(\mathbf{v}', \mathbf{w}')\right]_0^{(0)}$$

$$= \left[\left[\mathbf{C}^{(j)}(\theta, \phi) \otimes \mathbf{C}^{(l)}(\mathbf{e}_Z)\right]^{(L)} \otimes \mathbf{T}^{(k)}(\mathbf{v}, \mathbf{w})\right]_0^{(0)} D_{00}^{(0)}(\alpha, \beta, 0)$$

$$= \sum_q C_{jq}(\theta, \phi)\hat{T}_q^k(\mathbf{v}, \mathbf{w})\langle jql0|kq\rangle\langle kqk-q|00\rangle, \tag{6.14}$$

where $D_{00}^{(0)}(\alpha, \beta, 0) = 1$, and in the last line we used $C_{lm_l}(\mathbf{e}_Z) = \delta_{m_l 0}$ along with some properties of Clebsch-Gordan coefficients. The rotation-invariant expansion of the potential energy can now be written as:

$$\hat{V}(\mathbf{r}, \mathbf{s}) = \sum_{jlkq} v_{jlk}^{(\lambda)}(r_0, s)C_{jq}(\theta, \phi)\hat{T}_{-q}^{(k)}\langle jql0|kq\rangle\langle kqk-q|00\rangle. \tag{6.15}$$

This can be further simplified by absorbing some of the factors in the expansion coefficients:

$$\hat{V}(\mathbf{r}, \mathbf{s}) = \sum_{jkq} v_{jkq}^{(\lambda)}(r_0, s)C_{jq}(\theta, \phi)\hat{T}_{-q}^{(k)}, \tag{6.16}$$

where

$$v_{jkq}^{(\lambda)}(r_0, s) = \sum_l (-1)^{k-q}\frac{\langle jql0|kq\rangle}{\sqrt{2k+1}}v_{jlk}^{(\lambda)}(r_0, s). \tag{6.17}$$

Matrix elements $V_{\mu,\mu'}^{(\lambda)}$ can be found using Eqs. (6.7) and (6.13):

$$V_{\mu,\mu'}^{(\lambda)}(\mathbf{r}, \mathbf{s}) = \langle\lambda\mu|\hat{V}(\mathbf{r}, \mathbf{s})|\lambda\mu'\rangle = \sum_j v_j^{(\lambda\mu\mu')}(r_0, s)C_{j(\mu'-\mu)}(\theta, \phi), \tag{6.18}$$

with:

$$v_j^{(\lambda\mu\mu')}(r_0, s) = \sum_k (-1)^{\lambda-\mu} \langle\lambda\mu\lambda -\mu'|kq\rangle v_{jkq}^{(\lambda)}(r_0, s). \tag{6.19}$$

Equation (6.18) is general for any atom-molecule system with the molecule in a $^1\Sigma_g^+$ state. Using Eq. (6.17) and $C_{j\mu'-\mu}(\theta, \phi) = C_{j(\mu'-\mu)}(\theta, 0)e^{i(\mu'-\mu)\phi}$ we can write:

$$\hat{V}_{\mu\mu'}^{(\lambda)}(\mathbf{r}, \mathbf{s}) = \hat{V}_{\mu\mu'}^{(\lambda)}(\theta, \phi, s) = \hat{V}_{\mu\mu'}^{(\lambda)}(\theta, s)e^{i(\mu'-\mu)\phi}. \tag{6.20}$$

6.2.2   Symmetry properties

In the linear configuration, the N_2O molecule has $C_{\infty v}$ symmetry which is reduced to C_s upon bending. In the T-shaped geometry the symmetry increases again to C_{2v}. The only conserved symmetry which applies in all configurations is $\hat{\sigma}(xz)$: reflection in the molecular xz-plane. The action of $\hat{\sigma}(xz)$ on the electronic wave function $|\lambda\mu\rangle$ is given by:

$$\hat{\sigma}(xy)|\lambda\mu\rangle = (-1)^{p+\lambda-\mu}|\lambda -\mu\rangle, \tag{6.21}$$

where $p = 0$ is the parity of the asymptotic $O(^1D_2)$ atom. A symmetry-adapted basis of types A' (symmetric) and A'' (antisymmetric) is thus given by[197]:

$$A' \quad \begin{cases} |0\rangle &= |\lambda 0\rangle, \\ |\mu+\rangle &= \frac{1}{\sqrt{2}}\left[|\lambda -\mu\rangle + (-1)^{\lambda-\mu}|\lambda\mu\rangle\right] \end{cases} \tag{6.22}$$

$$A'' \quad \begin{cases} |\mu-\rangle &= \frac{-i}{\sqrt{2}}\left[|\lambda -\mu\rangle - (-1)^{\lambda-\mu}|\lambda\mu\rangle\right]. \end{cases} \tag{6.23}$$

In this basis, the 5×5 electronic potential energy matrix splits into a 3×3 block of A' and a 2×2 block of A'' symmetry. In Table 6.1 a correlation diagram is shown for the electronic states of N_2O in different symmetries. Since the potential energy operator is Hermitian, there are 15 independent matrix elements in a real representation. This number is reduced to 9 independent matrix elements in C_{2v} symmetry. Explicit symmetry relations for the potential energy matrix elements are given by Zeimen et al.[197].

6.2.3   Long range potential

In the limit of large s, the form of the potential is given analytically by the long range multipole expansion. The multipole expansion for an atom-diatom system has recently been discussed by Brouard et al.[59,195] in the

Table 6.1: Correlation diagram for the diabatic electronic states of N_2O in different symmetries. The subscript notation in $C_{\infty v}$ symmetry indicates the symmetry under reflection in the molecular xz-plane. For example: $\hat{\sigma}(xz)|C^1\Pi_{yz+zy}\rangle = |C^1\Pi_{\hat{\sigma}(xz)(yz+zy)}\rangle = |C^1\Pi_{-(yz+zy)}\rangle = -|C^1\Pi_{yz+zy}\rangle$.

Linear		bent		T-shaped	
$C_{\infty v}$		C_s		C_{2v}	Notation
$C^1\Pi_{yz+zy}$	$\rightarrow$	$2A''$	$\rightarrow$	$1B_1$	$\Pi(2A'';1B_1)$
$C^1\Pi_{xz+zx}$	$\rightarrow$	$3A'$	$\rightarrow$	$1B_2$	$\Pi(3A';1B_2)$
$B^1\Delta_{xy+yx}$	$\rightarrow$	$1A''$	$\rightarrow$	$1A_2$	$\Delta(1A'';1A_2)$
$B^1\Delta_{x^2-y^2}$	$\rightarrow$	$2A'$	$\rightarrow$	$2A_1$	$\Delta(2A';2A_1)$
$X^1\Sigma^+_{z^2}$	$\rightarrow$	$1A'$	$\rightarrow$	$1A_1$	$\Sigma^+(1A';1A_1)$

context of $SO_2 + \hbar\omega \rightarrow SO(^3\Sigma^-) + O(^3P)$ and $O_3 + \hbar\omega \rightarrow O_2(^3\Sigma^-_g) + O(^1D)$ photodissociation reactions.

Since both the N_2 and the oxygen fragment have no dipole moment, the leading term in the expansion for $N_2(^1\Sigma^+_g)$-$O(^1D_2)$ scattering is the quadrupole-quadrupole interaction. Using Eq. (13) in Brouard *et al.*[59], the 5×5 quadrupole-quadrupole interaction matrix in the diabatic basis $\{|2\mu\rangle; -2 \leq \mu \leq 2\}$ reads:

$$\mathbf{V}_Q(\theta, s) = \frac{Q_{N_2}Q_O}{s^5}$$

$$\times \begin{bmatrix} -6c_{20} & 2\sqrt{6}c_{21} & -c_{22} & 0 & 0 \\ 2\sqrt{6}c_{21} & 3c_{20} & 2c_{21} & -\frac{\sqrt{6}}{2}c_{22} & 0 \\ -c_{22} & 2c_{21} & 6c_{20} & -2c_{21} & -c_{22} \\ 0 & -\frac{\sqrt{6}}{2}c_{22} & -2c_{21} & 3c_{20} & -2\sqrt{6}c_{21} \\ 0 & 0 & -c_{22} & -2\sqrt{6}c_{21} & -6c_{20} \end{bmatrix}, \qquad (6.24)$$

where we use the notation $c_{lm} = c_{lm}(\theta) = C_{lm}(\theta, 0)$. In the symmetry-adapted basis $\{|0\rangle, |\mu+\rangle, |\mu-\rangle, \mu = 1, 2\}$ we have $\mathbf{V}_Q = \mathbf{V}_Q^{A'} \oplus \mathbf{V}_Q^{A''}$, where:

$$\mathbf{V}_Q^{A'}(\theta, s) = \frac{Q_{N_2}Q_O}{s^5} \begin{bmatrix} 6c_{20} & 2\sqrt{2}c_{21} & -\sqrt{2}c_{22} \\ 2\sqrt{2}c_{21} & 3c_{20} + \sqrt{\frac{3}{2}}c_{22} & 2\sqrt{6}c_{21} \\ -\sqrt{2}c_{22} & 2\sqrt{6}c_{21} & -6c_{20} \end{bmatrix} \qquad (6.25)$$

$$\mathbf{V}_Q^{A''}(\theta, s) = \frac{Q_{N_2}Q_O}{s^5} \begin{bmatrix} 3c_{20} - \sqrt{\frac{3}{2}}c_{22} & 2\sqrt{6}c_{21} \\ 2\sqrt{6}c_{21} & -6c_{20} \end{bmatrix}. \qquad (6.26)$$

Here, Q_O and Q_{N_2} are permanent quadrupole moments of $O(^1D_2)$ and $N_2O(X^2\Sigma^+)$,

respectively. They can be written in terms of expectation values of (body-fixed) components of the quadrupole operator $\hat{\mathbf{Q}}^{(2)} = \{\hat{Q}_{-2}^{(2)}, \hat{Q}_{-1}^{(2)}, \dots \hat{Q}_{2}^{(2)}\}$:

$$Q_{N_2} = \langle\Sigma_g^+|\hat{Q}_0^{(2)}|\Sigma_g^+\rangle \tag{6.27}$$

$$Q_O = \langle\lambda 0|\hat{Q}_0^{(2)}|\lambda 0\rangle, \tag{6.28}$$

where $|\Sigma_g^+\rangle$ and $|\lambda\omega_\lambda\rangle$ have been defined above. The values of Q_O and Q_{N_2} are obtained from electronic structure calculations with the MOLPRO program package[79]. A value of $Q_O = 0.86727244$ au is obtained using wave functions computed at the CASSCF level using an aug-cc-p-V6Z basis set. A value of $Q_{N_2} = -1.05948221$ au at the $N-N$ equilibrium separation of 2.13199 a_0 is determined with CCSD(T) calculations in an aug-cc-pV5Z one-electron basis set, using the finite field method.

6.2.4 Model potential

We construct model potential energy surfaces for the dynamics calculations. For a realistic description, our model potential must have at least the following four properties: first, in the linear configuration the Π and Δ states must be two-fold degenerate, and the energy-ordering of Σ^+, Π, and Δ states must be the same as in N_2O. Second, as the molecule bends away from $\theta = 0$, the degeneracy of the Π and Δ states with different $\hat{\sigma}(xz)$ symmetry must be lifted as in N_2O, and in T-shaped geometry ($\theta = \pi/2$) the system must also have $\hat{\sigma}(xy)$ symmetry. Third, the Π and Δ states must be repulsive at all s, and the Σ^+ ground state must support bound states, and fourth, the quadrupole-quadrupole interaction must be retrieved exactly for large s.

The short-range electronic potential energy surfaces are most easily modeled in the adiabatic basis. In Eqs. (6.24) to (6.26) the long-range potential energy matrix is given in the diabatic (symmetry-adapted) basis. The adiabatic basis is by definition the basis where the matrix $\mathbf{V}(\theta, s)$ is diagonal, so we also need a model unitary transformation between diabatic and adiabatic states. In the long range, this transformation can be written as:

$$\mathbf{V}_Q(\theta, s) = \frac{Q_{N_2}Q_O}{s^5}\mathbf{U}(\theta)\mathbf{\Lambda}(\theta)\mathbf{U}^\dagger(\theta), \tag{6.29}$$

where $\mathbf{\Lambda}$ is the diagonal matrix containing the θ-dependent potentials $\lambda^\gamma(\theta)$, where γ labels the adiabatic electronic states, and $\mathbf{U}$ is a unitary matrix that transforms between the diabatic and adiabatic bases. The matrices in Eqs. (6.25) and (6.26) can be diagonalized analytically, and the eigenvalues $\lambda^\gamma(\theta)$

Table 6.2: Model functions for the short-range potential. See Eq. (6.38)

γ	$f^\gamma(s)$	$g^\gamma(\theta)$
$1A'$	$\frac{1}{6}\{D_e[1-\exp\{-(s-s_e)\}]^2-D_e\}$	$6-a_1\sin^2\{\cos^{-1}(\cos^n\theta)\}$
$2A'$	$(s-2)^{-1}\exp\{s-s_1\}$	$-3+a_2\sin^2\theta$
$3A'$	$(s-2)^{-1}\exp\{s-s_2\}$	$3-a_2\sin^2\theta$
$2A''$	$f^{3A'}(s)$	$\lambda^{2A''}(\theta)$
$1A''$	$f^{2A'}(s)$	$\lambda^{1A''}(\theta)$

are given by:

$$\lambda^{1A'}_{2A'}(\theta) = \pm\left[36c_{20}(\theta)^2+32c_{21}(\theta)^2+2c_{22}(\theta)^2\right]^{1/2} \tag{6.30}$$

$$\lambda^{3A'}(\theta) = \frac{\sqrt{6}}{2}\left[\sqrt{6}c_{20}(\theta)+c_{22}(\theta)\right] \tag{6.31}$$

$$\lambda^{1A''}_{2A''}(\theta) = -\frac{3}{2}c_{20}(\theta)-\frac{\sqrt{6}}{4}c_{22}(\theta)$$

$$\pm\frac{1}{4}\left[\{18c_{20}(\theta)-\sqrt{6}c_{22}(\theta)\}^2+384c_{21}(\theta)^2\right]^{1/2}. \tag{6.32}$$

We label the eigenvalues with the unique C_s symmetry-labels and not with the full labels given in Table 6.1 to avoid cluttering. Just as the potential in Eqs. (6.25) and (6.26), the transformation matrix $\mathbf{U}(\theta)$ splits in two parts: $\mathbf{U}=\mathbf{U}^{A'}\oplus\mathbf{U}^{A''}$. For the A' surfaces, the transformation matrices $\mathbf{U}^{A'}$ can be written in terms of its columns $\mathbf{u}'$: $\mathbf{U}^{A'}=[\mathbf{u}'_1\mathbf{u}'_2\mathbf{u}'_3]\mathbf{N}'$, with:

$$u'_{1i}(\theta) = 1 \tag{6.33}$$

$$u'_{2i}(\theta) = \frac{\lambda_i(\theta)+\sqrt{2}c_{22}(\theta)u_{3i}-6c_{20}(\theta)}{2\sqrt{2}c_{21}(\theta)} \tag{6.34}$$

$$u'_{3i}(\theta) = \frac{\sqrt{2}c_{22}(\theta)-\sqrt{3}\lambda_i(\theta)+6\sqrt{3}c_{20}(\theta)}{\sqrt{6}c_{22}(\theta)-6c_{20}(\theta)-\lambda_i(\theta)}, \tag{6.35}$$

where $i=1,2,3$ labels the columns and and $N'_{ij}=\delta_{ij}N'_{ii}$ contains the θ-dependent normalization factors for the column vectors $\mathbf{u}'_i$. For the A'' surfaces, we similarly have $\mathbf{U}^{A''}=[\mathbf{u}''_1\mathbf{u}''_2]\mathbf{N}''$, with:

$$u''_{1i}(\theta) = 1 \tag{6.36}$$

$$u''_{2i}(\theta) = \frac{\lambda_i(\theta)-[3c_{20}(\theta)-\sqrt{3/2}c_{22}(\theta)]}{2\sqrt{6}c_{21}(\theta)}. \tag{6.37}$$

With the use of Eq. (6.29), we model the diabatic potential energy surfaces

as follows:

$$\mathbf{V}(\theta, s) = \mathbf{U}(\theta) \left[w_-(s)\mathbf{F}(s) + w_+(s)Q_{N_2}Q_O s^{-5}\mathbf{1} \right]$$
$$\times \left[w_-(s)\mathbf{G}(\theta) + w_+(s)\boldsymbol{\Lambda}(\theta) \right] \mathbf{U}^\dagger(\theta). \tag{6.38}$$

Here, the $w_\pm(s)$ are switching functions of the form:

$$w_\pm(s) = \tfrac{1}{2}\{1 + \tanh[\pm\alpha(s - s_0)]\}, \tag{6.39}$$

where s_0 determines the point where the quadrupole-quadrupole interaction becomes effective, and α determines the smoothness of the transition. In Eq. (6.38), $\mathbf{1}$ denotes the 5×5 identity matrix. The $\mathbf{F}$ and $\mathbf{G}$ are diagonal matrices whose non-zero elements are the short range potential energy functions $f^\gamma(s)$ and $g^\gamma(\theta)$, respectively. The $f^\gamma(s)$ and $g^\gamma(s)$ have been chosen as simple as possible, while obeying the restrictions mentioned at the beginning of this paragraph. They are summarized in Table 6.2. It is easily verified that Eq. (6.38) returns to the quadrupole interaction matrix in Eq. (6.29) for large s. At small internuclear distances ($s < s_0$), the s-dependent part of the $\Sigma(1A'; 1A_1)$ ground state potential is a Morse potential, where the parameters s_e and D_e determine the potential equilibrium distance and binding energy. In $g^{1A'}(\theta)$, the parameter $0 < a_1 < 6$ determines the height of the barrier at $\theta = \pi/2$. Larger a_1 gives a higher barrier. The width (in θ) of the potential is controlled with n, where smaller n yields a wider potential, allowing the molecule to bend over wider ranges of θ. The $\Pi(3A'; 1B_2)$ and $\Pi(1A''; 1B_1)$, and $\Delta(2A'; 2A_1)$ and $\Delta(1A''; 1A_2)$ are degenerate at $\theta = 0$, and the degeneracy is lifted at nonlinear geometry. In the inner region, these states are given by Yukawa-like potentials, to ensure a repulsive wall in the inner region. The repulsive walls are controlled by parameters s_1 and s_2 in $f^{2A'}(s)$ and $f^{3A'}(s)$. Smaller (possibly negative) s_1 and s_2 shift the repulsive wall to smaller distances s. The $\Pi(3A'; 1B_2)$ state is repulsive everywhere, but contains a minimum in θ at $\theta = \pi/2$. The parameter $0 < a_2 < 3$ controls the depth of that minimum. Values $a_2 > 3$ give rise to an unphysical deep minimum in the $\Pi(3A'; 1B_2)$ state at $\theta = \pi/2$. In Fig. (6.2) we plot the potentials and indicate the influence of some of the parameters.

6.3   Model dipole moment surfaces

In order to model the photoexcitation process from ground to excited state electronic surfaces, we develop model electronic dipole moment surfaces. The dipole moment rotates as a spherical tensor of rank one, and thus we find
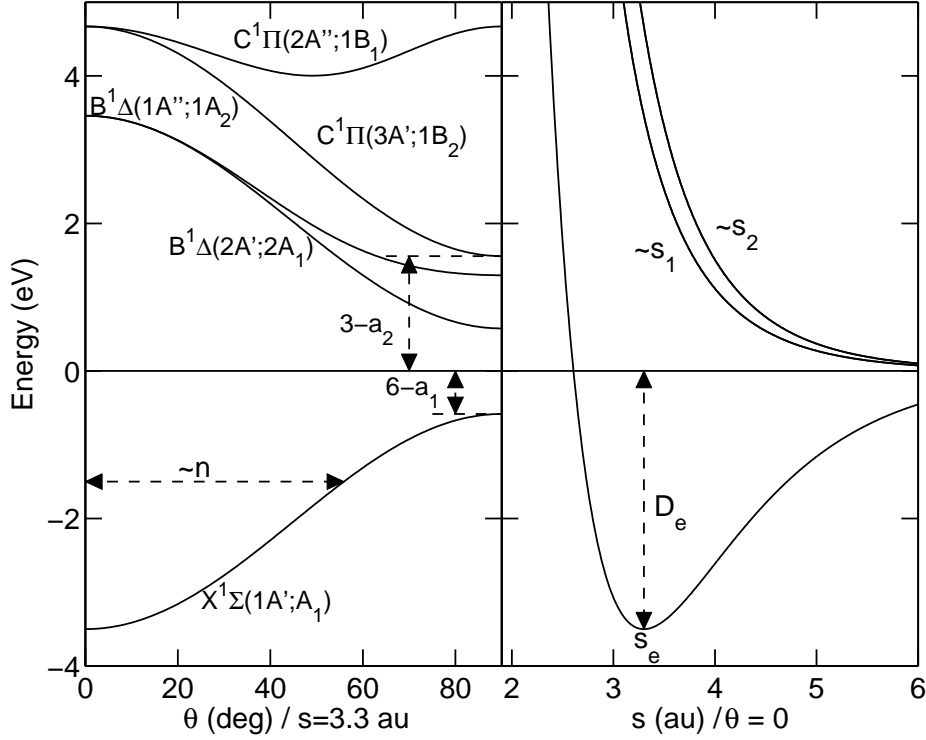
Figure 6.2: The adiabatic model potentials and parameters as a function of s and θ, see Eq. (6.38) and Table 6.2. The arrows indicate the value of the parameters shown in the plot, except when a parameter is prefixed with a $\sim$. The $\sim$ should be read as "is controlled by". In this particular plot we have $D_e = 3.5$, $n = 1$, $(a_1, a_2) = (5, 2)$, $(s_e, s_1, s_2) = (3.3, 1.8, 1.5)$, and $(s_0, \alpha) = (9, 3)$.

body-fixed angular basis functions by coupling $\hat{\mathbf{r}}$- and $\hat{\mathbf{s}}$ dependent angular basis functions and separating overall rotation from internal rotation:

$$
\left[\mathbf{C}^{(j)}(\hat{\mathbf{r}}) \otimes \mathbf{C}^{(l)}(\hat{\mathbf{s}})\right]_t^{(1)} = \sum_q \left[\mathbf{C}^{(j)}(\theta, \phi) \otimes \mathbf{C}^{(l)}(\vec{e_z})\right]_q^{(1)} D_{tq}^{(1)*}(\alpha, \beta, 0)
$$

$$
= \sum_s C_{jq}(\theta, \phi) \langle jql0|1q \rangle D_{tq}^{(1)*}(\alpha, \beta, 0). \tag{6.40}
$$

Here, we used Eqs. (6.4) and (6.5). It follows that molecule fixed components of the dipole operator can be expanded as:

$$
\begin{aligned}
\hat{d}_q^{(1)\gamma\gamma'}(s, \theta, \phi) &= \sum_{jl} n_{lj}^{\gamma\gamma'q}(s) \langle jql0|1q \rangle C_{jq}(\theta, \phi) \\
&\equiv \sum_j n_j^{\gamma\gamma'q}(s) C_{jq}(\theta, \phi), \tag{6.41}
\end{aligned}
$$

Table 6.3: Symmetry conditions and expansion coefficients for the components of the dipole operator in the adiabatic representation.

$\langle\gamma\|\hat{d}\|0\rangle$ $\;\;\;\;\|0\rangle = \|\Sigma(1A';1A_1)\rangle$	conditions			model function		
	linear	bent	T-shaped	$n_0^{\gamma 0q}$	$n_1^{\gamma 0q}$	$n_2^{\gamma 0q}$
$\langle\Sigma(1A';1A_1)\|\hat{d}_{\pm 1}\|0\rangle$	0	$\neq 0$	$\neq 0$	0	± 1	0
$\langle\Pi(3A';1B_2)\|\hat{d}_{\pm 1}\|0\rangle$	$\neq 0$	$\neq 0$	0	$\pm\frac{1}{3}$	$\frac{\sqrt{2}}{3}$	0
$\langle\Delta(2A';2A_1)\|\hat{d}_{\pm 1}\|0\rangle$	0	$\neq 0$	$\neq 0$	0	1	0
$\langle\Pi(2A'';1B_1)\|\hat{d}_{\pm 1}\|0\rangle$	$\neq 0$	$\neq 0$	$\neq 0$	1	0	0
$\langle\Delta(1A'';1A_2)\|\hat{d}_{\pm 1}\|0\rangle$	0	$\neq 0$	0	0	0	± 1
$\langle\Sigma(1A';1A_1)\|\hat{d}_0\|0\rangle$	$\neq 0$	$\neq 0$	0	0	1	0
$\langle\Pi(3A';1B_2)\|\hat{d}_0\|0\rangle$	0	$\neq 0$	0	$\frac{-1}{\sqrt{14}}$	$\frac{3}{\sqrt{14}}$	$-\sqrt{\frac{2}{7}}$
$\langle\Delta(2A';1A_1)\|\hat{d}_0\|0\rangle$	$\neq 0$	$\neq 0$	0	0	1	0
$\langle\Pi(2A'';1B_1)\|\hat{d}_0\|0\rangle$	0	0	0	0	0	0
$\langle\Delta(1A'';1A_2)\|\hat{d}_0\|0\rangle$	0	0	0	0	0	0

where we defined the s-dependent expansion coefficients $n_j^{\gamma\gamma'q}(s)$. The γ and γ' label adiabatic electronic states, and we have $-1 \leq q \leq 1$. Since all electronic (transition) dipole moments vanish as $s \to \infty$, we use the following simple s-dependence:

$$n_j^{\gamma\gamma'q}(s) = n_j^{\gamma\gamma'q} e^{-(s-s_e)^2}, \tag{6.42}$$

where s_e is the equilibrium distance of the electronic ground state (see also the previous subsection), and the $n_j^{\gamma\gamma'q}$ do not depend on s.

The values of $n_j^{\gamma\gamma'q}$ are restricted by symmetry rules imposed by the point group symmetry of the molecule in linear, bent and T-shaped configurations. For example, excitation from the $\Sigma(1A'; A_1)$ to the $\Delta(2A'; 2A_1)$ state is forbidden in linear geometry, but becomes allowed upon bending of the molecule. In the first four columns of Table 6.3, the conditions imposed by the point group symmetry for different geometries of the molecule are shown for each component of the dipole operator, for transitions from the adiabatic electronic ground state to excited states. The conditions on the value of components of the dipole operator at various angles allow us to set up systems of linear equations to determine the coefficients $n_j^{\gamma\gamma'q}$ with $j = 1, 2, 3$. The results are shown in columns 5-7 of Table 6.3, and in Fig. 6.2 the absolute magnitudes $|\hat{\mathbf{d}}^{(1)\gamma\gamma'}| = \sum_q (d_q^{(1)\gamma\gamma'})^2$ as a function of angle are plotted. The diabatic representation of the electric dipole moment operator is obtained by
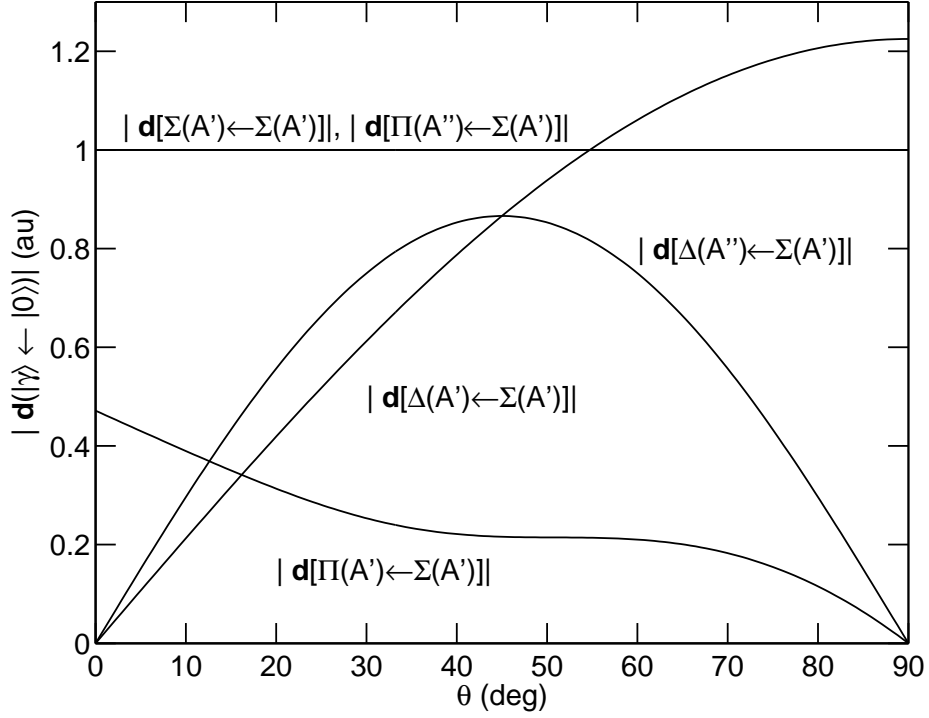
Figure 6.3: The absolute magnitude of dipole transition moment vectors, as a function of bending angle θ, at $s = s_e$.

the transformation:

$$d_q^{(1)\gamma\gamma'} = \langle\gamma|\hat{d}_q^{(1)}|\gamma'\rangle = \sum_{\omega_\lambda\omega_\lambda'}\langle\gamma|\lambda\omega_\lambda\rangle\langle\lambda\omega_\lambda|\hat{d}_q^{(1)}|\lambda\omega_\lambda'\rangle\langle\lambda\omega_\lambda'|\gamma\rangle. \qquad (6.43)$$

The matrix elements $\langle\gamma|\lambda\omega_\lambda\rangle$ are matrix elements of the matrix $\mathbf{U}(\theta)$ of section 6.2.4 (but represented in the $\{|\lambda\omega_\lambda\rangle\}$ instead of the $\{|\mu\pm\rangle\}$ basis). Since the ground state nuclear wave functions (see Sect. 6.4.1) have small amplitude at $\theta \approx \pi/2$, we here set $\mathbf{U}(\theta) = \mathbf{1}$. The transformation in Eq. (6.22) is then the effective transformation between adiabatic and diabatic states. After applying this transformation, we can write:

$$d_q^{(1)\omega_\lambda\omega_\lambda'} = \langle\lambda\omega_\lambda|\hat{d}_q^{(1)}|\lambda\omega_\lambda'\rangle = \sum_k n_k^{\omega_\lambda\omega_\lambda'}(s)C_{k(\omega_\lambda'-\omega_\lambda)}(\theta,\phi). \qquad (6.44)$$

Using that for the ground state the adiabatic state $\gamma = 0$ equals the diabatic state $|\lambda0\rangle$, the full electronic transition dipole vector functions in the $\{|\lambda\omega_\lambda\rangle$

basis are given by:

$$
\mathbf{d}_{\pm 1}^{(1)} =
\begin{bmatrix}
\frac{1}{\sqrt{2}}\{C_{1\pm 1}(\theta,\phi) - iC_{2\pm 1}(\theta,\phi)\} \\
\frac{1\pm 3i}{3\sqrt{2}} + \frac{1}{3}C_{1\pm 1}(\theta,\phi) \\
\pm C_{1\pm 1}(\theta,\phi) \\
\mp \frac{1\pm 3i}{3\sqrt{2}} - \frac{1}{3}C_{1\pm 1}(\theta,\phi) \\
\frac{1}{\sqrt{2}}\{C_{1\pm 1}(\theta,\phi) \mp iC_{2\pm 1}(\theta,\phi)\}
\end{bmatrix}
e^{-(s-s_0)^2},
\tag{6.45}
$$

and

$$
\mathbf{d}_0^{(1)} =
\begin{bmatrix}
\frac{1}{\sqrt{2}}C_{10}(\theta,\phi) \\
\frac{-1}{2\sqrt{7}}\{C_{00}(\theta,\phi) - 3C_{10}(\theta,\phi) + 2C_{10}(\theta,\phi)\} \\
C_{10}(\theta,\phi) \\
\frac{1}{2\sqrt{7}}\{C_{00}(\theta,\phi) - 3C_{10}(\theta,\phi) + 2C_{10}(\theta,\phi)\} \\
\frac{1}{\sqrt{2}}C_{10}(\theta,\phi)
\end{bmatrix}
e^{-(s-s_0)^2}.
\tag{6.46}
$$

6.4 Wave functions

6.4.1 Bound states

The bound state wave functions can be expanded in the following basis functions:

$$
|\psi_{v\nu}^{LM_L}\rangle = \sum_{nj\omega_j} c_{nj\omega_j}^{Lv\nu} |nLM_L j\omega_j; 0\rangle,
\tag{6.47}
$$

where v labels the s-stretching mode and ν the θ-bending mode. The total nuclear angular momentum quantum number is indicated by L, and its projection on the space fixed Z-axis by M_L. The basis functions are given by:

$$
|nLM_L j\omega_j; 0\rangle =
$$
$$
s^{-1}f_n(s)\sqrt{\frac{2L+1}{4\pi}} D_{M_L\omega_j}^{(L)*}(\alpha,\beta,0)|j\omega_j\rangle|0\rangle.
\tag{6.48}
$$

Here, $|0\rangle$ labels the ground state adiabatic electronic wave function [see Eq. (6.22)]. The $|j\omega_j\rangle$ are end-over-end rotational eigenfunctions of the N_2 fragment, where ω_j labels the projection of $\mathbf{j}$ on the molecule fixed z-axis, and $s^{-1}f_n(s)$ is a Morse oscillator eigenfunction. In the bound state calculations we neglect coupling between different electronic states, since in the short range the energy difference between the ground and excited states is large

compared to terms coupling these states. Neglecting long-range terms, it follows that the Hamiltonian matrix elements for N_2O in the electronic ground state are given by:

$$
\langle nLM_Lj\omega_j; 0|\hat{H}|n'L'M_{L'}j'\omega_{j'}; 0\rangle =
$$
$$
\delta_{LL'}\delta_{M_LM_{L'}}\left\{\frac{-\hbar^2}{2\mu}\langle n|\frac{1}{s}\frac{\partial^2}{\partial s^2}s|n'\rangle\delta_{jj'}\delta_{\omega_j\omega_{j'}}\right.
$$
$$
+b_0j(j+1)\delta_{nn'}\delta_{jj'}\delta_{\omega_j\omega_{j'}} + C^-_{L\omega_{j'}}C^-_{j\omega_{j'}}\delta_{\omega_j\omega_{j'}+1} + C^+_{L\omega_{j'}}C^+_{j\omega_{j'}}\delta_{\omega_j\omega_{j'}-1}
$$
$$
\left.+\langle n|f^{1A'}(s)|n'\rangle\langle j\omega_j|\ g^{1A'}(\theta)|j'\omega_{j'}\rangle\right\}, \tag{6.49}
$$

where b_0 is the rotational constant of N_2 given by $b_0 = 1/mr_0^2$ (with m the reduced mass of the N_2 molecule), and $g^{1A'}(\theta)$ and $f^{1A'}(s)$ are defined in Table 6.2. We used that $|0\rangle = |\lambda 0\rangle$ [see Eq. (6.22)], and $C^{\pm}_{jm_j} = \sqrt{j(j+1) - m_j(m_j \pm 1)}$.

   We represent the Morse oscillator eigenfunctions $f_n(s)$ in a sinc-DVR basis[100,101]. The $f_n(s)$ are obtained by diagonalizing the sinc-DVR Hamiltonian, where the s-dependent potential is given by a cut through the short-range potential (which is a Morse potential) at $\theta = 0$. The bound state functions are then obtained by setting up and diagonalizing the Hamiltonian matrix in Eq. (6.49). We find that calculations are converged when basis sets include $|j\omega_j\rangle$ functions up to $j = 30$, and $n = 14$.

6.4.2   Continuum states

The molecule fixed photodissociation wave functions with total energy E and total angular momentum quantum number J are given by:

$$
|\psi_E^{JM_J\Omega j\omega_\lambda}\rangle = \sum_{\Omega'j'\omega'_\lambda} s^{-1} f_{\Omega'j'\omega'_\lambda}^{J\Omega j\omega_\lambda}(s; E)|JM_J\Omega'j'\lambda\omega'_\lambda\rangle. \tag{6.50}
$$

The angular functions are given by:

$$
|JM_J\Omega j\lambda\omega_\lambda\rangle = \sqrt{\frac{2J+1}{4\pi}}D_{M_J\Omega}^{(J)*}(\alpha, \beta, 0)|j\omega_j\rangle|\lambda\omega_\lambda\rangle, \tag{6.51}
$$

where $\omega_j = \Omega - \omega_\lambda$, the $|\lambda\omega_\lambda\rangle$ are diabatic electronic wave functions with ω_λ the electronic orbital angular momentum projection quantum number on the body-fixed z-axis. Furthermore, J denotes the total (electronic plus nuclear) angular momentum quantum number with space fixed projection M_J and molecule fixed projection Ω. The radial functions $\mathbf{f}_E^{J\Omega j\omega_\lambda}(s) = \{f_{\Omega'j'\omega'_\lambda}^{J\Omega j\omega_\lambda}(s; E)\}$

can be found by solving the set of coupled second order differential equations:

$$\frac{\partial^2}{\partial s^2}\mathbf{f}_E^{J\Omega j\omega_\lambda}(s) = \mathbf{W}(s; E)\mathbf{f}_E^{J\Omega j\omega_\lambda}(s). \tag{6.52}$$

Here, $\mathbf{W}(s; E)$ is the matrix of the operator $\hat{W}(s; E)$ given by

$$\hat{W}(s; E) = \frac{\hbar^2}{2\mu}[b_0\hat{\mathbf{j}}^2 + \frac{\hat{\mathbf{l}}^2}{2\mu s^2} + \hat{V}(\mathbf{r}, \mathbf{s}) - E]. \tag{6.53}$$

The matrix elements of $\hat{W}$ are given by:

$$\frac{\hbar^2}{2\mu}\langle JM_J\Omega j\lambda\omega_\lambda|\hat{W}|JM_J\Omega'j'\lambda\omega_\lambda'\rangle = -E\delta_{\Omega\Omega'}\delta_{jj'}\delta_{\omega_\lambda\omega_\lambda'}$$

$$+ \frac{-1}{2\mu s^2}\delta_{jj'}\left\{C_{J'\Omega'}^- C_{\lambda\omega_\lambda'}^- \delta_{\Omega\Omega'-1}\delta_{\omega_\lambda\omega_\lambda'-1} + C_{J'\Omega'}^+ C_{\lambda\omega_\lambda'}^+ \delta_{\Omega\Omega'+1}\delta_{\omega_\lambda\omega_\lambda'+1}\right.$$

$$+ C_{J\Omega'}^- C_{j'(\Omega'-\omega_\lambda')}^- \delta_{\Omega\Omega'-1}\delta_{\omega_\lambda\omega_\lambda'} + C_{J\Omega'}^+ C_{j'(\Omega'-\omega_\lambda')}^+ \delta_{\Omega\Omega'+1}\delta_{\omega_\lambda\omega_\lambda'}$$

$$- C_{\lambda\omega_\lambda'}^+ C_{j'(\Omega'-\omega_\lambda')}^- \delta_{\Omega\Omega'}\delta_{\omega_\lambda\omega_\lambda'+1} - C_{\lambda\omega_\lambda'}^- C_{j'(\Omega'-\omega_\lambda')}^+ \delta_{\Omega\Omega'}\delta_{\omega_\lambda\omega_\lambda'-1}$$

$$+ \left[J(J+1) + j(j+1) + \lambda(\lambda+1) + 2(\Omega\omega_\lambda - \omega_\lambda^2 - \Omega^2)\right]\delta_{\Omega\Omega'}\delta_{\omega_\lambda\omega_\lambda'}\Big\}$$

$$+ b_0j(j+1)\delta_{j'j}\delta_{\Omega\Omega'}\delta_{\omega_\lambda\omega_\lambda'} + \delta_{j'j}\delta_{\Omega\Omega'}\langle j\omega_j|\hat{V}_{\omega_\lambda\omega_\lambda'}^{(\lambda)}(\theta, \phi, s)|j'\omega_{j'}\rangle. \tag{6.54}$$

where we used that the matrix of $\hat{W}$ is block diagonal in J and M_J, and $\lambda = 2$ has only one value in this work. The potential energy operator $\hat{V}_{\omega_\lambda\omega_\lambda'}(\theta, \phi, s)$ is defined in Eq. (6.20). The radial functions in Eq. (6.52) obey the boundary conditions $\mathbf{f}_E^{J\Omega j\lambda\omega_\lambda}(0) = \mathbf{0}$. The boundary conditions for $s \to \infty$ are most conveniently written in a basis of space fixed channel eigenfunctions:

$$f_{k'j'l'}^{Jkjl}(s; E) = v_{k'j'l'}(s; E)\delta_{kk'}\delta_{jj'}\delta_{ll'} - u_{k'j'l'}(s; E)S_{k'j'l'}^{kjl*}(E; J), \tag{6.55}$$

where $\mathbf{S}(E; J)$ is the scattering matrix, and $v_{k'j'l'}(s; E)$ and $u_{k'l'j'}(s; E)$ are outgoing and incoming waves, respectively[197]. Furthermore l is the quantum number for $\hat{\mathbf{l}}^2$, and $|j - \lambda| \le k \le j + \lambda$. The transformation between the space fixed and molecule fixed functions reads:

$$\mathbf{f}_E^{J\Omega j\omega_\lambda}(s) = \sum_{kl} \mathbf{f}_E^{Jkjl}(s)\sqrt{\frac{2l+1}{2J+1}}\langle k\Omega l0|J\Omega\rangle\langle j(\Omega-\omega_\lambda)\lambda\omega_\lambda|k\Omega\rangle. \tag{6.56}$$

We determine the radial functions using the renormalized numerov propagator in the molecule fixed basis set. At the end of the grid we transform to the space fixed basis set to match the wave functions to the boundary conditions, and then transform back. The calculations can be performed in the space

fixed basis as well. However, in the space fixed basis evaluation of the W matrix becomes more cumbersome, since evaluation of the potential energy matrix then involves the transformation of Eq. (6.56). Since we are interested in ω_λ populations, working in the molecule fixed basis has conceptual advantage as well.

6.5 Cross section

The photodissociation cross section is given by:

$$\sigma_{\mathbf{fi}}(\omega) = \frac{4\pi^2 \alpha \hbar \omega}{e^2(2L+1)} \sum_{JM_J\Omega M_L} |\langle \psi_E^{JM_J\Omega j\omega_\lambda} | \boldsymbol{\epsilon} \cdot \hat{\boldsymbol{\mu}} | \psi_{v\nu}^{LM_L} \rangle|^2. \tag{6.57}$$

Initial and final state quantum numbers are indicated with $\mathbf{i}$ and $\mathbf{f}$, where $\mathbf{i} = \{L, v, \nu\}$ and $\mathbf{f} = \{j, \omega_\lambda\}$. Furthermore, α is the finestructure constant, e the elementary charge, ω the photon angular transition frequency, $\hat{\boldsymbol{\mu}}$ the electronic dipole operator and $\boldsymbol{\varepsilon}$ the photon polarization vector. The electronic dipole operator in the molecule fixed frame ($\hat{\mathbf{d}}$) is given by [see Eq. (6.40)]:

$$\hat{\mu}_t^{(1)} = \sum_s \hat{d}_s^{(1)} D_{ts}^{(1)*}(\alpha, \beta, 0). \tag{6.58}$$

We choose the space fixed laboratory center of mass $\mathbf{e}_Z$ unit vector parallel to $\boldsymbol{\varepsilon}$, so we have $\boldsymbol{\varepsilon} \cdot \hat{\boldsymbol{\mu}} = \hat{\mu}_0^{(1)}$. Using Eqs. (6.51), (6.48), and Eq. (6.50), integrating over angles α, β, θ, and ϕ, and completing the sum over M_J and M_L we get:

$$\sigma_{\mathbf{fi}}(\omega) = \frac{4\pi^2 \alpha \hbar \omega}{3e^2} \sum_{J\Omega} |\langle \psi_E^{J\Omega j\omega_\lambda} || \hat{d}^{(1)} || \psi_{v\nu}^L \rangle|^2, \tag{6.59}$$

where the reduced matrix element can be written as:

$$\langle \psi_E^{Jj\omega_\lambda} || \hat{d}^{(1)} || \psi_{v\nu}^L \rangle = \sum_{\mathcal{I}} \sqrt{\frac{2j'+1}{4\pi(2j''+1)}} \langle f_{\Omega'j'\omega_\lambda'}^{J\Omega j\omega_\lambda}(E) | n_k^{\omega_\lambda'\omega_\lambda''} | f_n \rangle c_{n''j''\omega_{j''}}^{Lv\nu}$$

$$\times \langle L\omega_{j''}1q|J\Omega'\rangle \langle j''\omega_{j''}kt|j'(\Omega'-\omega_\lambda')\rangle \langle j''0k0|j'0\rangle. \tag{6.60}$$

The index set $\mathcal{I}$ indicates the sum over all (double) primed quantum numbers, k and q: $\mathcal{I} = \{\Omega', j', \omega_\lambda', n'', j'', \omega_{j''}, k, q\}$. In the second line, the Clebsch-Gordan coefficient $\langle j''\omega_{j''}kt|j'(\Omega'-\omega_\lambda')\rangle$, results from integration over the internal angles θ and ϕ. As a consequence of the model for the diabatic to adiabatic transformation in sections 6.2.4 and 6.3, we set $t = \Omega' - \omega_\lambda' - \omega_{j''}$ if $|\Omega' - \omega_\lambda' - \omega_{j''}| \leq 1$, and $t = q$ otherwise. This way, the spatial symmetry is reflected in the calculation of the cross sections, and selection rules are obeyed.
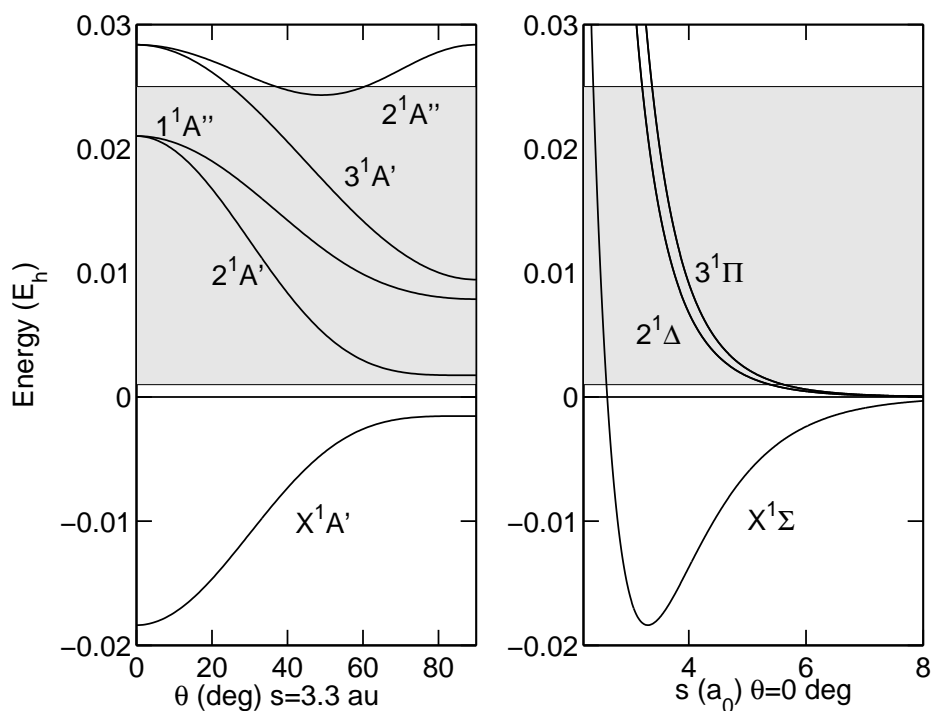
Figure 6.4: Model potential energy surfaces used in this calculation. The colored areas indicates the energy region for which scattering calculations were performed.

6.6 Results

As stated in the introduction, the central question we ask here concerns the fragment separation where the ω_λ distribution during dissociation does not change anymore. The time-independent photodissociation wave function we calculate here does not contain any direct information about the dynamics of the photodissociation process. However, we are able to extract some dynamical information by investigating the convergence of the product distribution as the propagation grid is extended. In order to minimize computational costs, we use a model potential here (see Figure 6.4 and Table 6.2) where the bound state has a relatively shallow minimum potential energy $D_e = 0.5$ eV, and a binding distance $s_e = 3.3$ a_0. Furthermore we have angular parameters $n = 2$, $a_1 = 5.5$ and $a_2 = 2$, and we use $s_1 = 0$ and $s_2 = -0.3$ for the repulsive potentials. The analytical long-range potential energy surface is switched on at 9 a_0 to ensure a smooth transition from the short-range to long-range interaction. Scattering calculations are performed at 25 dissociation energies, ranging from 0.027 to 0.68 eV (1 to 25 mE$_h$). As shown in Figure 6.4, the

range of dissociation energies is large enough to probe all dissociative surfaces. Apart from these calculations, a few calculations with "more realistic" potentials, with larger binding energy ($D_e = 3.5$), more repulsive potentials ($s_1 = 1.8$ and $s_2 = 1.5$) at higher dissociation energies were performed as well, in order to check to what extent the results depend on the choice of our parameters.

Here we look at the transition $\{J = 1, j, \omega_\lambda\} \leftarrow \{L = 0, v = 0, \nu = 0\}$.

6.6.1   Rotational distribution

In the left panel of Figure 6.5 the rotational distribution of the N$_2$ fragment (j) at the various dissociation energies are shown for the fully converged calculations. It is clear that higher dissociation energies yield higher j-levels. The maximum centers around $j = 9$ at a dissociation energy of 1 mE$_\text{h}$, and increases to $j = 48$ at $E = 25$ mE$_\text{h}$. It can be seen that at low dissociation energies, the shape of the rotational distribution varies significantly as the energy of dissociation varies, while at higher energies the distribution stays similar in shape, while the main peak shifts as a function of the energy.

In the right panelof Figure 6.5 the relative average photofragment velocity and the average fraction of energy which ends up as rotational energy is shown as a function of total dissociation energy. In experiments on N$_2$O photodissociation at high dissociation energies, more than 90% of the dissociation energy is transferred to rotation of the N$_2$ fragment. In our model this fraction runs from about 50% at low energies, to about 70% at high dissociation energies. The difference can be ascribed to the differences between the potential. Our model potential is far less anisotropic than the true N$_2$O potential. For instance, in N$_2$O the excited electronic $^1\Sigma^-(1A''; 2A_2)$ state has avoided crossings with the $^1\Delta(2A'; 2A_1)$ and $^1\Delta(1A''; 1A_2)$ states, which strongly influences the excitation and dissociation mechanism. If the bound state potential well depth is increased, the dissociative potentials are made more repulsive, and the dissociation energies increased accordingly, we also find that typically about 70% of the dissociation energy is transferred into rotation of the N$_2$ fragment.

In the experiment by Teule *et. al*[58], the photofragments were produced with relative velocities of about 1.5×10^{13} Å/s. Depending on dissociation energy, we find in our model calculations relative velocities running from about 0.5 to 2.0×10^{13} Å/s, which is quite comparable with the experiment.
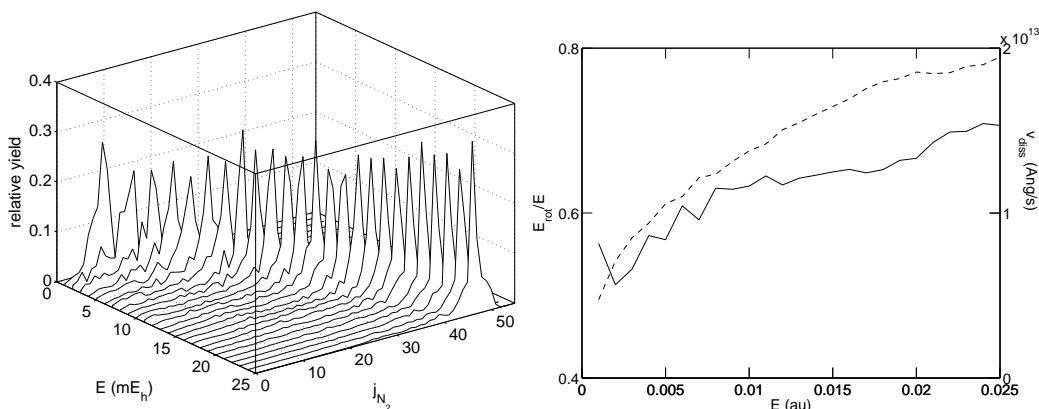
Figure 6.5: Left pane: rotational distribution of N_2 molecules as a function of dissociation energy E. Right pane: fraction of dissociation energy converted to N_2 rotational energy (solid line) and final relative velocity v_{diss} of photofragments (dashed line).

6.6.2 Distribution of $|\omega_\lambda|$

In Figure 6.6 the relative yield of $|\omega_\lambda|$ states is plotted as a function of the rotational quantum number j of the N_2 fragment, centered around the most abundant j-value (j_{max}) at various dissociation energies. Considering the differences between our model potential and the real N_2O potential, as well as differences in the excitation mechanism, it is not surprising that the oxygen fragment polarization as a function of j_{max} differs significantly from the experimental distributions. The dipole (transition) surfaces in the model are chosen such that they obey all rules of symmetry relevant for the molecule, but no assumptions are made about the relative magnitude of the dipole moments. It can therefore be expected that more than the experimentally observed 3% of the excitation will take place to the $1'A''$ surface in the model. As result, interference between wavepackets propagating on the $1^1A''$ and the $2^1A''$ surfaces will significantly affect the $|\omega_\lambda|$ distribution. It can also be expected that the choice of the short-range nonadiabatic coupling matrix $\mathbf{U}(\theta)$ has significant influence on the actual ω_λ distribution.

The main difference between our result and the experiment by Teule *et al.*[58], is the increase in the $|\omega_\lambda| = 2$ population as a function of j, at the cost of $\omega_\lambda = 0$. Such a trend is lacking in the present results.
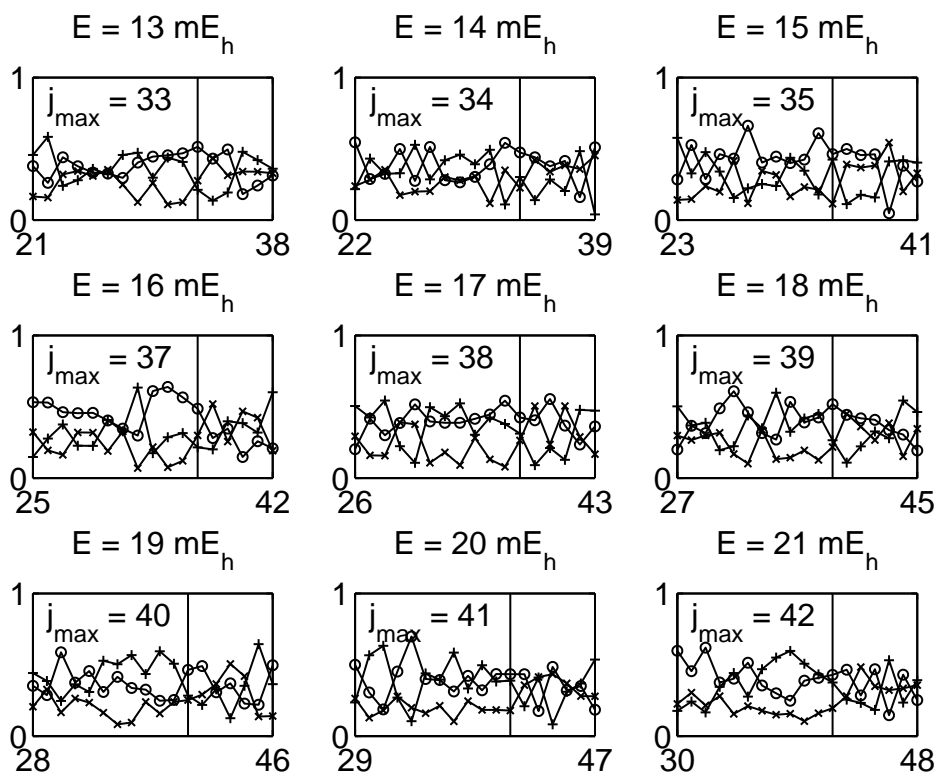
Figure 6.6: $|\omega_\lambda|$ distribution at various dissociation energies, as a function of N$_2$ rotation quantum number j. The relative yields of $\omega_\lambda = 0$ (+), $|\omega_\lambda| = 1$ (○) and $|\omega_\lambda| = 2$ (×) are plotted as a function of j, around the most abundant rotational state j_{max}, indicated with the vertical line, at the dissociation energy E. The highest j-value is the cutoff value for the distribution.

6.6.3 Convergence of product distribution functions

Measures for convergence

In order to be able to see at what point the rotational and angular distributions become fixed, we performed a series of convergence tests, where scattering wave functions and cross sections are computed by numerov propagation over s-grids of varying length, given by $2.20, 2.22, \ldots, s_i$. We thus get a sequence of computed cross sections $\{\sigma_{\mathbf{fi}}^{(i)}(\omega), \ i = 1, 2 \ldots n\}$, corresponding to different propagation distances $s_1, s_2, \ldots s_n$. This sequence of cross sections should converge as $n \to \infty$. We define the following convergence

parameter for the total cross section:

$$d_i(\omega) = \frac{|\sum_{j\omega_\lambda} \sigma_{\mathbf{fi}}^{(i)}(\omega) - \sigma_{\mathbf{fi}}^{(n)}(\omega)|}{\sum_{j\omega_\lambda} \sigma_{\mathbf{fi}}^{(n)}(\omega)}. \tag{6.61}$$

In order to study the convergence properties of the rotational and ω_λ product distributions, we first define the distribution function

$$P_j^{(i)}(\omega) = \frac{\sum_{\omega_\lambda} \sigma_{\mathbf{fi}}^{(i)}(\omega)}{\sum_{j\omega_\lambda} \sigma_{\mathbf{fi}}^{(i)}(\omega)}, \tag{6.62}$$

for the rotational distributions, and the distribution function

$$P_{\omega_\lambda}^{(i)}(j, \omega) = \frac{\sigma_{\mathbf{fi}}^{(i)}(\omega)}{\sum_{\omega_\lambda} \sigma_{\mathbf{fi}}^{(i)}(\omega)}, \tag{6.63}$$

for the ω_λ distribution at a given value of j. The convergence parameter we use is given by:

$$d_i'(\omega) = \frac{1}{2} \sum_k |P_k^{(i)}(\omega) - P_k^{(n)}(\omega)|, \tag{6.64}$$

where k can stand for ω_λ or j. It follows from the definitions of $d_i(\omega)$ and $d_i'(\omega)$ that $0 \leq d_i(\omega) \leq 1$ and $0 \leq d_i'(\omega) \leq 1$. We use the propagation distances $s_i = 6, 7, 8, 9, 10, 12, 14, 16$ a_0. The value of the cross section at 16 a_0 is considered the converged value.

Results

In Figure 6.7 the convergence of the total cross section is shown as a function of propagation distance and dissociation energy. In the left pane, each line corresponds to calculations where the energy is kept fixed and the propagation distance varied, and in the right paneleach line corresponds to a calculation where the propagation distance is kept fixed and the dissociation energy is varied.

It can be seen that the total cross section in general converges as the propagation distance increases. At a propagation distance of about 6 a_0, the total cross section differs less than about 10% from the converged cross section. There is no clear correspondence between the dissociation energy and the convergence of the total cross section.
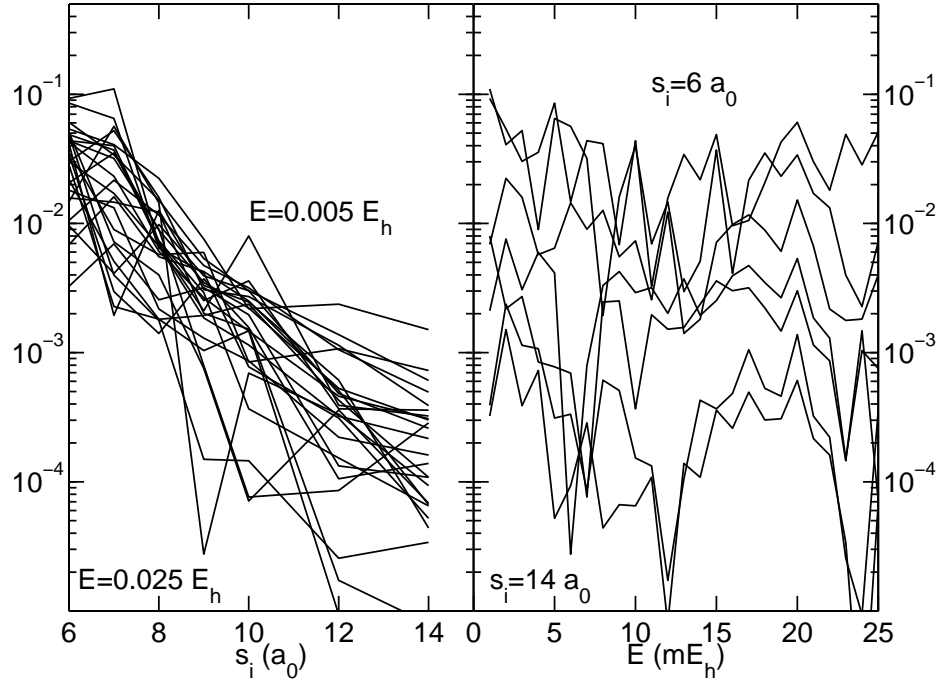
Figure 6.7: Convergence $d_i(\omega)$ of total photodissociation cross section as a function of s_i and energy, as defined in Eq. (6.61).
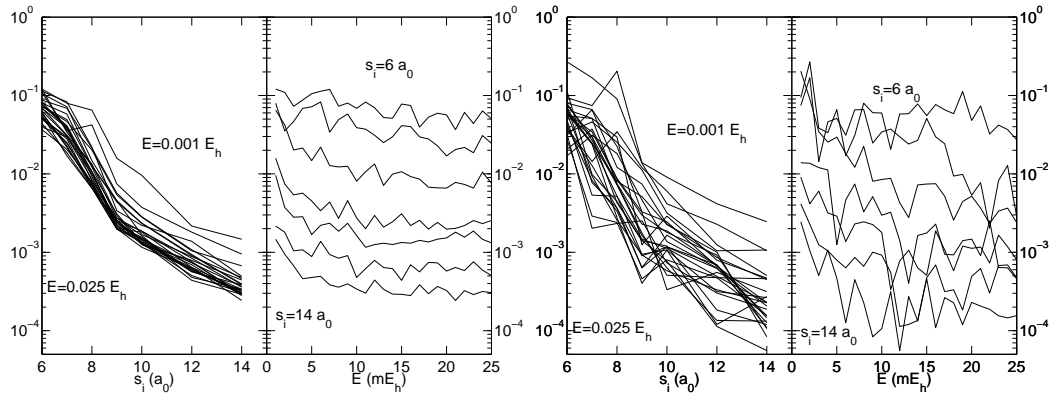
Figure 6.8: Left pane: convergence $d'_i(\omega)$ of rotational distribution, as a function of dissociation energy E and propagation distance s_i. Right pane: *idem*, but for the ω_λ distribution. The convergence parameters are defined in Eq. (6.64).

The situation is somewhat different for convergence of the rotational distribution, which is plotted in the left panel of Figure 6.8. The rate of convergence as a function of propagation distance s_i depends on the total dissocia-

tion energy. Calculations performed at higher dissociation energies converge faster as a function of s_i. This indicates that at at higher energies the rotational distribution is determined at smaller dissociation distance s. At a propagation distance of 7 a$_0$, the rotational distribution differs less than 10% from the converged distribution for all but the lowest dissociation energies.

In the right panelof Figure 6.8, the convergence behaviour of the ω_λ distribution is plotted for the most likely j-state occuring at each dissociation energy. It can be seen that as the propagation distance s_i increases, the dependence of $d'_i(\omega)$ on energy gets stronger. Thus, as the energy of dissociation gets higher, the ω_λ-distribution is determined at shorter interfragment separation distances. At higher dissociation energies, the ω_λ distribution differs less than 10% from the converged distribution at 16 a$_0$.

Given the above results, we are now able to discuss the relation with the analytical long-range interaction model. Remember that this model implicitly assumes that in the region where the ω_λ distribution is determined, the potential behaves as the analytical quadrupole-quadrupole interaction. It follows from our results, that even in this strongly simplified model about 90% of the final j-distribution and oxygen polarization are determined in a region where the shape of the potential differs significantly from the long-range potential. This indicates that the assumption that the potential can be described as a quadrupole-quadrupole interaction in the recoupling region is probably too strong.

On the other hand, the assumption that the dependence of the fragment polarization on the j-level can be translated into a dependence on the bending angle θ seems quite plausible.

Dissociation takes place mostly on the Δ state surfaces. At a distance of 6 a$_0$, the maximum difference in energy between the adiabatic $\Delta(1A''; 1A_2)$ and $\Delta(2A'; 2A)$ states is about 0.15 mE$_h$ at $\theta = \pi/2$, which is about 30 times smaller than the smallest dissociation energy used here. The energy differences decreases to about 0.04 mE$_h$ at 7 a_0 and about 5×10^{-6} E$_h$ at 8 a_0 respectively. Judging from the data plotted in the right panelof Figure 6.8, a convergence of the ω_λ distribution up to 10% from the final result is obtained when the maximum ratio between the energies of the relevant electronic energy surfaces and the dissociation energy is on the order of 0.001-0.01. Similarly, we find that a ratio on the order of about 5% is enough to converge the rotational distribution to within 10% of it's final value.

6.7   Conclusion and outlook

We present 2-dimensional model potential energy surfaces and electronic dipole (transition) moment surfaces which can be useful in studying models for photodissociation of N$_2$O-like molecules. The model potentials and dipole moment surfaces obey all restrictions imposed by the symmetry of the system and the long-range quadrupole-quadrupole interaction is reproduced analytically for the potential energy surfaces. A model transformation between the adiabatic and diabatic representations of the electronic states was developed, based on the long range analytical transformation.

The transformation matrices and model potentials are used to judge the validity of a long-range interaction model, used to the predict the O($^1D_2$) electronic polarization upon the photodissociation reaction N$_2$O $+ \hbar\omega \rightarrow$ N$_2$(X$^1\Sigma^+$) $+$ O($^1D_2$). To this end the rotational distribution of the N$_2$ fragment and polarization of the O($^1D_2$) fragment are computed using time-independent methods and compared with experiment. We conclude that there is qualitative agreement with the rotational distribution, in the sense that both in the experiment and in the model calculation a high percentage of the available dissociation energy is transferred to rotational energy of the N$_2$ fragment. There is no clear similarity between the experimental and calculated O($^1D_2$) polarization, mostly because of differences in the model nonadiabatic couplings and the excitation mechanism.

In order to gain some insight into where the polarization of the oxygen fragment becomes fixed, convergence properties of the calculated cross sections were studied, as a function of energy and propagation distance. The results indicate that the N$_2$ rotational distribution becomes fixed earlier in the dissociation process than the oxygen polarization. It is concluded that at moderately high energies, more than 90% of the distribution is fixed at relative short range. Most of the dynamics relevant for determining the N$_2$ rotational distribution and the oxygen polarization takes place on a range shorter than 6 a_0. The rotational distribution converges when the ratio between energy differences between the electronic surfaces on which the dissociation takes place, and the dissociation energy, is on the order of 5%, while the polarization of the oxygen atom converges when this ratio is on the order of 0.1-1%. The results indicate that the quadrupole-quadrupole interaction is not the most important interaction which determines the final oxygen polarization distribution. However, the results indicate that the relation between oxygen polarization and N$_2$ rotational quantum number can be translated into a dependence of polarization on the bending angle between the N$_2$ and oxygen fragment.

The work presented here serves as a first step towards a complete descrip-

tion of photodissociation of N_2O-like molecules into electronically degenerate states. As a next step the excitation model should be improved, to better reflect the actual excitation. After this, the model transformation between diabatic and adiabatic states should be improved.

The long-range interaction model can possibly be improved by extending the model to (roughly) incorporate the angular dependence of the short-range potential. One of the key difficulties in building such a model description will be to find the transformation between the adiabatic and diabatic representation in the short range. The development of such models will undoubtedly be valuable in the interpretation of a great number of (planned) experiments.

Bibliography

1. G. R. Kirchhoff and R. W. Bunsen, Ann. Phys. (Leipzig) **186**, 161 (1860).
2. G. R. Kirchoff, in *Monatsberichte der Königlich Preussischen Akademi der Wissenschaften zu Berlin* (1859).
3. G. R. Kirchoff, Philos. Mag. **XIX**, 196 (1860).
4. J. C. Maxwell, Philos. Mag. **XXI**, 161 (1861).
5. J. C. Maxwell, Proc. R. Soc. London **XIII**, 531 (1864).
6. J. C. Maxwell, Philos. Trans. R. Soc. London **CLV**, 459 (1865).
7. J. C. Maxwell, Philos. Mag. **XXIX**, 152 (1865).
8. H. R. Hertz, *Untersuchungen über die Ausbreitung der elektrischen Kraft* (J. A. Barth, Leipzig, 1892), the results on radio waves were also published earlyer in Ann. Phys. Leipzig.
9. J. J. Ballmer, **25**, 80 (1885).
10. M. Planck, Ann. Phys. (Leipzig) **4**, 553 (1901).
11. A. Einstein, Ann. Phys. (Leipzig) **17**, 132 (1905).
12. Photoelectric effect: the phenomenon that metals can emit electrons from a metal surface under influence of light.
13. H. R. Hertz, Ann. Phys. (Leipzig) **31**, 421 (1887).
14. A. Einstein, Ann. Phys. (Leipzig) **22**, 180 (1907).
15. E. Rutherford, Philos. Mag. **XXI**, 669 (1911).
16. J. W. Geiger and E. M. Marsden, Proc. R. Soc. London **LXXXII**, 495 (1909).
17. J. W. Geiger, Proc. R. Soc. London **LXXXIII**, 492 (1910).
18. N. Bohr, Philos. Mag. **XXVI**, 1 (13).
19. F. Paschen, Ann. Phys. (Leipzig) **332**, 537 (1908).
20. T. Lyman, Astrophys. J. **23**, 181 (1906).
21. R. S. Muliken, Rev. Mod. Phys. **2**, 506 (1930).
22. R. S. Muliken, Phys. Rev. **36**, 611 (1930).
23. W. Heisenberg, Z. Phys. **33**, 879 (1925).

24. M. L. de Broglie, Ann. Phys. (Paris) **3**, 22 (1925).

25. E. Schrodinger, Ann. Phys. (Leipzig) **79**, 361 (1926).

26. E. Schrodinger, Ann. Phys. (Leipzig) **79**, 489 (1926).

27. E. Schrodinger, Ann. Phys. (Leipzig) **79**, 734 (1926).

28. W. Heitler and F. London, Z. Phys. **44**, 455 (1927).

29. P. A. M. Dirac, Proc. R. Soc. London **A114**, 243 (1927).

30. G. Uhlenbeck and S. Goudsmit, Naturwissenschaften **47**, 953 (1925).

31. G. Uhlenbeck and S. Goudsmit, Nature **117**, 264 (1926).

32. P. A. M. Dirac, Proc. R. Soc. London, Ser. A **117**, 610 (1928).

33. P. A. M. Dirac, Proc. R. Soc. London, Ser. A **118**, 351 (1928).

34. H. Bethlem and G. Meijer:, Int. Rev. Phys. Chem **22**, 73 (2003).

35. A. Eppink and D. Parker, Rev. Sci. Instrum. **68** (1997).

36. D. Parker and A. Eppink, J. Chem. Phys **107** (1997).

37. M. J. Ashfold, N. H. Nahler, A. J. Orr-Ewing, O. P. j. Vieuxmaire P. L. Toomes, T. N. Kitsopoulos, I. A. Garcia, D. A. Chestakov, S.-M. Wu, and D. H. Parker, Phys. Chem. Chem. Phys. **8**, 26 (2006).

38. J. Doyle, B. Friedrich, R. Krems, and F. Masnou-Seeuws, Eur. Phys. J. D **31**, 149 (2004).

39. G. S. F. Dhont, J. H. van Lenthe, G. C. Groenenboom, and A. van der Avoird, J. Chem. Phys **123**, 184302 (2005).

40. W. Ubachs and E. Reinhold, Phys. Rev. Lett. **92**, 101302 (2004).

41. E. Reinhold, R. Buning, U. Hollenstein, A. Ivanchik, P. Petitjean, and W. Ubachs, Phys. Rev. Lett. **96**, 151101 (2006).

42. E. R. Hudson, H. J. Lewandowski, B. C. Sawyer, and J. Ye, Phys. Rev. Lett. **96**, 143004 (2006), `arXiv:physics/0601054`.

43. M. Born and J. M. Oppenheimer, Ann. Phys. (Leipzig) **84**, 457 (1927).

44. R. Wayne, *Chemistry of atmospheres* (Clarendon Press, 1985).

45. The all-sky images were copied from the Airglow Database of Tohoku University, http://pat.geophys.tohoku.ac.jp/airglowdb/.

46. M. Wardle and F. Yusef-Zadeh, Science **296**, 2350 (2002).

47. J. M. Weisberg, S. Johnston, B. Koribalski, and S. Stanimirovic, Science **309**, 5731 (2005).

48. M. D. Gray, K. N. Jones, R. C. Doel, D. Field, and R. N. F. Walker, *Astrophysical Masers* (Springer, 1993), p. 129, Lecture notes in physics.

49. P. F. Bowers, K. J. Johnston, and J. H. Spencer, nature **291**, 382 (1981).

50. E. F. van Dishoeck and A. Dalgarno, Icarus **59**, 305 (1984).

51. S. Lepp, P. C. Stancil, and A. Dalgarno, J. Phys. B **35**, R57 (2002).

52. A. Dalgarno, J. Phys.: Conference Series **4**, 10 (2005).

53. D. Galli and F. Palla, Astron. Astrophys. **335**, 403 (1998).

54. J. R. Partington, *A Short History of Chemistry* (Dover Publications, 1989).

55. J. T. Houghton, L. Filho, and N. B. Harris, *Climate change 1994; Radiative forcing of Climate Change and an Evaluation of the IPCC 1992 IS92 Emission Scenarios* (Cambridge University Press, 1995).

56. *Inventory of US greenhouse gas emission and sinks; 1990-2003* (U.S. Environmental Protection Agency, 2005).

57. G. C. Groenenboom, in *Vector Correlation and Alignment in Chemistry*, edited by G. G. Balint-Kurti and M. P. de Miranda (Collaborative computational project on molecular quantum dynamics (CCP6), Daresbury, United Kingdom, 2005), pp. 44–47.

58. J. M. Teule, G. C. Groenenboom, D. W. Neyer, D. W. Chandler, and M. Janssen, Chem. Phys. Lett. **320**, 177 (2000).

59. M. Brouard, R. Cireasa, A. P. Clark, T. J. Preston, C. Vallance, G. C. Groenenboom, and O. S. Vasyutinskii, J. Phys. Chem. A **108**, 7965 (2004).

60. M. E. Greenslade, M. I. Lester, D. Č Radenović, J. A. van Roij, and D. H. Parker, J. Chem. Phys (2005).

61. M. P. J. van der Loo and G. C. Groenenboom, J. Chem. Phys **126**, 114314 (2007).

62. A. E. Douglas, Can. J. Phys. **52**, 318 (1974).

63. I. Easson and M. Pryce, Can. J. Phys. **51**, 518 (1973).

64. E. de Beer, M. P. Koopmans, C. A. de Lange, Y. Wang, and W. A. Chupka, J. Chem. Phys **94**, 7634 (1991).

65. E. de Beer, C. A. de Lange, J. A. Stephens, K. Wang, and V. McKoy, J. Chem. Phys **95**, 14 (1991).

66. C. McRaven, J. Alnis, B. Furneaux, and N. Shafer-Ray, J. Phys. Chem. **107**, 7138 (2003).

67. E. F. van Dishoeck, S. R. Langhoff, and A. Dalgarno, J. Chem. Phys **78**, 4552 (1983).

68. J. A. Stephens and V. McKoy, J. Chem. Phys **93**, 7863 (1990).

69. J. A. Stephens and V. McKoy, Phys. Rev. Lett. **62**, 889 (1989).

70. E. F. van Dishoeck and A. Dalgarno, Icarus **56**, 184 (1983).

71. E. F. van Dishoeck, M. C. van Hemert, A. C. Alison, and A. Dalgarno, J. Chem. Phys **81**, 5709 (1984).

72. J. P. Morgenthaler, W. M. Harris, F. Scherb, C. M. Anderson, R. J. Oliversen, N. E. Doane, M. R. Combi, M. L. Marconi, and W. H. Smith, Astrophys. J. **563**, 451 (2001).

73. T. Seideman and W. H. Miller, J. Chem. Phys **96**, 4412 (1992).

74. T. Seideman and W. H. Miller, J. Chem. Phys **97**, 2499 (1992).

75. T. Seideman, J. Chem. Phys **98**, 1989 (1993).

76. G. Herzberg, *Molecular Spectra and Molecular Structure, Vol. 1: Spectra of Diatomic Molecules* (Van Nostrand, New York, 1950).

77. R. N. Zare, *Angular Momentum* (Wiley, New York, 1988).

78. M. C. G. N. van Vroonhoven and G. C. Groenenboom, J. Chem. Phys **116**, 1965 (2002).

79. H.-J. Werner, P. J. Knowles, R. Lindh, F. R. Manby, M. Schütz, P. Celani, T. Korona, G. Rauhut, R. D. Amos, A. Bernhardsson,, *Molpro, version 2006, a package of ab initio programs* (2006).

80. P. J. Knowles and H.-J. Werner, Chem. Phys. Lett. **145**, 514 (1988).

81. H.-J. Werner and P. J. Knowles, J. Chem. Phys **89**, 5803 (1988).

82. H.-J. Werner and P. J. Knowles, J. Chem. Phys **82**, 5053 (1985).

83. P. J. Knowles and H.-J. Werner, Chem. Phys. Lett. **115**, 259 (1985).

84. R. McWeeny, *Methods of Molecular Quantum Mechanics* (Academic, London, 1989), 2nd ed., chapter 5.

85. S. R. Langhoff and E. R. Davidson, Int. J. Quantum Chem. **8**, 61 (1974).

86. T. H. Dunning, J. Chem. Phys **90**, 1007 (1989).

87. Atomic energy levels are taken from the National Institute of Standards and Technology (NIST) atomic spectra database. See http://physics.nist.gov/cgi-bin/AtData/main_asd.

88. R. A. Copeland, B. R. Chamala, and J. A. Coxon, J. Mol. Spectrosc. **161**, 243 (1993).

89. J. R. Ackerhalt and J. H. Eberly, Phys. Rev. A **14**, 1705 (1976).

90. M. S. Pindzola, Phys. Rev. A **17**, 1021 (1978).

91. L. Allen, R. W. Boyd, J. Krasinski, M. S. Malcuit, and C. R. Stroud, Jr., Phys. Rev. Lett. **54**, 309 (1985).

92. D. J. Bamford, L. E. Jusinski, and W. K. B. and, Phys. Rev. A **34**, 185 (1986).

93. R. P. Saxon and J. Eichler, Phys. Rev. A **34**, 199 (1986).

94. D. P. Craig and T. Thirunamachandran, *Molecular quantum electrodynamics* (Academic, London, 1984).

95. R. Loudon, *The quantum theory of light* (Oxford University Press, Oxford, 1973).

96. G. J. Fiechtner and J. R. Gord, J. Quant. Spectros. Radiat. Transfer **68**, 543 (2000).

97. J. D. Jackson, *Classical Electrodymanics* (Wiley, New York, 1975), 2nd ed.

98. W. M. McLain and R. A. Harris, in *Excited states*, edited by E. C. Lin (Academic, New York, 1977), vol. 3, pp. 1–57.

99. K. Omnidvar, Phys. Rev. A **22**, 1576 (1980).

100. D. T. Colbert and W. H. Miller, J. Chem. Phys **96**, 1982 (1992).

101. G. C. Groenenboom and D. T. Colbert, J. Chem. Phys **99**, 9681 (1993).

102. H. Lefebvre-Brion and R. W. Field, *Perturbations in the spectra of diatomic molecules* (Academic, New York, 1986).

103. R. Schinke, *Photodissociation Dynamics* (Cambridge University Press, Cambridge, 1993).

104. R. Colin, P.-F. Coheur, M. Kiseleva, A. C. Vandaele, and P. F. Bernath, J. Mol. Spectrosc. **214**, 225 (2002).

105. F. Mélen, J. Sauval, N. Grevesse, C. B. Farmer, C. Servais, L. Delbouille, and G. Roland, J. Mol. Spectrosc. **174**, 490 (1995).

106. E. F. van Dishoeck and A. Dalgarno, J. Chem. Phys **79**, 873 (1983).

107. The computed potential energy curves and dipole transition moments are deposited at EPAPS Document No. E-JCPSA6-123-

037528 This document may be retrieved via the EPAPS homepage (http://www.aip.org/pubservs/epaps.html) or from ftp.aip.org in the directory /epaps/. See the EPAPS homepage for more information.

108. M. E. Greenslade, M. I. Lester, D. Č Radenović, A. J. A. van Roij, and D. H. Parker, Private communication.

109. D. C. Radenović, A. J. A. van Roij, D. A. Chestakov, A. T. J. B. Eppink, J. J. ter Meulen, D. H. Parker, M. P. J. van der Loo, G. C. Groenenboom, M. E. Greenslade, and M. I. Lester, J. Chem. Phys **119**, 9341 (2003).

110. A. L. Smith, J. Chem. Phys **55**, 4344 (1971).

111. A. C. Allison and A. Dalgarno, J. Chem. Phys **55**, 4342 (1971).

112. A. B. Meinel, J. Astrophys. **111**, 555 (1950).

113. F. Phillips, G. B. Burns, W. J. R. French, P. F. B. Williams, A. R. Klekociuk, and R. P. Lowe, Ann. Geophys. **22**, 1549 (2004).

114. H. M. Pickett, W. G. Read, K. K. Lee, and Y. L. Yung, **33**, 19808 (2006).

115. R. A. Viereck and C. S. Deehr, J. Geophys. Res. **94**, 5397 (1989).

116. U. B. Makhlouf, R. H. Picard, and J. R. Winick, J. Geophys. Res. **100**, 11289 (1995).

117. G. R. Swenson and C. S. Gardner, J. Geophys. Res. **103**, 6271 (1998).

118. T. G. Slanger, AGU Fall Meeting Abstracts pp. A3+ (2005).

119. A. García Muñoz, J. C. McConnell, I. C. McDade, and S. M. L. Melo, Icarus **176**, 75 (2005).

120. J. Meléndez, B. Barbuy, and F. Spite, Astrophys. J. **556**, 858 (2001), `astro-ph/0104184`.

121. S. Y. T. van de Meerakker, P. Smeets, N. Vanhaecke, R. T. Jongema, and G. Meijer, Phys. Rev. Lett. **94**, 023004 (2005).

122. S. Y. T. van de Meerakker, N. Vanhaecke, M. P. J. van der Loo, G. C. Groenenboom, and G. Meijer, Phys. Rev. Lett. **95**, 013003 (2005).

123. V. I. Shklovskii, Dokl. Akad. Nauk. SSSR **80**, 735 (1950).

124. J. W. Chaimberlain and C. A. Smith, J. Geophys. Res. **64**, 611 (1959).

125. G. Kvifte, Planet. Space Sci. **5**, 158 (1961).

126. H. S. Heaps and G. Herzberg, Z. Phys. **133**, 48 (1952).

127. J. Wallace, J. Atmos. Sci. **19**, 1 (1962).

128. D. Garvin, H. P. Broida, and H. J. Kostowski, J. Chem. Phys **32**, 880 (60).

129. A. F. Ferguson and D. Parkinson, Planet. Space. Sci. **11**, 149 (1963).

130. V. I. Krassovsky, Dokl. Akad. Nauk. SSSR **80**, 735 (1951).

131. R. E. Murphy, J. Chem. Phys **54**, 4852 (1971).

132. L. Rothman, C. P. Rinsland, A. Goldman, S. T. Massie, D. P. Edwards, J.-M. Flaud, A. Perrin, C. Campy-Peyrret, V. Dana, J.-Y. Mandin,, J. Quant. Spectros. Radiat. Transfer **60**, 665 (1998).

133. J. Gilles and A. Goldman, J. Quant. Spectros. Radiat. Transfer **26**, 23 (1980).

134. A. Goldman, Appl. Opt. **21**, 2100 (1982).

135. A. Goldman, J. R. Gilles, and J. A. Coxon, J. Quant. Spectros. Radiat. Transfer **29**, 469 (1983).

136. F. Mies, J. Mol. Spectrosc. **53**, 150 (1974).

137. D. Turnbull and R. Lowe, Planet. Space Sci. **37**, 723 (1989).

138. P. C. Cosbey and T. G. Slanger, Can. J. Phys. **to be published** (2006).

139. V. I. Krassovsky, N. Shefov, and V. Yarin, Planet. Space Sci. **9**, 883 (1962).

140. A. Goldman, W. G. Schoenfeld, D.Goortvitch, C. C. Jr, H. Dothe, F. Mélen, M. C. Abrams, and J. E. A. Selby, J. Quant. Spectros. Radiat. Transfer **59**, 453 (1998).

141. D. D. Nelson Jr. and A. D. J. Nesbitt, J. Chem. Phys **90**, 5443 (1989).

142. D. D. Nelson Jr., A. Schiffman, D. J. Nesbitt, J. J. Orlando, and J. B. Burkholder, J. Chem. Phys **93**, 7003 (1990).

143. J. A. Coxon and S. C. Foster, J. Mol. Spectrosc. **91**, 243 (1982).

144. P. C. Cosby, T. G. Slanger, and D. L. Huestis, in *The 55th Ohio State University International Symposium on Molecular Spectroscopy* (2000).

145. M. C. Abrams, S. P. Davis, M. Rao, R. Engleman Jr, and J. W. Brault, Astrophys. J. Suppl. Ser. **93**, 351 (1994).

146. W. J. Stevens, G. Das, A. C. Wahl, M. Krauss, and D. Neumann, J. Chem. Phys **61**, 3686 (1974).

147. H.-J. Werner, P. Rosmus, and E.-A. Reinsch, J. Chem. Phys **79**, 905 (1983).

148. S. R. Langhoff, H.-J. Werner, and P. Rosmus, J. Mol. Spectrosc. **118**, 507 (1986).

149. S. R. Langhoff, C. W. Bauschlicher, and P. R. Taylor, J. Chem. Phys **91**, 5953 (1989).

150. S. R. Langhoff, C. W. Bauschlicher, and P. R. Taylor, J. Chem. Phys **86**, 6992 (1987).

151. E. Hill and J. H. van Vleck, Phys. Rev. **32**, 250 (1928).

152. R. N. Zare, A. L. Schmeltekopf, W. J. Harrop, and D. L. Albritton, J. Mol. Spectrosc. **46**, 37 (1973).

153. M. C. Abrams, S. P. davis, M. L. P. Rao, and R. E. Jr., J. Mol. Spectrosc. **165**, 57 (1994).

154. P. C. Cosbey, Private communication, the r_e value was determined by computing an RKR potential from the spectroscopic constants.

155. M. P. J. van der Loo and G. C. Groenenboom, J. Chem. Phys **123**, 074310 (2005).

156. The computed potential energy curve and properties are deposited at EPAPS Document No. E-JCPA6-017709. This document may be retrieved via the EPAPS homepage (http://www.aip.org/pubservs/epaps.html) or from ftp.aip.org in the directory /epaps/. See the EPAPS homepage for more information.

157. T.-S. Ho and H. Rabitz, J. Chem. Phys **104**, 2584 (1996).

158. J. A. Coxon and S. C. Foster, Can. J. Phys. **60**, 41 (1982).

159. K. I. Peterson, G. T. Fraser, and W. Klemperer, Can. J. Phys. **62**, 1502 (1984).

160. L. Rothman, D. Jacquemart, A. Barbe, D. C. Benner, M. B. L. Brown,

M. Carleer, C. C. Jr., K. Chance, L. Coudert, V. Dana,, J. Quant. Spectros. Radiat. Transfer **96**, 139 (2005).

161. G. Placzek and E. Teller, Z. Phys. **81**, 209 (1933).

162. S. R. Federman and L. Frommhold, Phys. Rev. A **25**, 2012 (1982).

163. A. Dalgarno and J. T. Lewis, Proc. R. Soc. London, Ser. A **233**, 70 (1955).

164. A. Dalgarno, A. L. Ford, and J. C. Browne, Phys. Rev. Lett. **27**, 1033 (1971).

165. A. L. Ford and J. C. Browne, Phys. Rev. A **7**, 418 (1973).

166. M. Marinescu, H. R. Sadeghpour, and A. Dalgarno, J. Opt. Soc. Am. B **10**, 988 (1993).

167. I. Simbotin, M. Marinescu, H. R. Sadeghpour, and A. Dalgarno, J. Chem. Phys **107**, 7057 (1997).

168. I. Simbotin, M. J. Jamieson, and A. Dalgarno, J. Geophys. Res. Atmospheres **109**, D13302 (2004).

169. L. Wolniewicz and G. Staszewska, J. Mol. Spectrosc. **212**, 208 (2002).

170. L. Wolniewicz and G. Staszewska, J. Mol. Spectrosc. **217**, 181 (2003).

171. L. Wolniewicz and G. Staszewska, J. Mol. Spectrosc. **220**, 45 (2003).

172. L. Wolniewicz, J. Chem. Phys **1851**, 99 (2004).

173. U. Fantz and Wünderlich, IAEA report INDC(NDS)-457, 2004. Available online via http://www-amdis.iaea.org. The calculations are based on the same *ab initio* data as the current work.

174. T. Abel and Z. Haiman, *Molecular hydrogen in space* (Cambridge, 1999), p. 237, Cambridge Contemporary Astrophysics.

175. P. C. Stancil, S. Lepp, and A. Dalgarno, Astrophys. J. **509**, 1 (1998).

176. P. C. Stancil and A. Dalgarno, Astrophys. J. **490**, 76 (1997).

177. A. J. Sauval and J. B. Tatum, Astrophys. J. Suppl. Ser. **56**, 193 (1984).

178. R. Wildt, Nature **134**, 418 (1934).

179. R. Wildt, Astrophys. J. **86**, 321 (1937).

180. R. P. Wayne, J. Geophys. Res. **98**, 13119 (1993).

181. A. Dalgarno, in *Astrophysics and Space Science Library Vol. 146: Rate Coefficients in Astrochemistry*, edited by T. J. Millar and D. A. Williams (1988), pp. 321–338.

182. Y. L. Yung and W. B. Demore, eds., *Photochemistry of planetary atmospheres* (1999).

183. D. J. Hollenbach and A. G. G. M. Tielens, Rev. Mod. Phys. **71**, 173 (1999).

184. B. T. Draine and F. Bertoldi, Astrophys. J. **468**, 269 (1996), `astro-ph/9603032`.

185. E. W. van Dishoeck and M. C. van Hemert, Proc. R. Soc. Chem. Faraday Discuss. **133**, 231 (2006).

186. H. Yurimoto and K. Kuramoto, Science **305**, 1763 (2004).

187. D. J. Hollenbach, T. Takahashi, and A. G. G. M. Tielens, Astrophys. J. **377**, 192 (1991).

188. D. J. Hollenbach and A. G. G. M. Tielens, Annu. Rev. Astron. Astrophys. **35**, 179 (1997).

189. A. G. G. M. Tielens and D. Hollenbach, Astrophys. J. **291**, 747 (1985).

190. A. G. G. M. Tielens and D. Hollenbach, Astrophys. J. **291**, 722 (1985).

191. A. Dalgarno, Proc. R. Soc. Chem. Faraday Discuss. **133**, 9 (2006).

192. S. Jung, E. Tiemann, and C. Lisdat, Phys. Rev. A **74**, 040701 (2006).

193. S. Jung, E. Tiemann, and C. Lisdat, J. Phys. B **39**, S1085 (2006).

194. A. Coroiu, D. H. Parker, and G. C. Groenenboom, Eur. Phys. J. D **38**, 151 (2006).

195. M. Brouard, R. Cireasa, A. P. Clark, G. C. Groenenboom, G. Hancock, S. J. Horrocks, F. Quadrini, G. A. D. Ritchie, and C. Vallance, J. Chem. Phys **125**, 133308 (2006).

196. M. N. Daud, G. G. Balint-Kurti, and A. Brown, J. Chem. Phys **122**, 054305 (2005).

197. W. B. Zeimen, J. Kłos, G. C. Groenenboom, and A. van der Avoird, J. Chem. Phys **118**, 7340 (2003).

Publications

1. Predissociaton of the $A^2\Sigma^+(v=3)$ state of the OH radical
   D. Č. Radenović, A. J. A. van Roij, S. -M. Wu, J. J. ter Meulen,
   D. H. Parker, M. P. J. van der Loo and G. C. Groenenboom
   J. Chem. Phys. submitted (2008)

2. Photodissociation of vibrationally excited OH/OD radicals.
   D. Č. Radenović, A. J. A. van Roij, S. -M. Wu, J. J. ter Meulen, D. H.
   Parker, M. P. J. van der Loo, L. M. C. Janssen and G. C. Groenenboom
   Mol. Phys. accepted (2008)

3. Theoretical transition probabilities for the OH Meinel system.
   M. P. J. van der Loo and G. C. Groenenboom
   J. Chem. Phys. **126** 114314 (2007). Erratum, submitted (2008)

4. Photodissociation of vibrationally excited SH and SD radicals at 288
   and 291 nm: The $S(^1D_2)$ channel
   L. M. C. Janssen, M. P. J. van der Loo, G. C. Groenenboom, S. -M. Wu,
   D. Č. Radenovic, A. J. A. van Roij, I. A. Garcia and D. H. Parker
   J. Chem. Phys. **126** 094304 (2007)

5. Recombination of H_2 by Raman association in the early Universe.
   A. Dalgarno and M. P. J. van der Loo.
   ApJ-letters **646** L91 (2006)

6. Raman association of H_2 in the early universe.
   M. P. J. van der Loo, G. C. Groenenboom, M. J. Jamieson and A. Dal-
   garno
   Proc. R. Soc. Chem. Faraday Discussions **133** 43 (2006)

115

7. Direct radiative lifetime measurement of trapped OH radicals.
   S. Y. T. van de Meerakker, N. Vanhaecke, M. P. J. van der Loo,
   G. C. Groenenboom and G. Meijer
   Phys. Rev. Lett. **95** 013003 (2005)

8. Ab initio calculation of (2+1) REMPI spectra and lifetimes of the
   $(D, 3)^2\Sigma^-$ states of OH and OD.
   M. P. J. van der Loo and G. C. Groenenboom
   J. Chem. Phys. **123** 074310 (2005)

9. Concentratie OH in atmosfeer begrepen
   Mark P. J. van der Loo *Chemisch2Weekblad* **100** 19 (2004)

10. Photodissociation of the OD radical at 226 and 243 nm.
    D. C. Radenovic, A. J. A. van Roij, D. A. Chestakov, A. T. J. B. Ep-
    pink, J. J. ter Meulen, D. H. Parker, M. P. J. van der Loo, G. C. Groe-
    nenboom, M. E. Greenslade, and M. I. Lester
    J. Chem. Phys. **119** 9341 (2003)

Summary

The study of interaction between electromagnetic radiation (light) and molecules is of importance in many areas of science. Understanding these processes on a fundamental level can therefore be of great value.

This dissertation deals with theoretical and computational investigations into several photodynamical processes taking place in the hydroxyl radical (OH), molecular hydrogen (H_2) and nitrous oxide (N_2O).

In Chapter 2, a number of high-level *ab initio* potential energy curves and (transition) dipole moments for the OH molecule are computed. The bound state energy levels obtained from these potentials show good agreement with experimental values. The results are used to estimate the (2+1) resonance enhanced multiphoton ionization (REMPI) spectrum for the $(D, 3)^2\Sigma^-(v') \leftarrow X^2\Pi(v'')$ transitions, which is compared with experiments by M. E. Greenslade *et al.*. Qualitative agreement with experiment for the line strengths is obtained. Furthermore, the decay rate of the Rydberg $^2\Sigma^-$ states are computed, where the effect of predissociation is incorporated for the first time. It is shown that the lifetime of the Rydberg $^2\Sigma^-$ states for rotationally cold molecules is limited mainly by predissociation caused by spin-orbit coupling.

In Chapter 3, a new potential energy curve, electric dipole moment function, and spin-orbit coupling function for OH in the $X^2\Pi$ state, based on high-level *ab initio* calculations is presented. These properties, combined with a spectroscopically parametrized lambda-type doubling Hamiltonian, are used to compute the Einstein A coefficients and photoabsorption cross sections for the OH Meinel transitions. Comparing with earlier *ab initio* calculations, it is concluded that our dipole moment and potential energy curve give the best agreement with some of the experimental data to date.

In Chapter 4, the formation of molecular hydrogen by an inelastic Raman

scattering process (Raman association) is investigated. The process may be of importance in several astrophysical environments such as star-forming regions or, H_2-formation in the early universe. In the Raman process that is studied, a photon is scattered by a pair of colliding hydrogen atoms leaving a hydrogen molecule that is stabilized by the transfer of kinetic energy to the photon. Both the Placzek-Teller approximation and the Kramers-Heisenberg equation are used in the calculation of the scattering cross sections. Raman association cross sections are calculated on a wide range of photon energies for the first time, and it is shown that the Placzek-Teller model fails at certain energies.

In Chapter 5, H-H Raman association cross sections are computed with methods explained in Chapter 4 as a function of H-H scattering energy and radiation wavelength. These cross sections are then used to compute the rate of Raman association as a function of hydrogen gas temperature and radiation temperature. Using a cosmological model, the Raman association rate in the cosmic background radiation field present during the early stages of the universe is determined. A comparison with other H_2-forming processes is made. It is concluded that Raman association contributed significantly to the H_2 population for a short time during and after the recombination era. However, the total relative contribution, counted over the time from recombination to the start of star formation ($\sim 10^8$ yr. after the big bang) is only minor.

In Chapter 6 the validity of an analytical long-range interaction model is investigated. This model has recently been used to interpret recent molecular photodissociation experiments. The experiments involve a determination of photofragment electronic polarization parameters using molecular beam techniques. Validity of the model is investigated by developing model potential energy surfaces, electronic dipole moment surfaces and nonadiabatic couplings for an N_2O-like molecule for which the long-range interaction model should hold. Detailed photodissociation calculations involving five adiabatic Born-Oppenheimer states are performed for the photodissociation reaction using these model properties. The oxygen polarization as a function of N_2 rotational state and photodissociation energy are obtained. The calculations are compared with the model and with experimental results by Teule *et al.*. Qualitative agreement between experimental and calculated N_2 rotational distributions are obtained. The calculations do not reproduce the experimental photofragment polarization, mainly due to differences between the modeled and experimental excitation step and because of the form of the nonadiabatic interactions in the model. A study of convergence behaviour as a function of the photodissociation grid reveals that assumptions behind the long-range interaction model are only partly valid.

Samenvatting

Onderzoek naar de interactie tussen electromagnetische straling (licht) en moleculen vindt toepassingen in allerlei wetenschappelijke en industriële vakgebieden. Een fundamenteel begrip van processen die optreden bij deze interactie is daarom van grote waarde.

Dit proefschrift is gewijd aan theoretisch onderzoek naar lichtgeïnduceerde processen in het hydroxyl radicaal (OH), het waterstofmolecuul (H_2) en stikstofoxidemolecuul (N_2O).

Het OH radicaal is een zeer reactief molecuul (radicaal) wat een belangrijke rol speelt bij verbrandingsprocessen en chemische processen in de aardatmosfeer. Verder is het een molecuul wat voorkomt in astrofysische omgevingen zoals regio's waar sterren worden geboren en interstellaire wolken. Een goed begrip van lichtgeïnduceerde processen in het OH radicaal draagt rechtstreeks bij aan onderzoek naar deze omgevingen. Het OH radicaal wordt vaak gebruikt als modelsysteem om theoretische en experimentele methoden te testen omdat het een van de kleinste open schil moleculen is. In hoofdstuk 2 worden nieuwe berekeningen aan electronische toestanden van het OH radicaal gepresenteerd. De uitkomsten van die berekeningen (potentiaalcurven en dipoolmomentcurven) zijn vervolgens gebruikt om de bewegingstoestanden van de O en H atoomkernen in het molecuul uit te rekenen. Hierbij is een uitstekende overeenstemming met de experimentele waarden gevonden. Vervolgens zijn de potentiaal- en dipoolmomentcurven gebruikt om de overgangssterkten bij een twee-foton absorptieproces te berekenen. De resultaten komen kwalitatief overeen met experimenteel bepaalde waarden uit een experiment van M.E. Greenslade *et al.*. Tot slot zijn een aantal vervalprocessen (via predissociatie en lichtemisie) van aangeslagen electronische toestanden in OH doorgerekend. De berekeningen tonen aan dat voor deze toestanden

(de $D^2\Sigma^-$ en $3^2\Sigma^-$ toestanden) predissociatie het belangrijkste vervalproces is.

In hoofdstuk 3 wordt de berekening van een nieuw dipoolmoment en spin-baancurve voor de electronische grondtoestand van OH beschreven. Deze zijn vervolgens gebruikt voor de berekening van de levensduren van aangeslagen kerntoestanden (het Meinel systeem). Vergeleken met eerdere *ab initio* berekeningen reproduceert deze berekening een aantal experimentele resultaten het best.

Moleculair waterstof (H_2) is het meest eenvoudige neutrale molecuul, en het meest voorkomende molecuul in het universum. Astrofysici nemen aan dat H_2 onder andere een belangrijke rol speelde bij de vorming van de eerste sterren, zo'n 10^8 jaar na de oerknal. Een vraag hierbij is welke processen een rol gespeeld hebben bij het vormen van H_2 uit een ijl gas van losse waterstofatomen. Hoofdstuk 4 beschrijft de vorming van moleculair waterstof via het Raman associatie proces. Raman associatie is een inelastisch verstrooiingsproces, waarbij achtergrondstraling wordt verstrooid aan twee botsende waterstofatomen. Tijdens dit proces staat het H-H botsingspaar kinetische energie af aan het veld, zodanig dat gebonden H_2 gevormd wordt. In hoofdstuk 4 wordt een methode besproken om de de werkzame doorsnede behorend bij dit proces uit te rekenen. De werkzame doorsnede is een maat voor de kans dat Raman associatie optreedt bij een gegeven H-H botsingsenergie en golflengte van achtergrondstraling. Er wordt gebruik gemaakt van twee methoden: de Placzek-Teller benadering en de Kramers-Heisenberg vergelijking. We concluderen dat de Placzek-Teller benadering niet voor alle relevante fotonenergiën geldig is.

In hoofdstuk 5 is de methode uit hoofdstuk 4 gebruikt om de werkzame doorsnede voor Raman associatie van H_2 te berekenen voor een groot aantal foton- en H-H botsingsenergiën. Deze doorsneden zijn vervolgens gebruikt om de reactiesnelheidsconstanten voor H-H Raman associatie te berekenen. De constanten hangen zowel af van de temperatuur van de achtergrondstraling als van de temperatuur van het atomaire waterstofgas. De constanten zijn vervolgens gebruikt in een kosmologisch model voor chemie in het vroege universum om de bijdrage van H_2-vorming door Raman associatie te berekenen. De conclusie is dat Raman associatie een significante bijdrage leverde aan H_2 vorming tijdens het recombinatie tijdperk (zo'n 10^5 jaar na de oerknal). Echter, de totale bijdrage van Raman associatie vanaf het recombinatie tijdperk tot aan de eerste stervorming (zo'n 10^8 jaar na de oerknal) is klein vergeleken met andere H_2-vormende processen.

Het stikstofoxidemolecuul N_2O is beter bekend is onder de naam lachgas. N_2O is ook een broeikasgas wat voorkomt in de aardatmosfeer. Stikstofoxide kan in de atmosfeer uiteenvallen (fotodissociëren) in N_2 en O onder invloed

van zonlicht. In het laboratorium kunnen fotodissociatie experimenten worden gedaan om de interactie tussen N_2 en O op een fundamenteel niveau te onderzoeken. Fotodissociatiepocessen zijn vaak zo ingewikkeld dat theoretische modellen nodig zijn om de experimenten te kunnen interpreteren. Hoofdstuk 6 beschrijft een onderzoek naar de geldigheid van een analytisch model, wat recentelijk gebruikt is om een N_2O fotodissociatieëxperiment te interpreteren. Tijdens dit experiment zijn de productverdeling van de O- en N_2 fragmenten bepaald. Specifiek zijn de rotatietoestanden van het N_2 fragment en de polarisatie (ladingsverdeling van de electronen) van het O fragment bepaald. De geldigheid van het analytische model is onderzocht door eerst model potentiaaloppervlakken en model dipooloppervlakken voor het dissociërende N_2O molecuul te ontwikkelen. Van het "model-N_2O" wat hiermee beschreven wordt, kan worden verwacht dat het analytische model ervoor opgaat. Vervolgens zijn quantummechanische fotodissociatieberekeningen uitgevoerd, gebruikmakend van vijf adiabatische model potentiaaloppervlakken. De verdeling van de N_2 rotatietoestanden komt kwalitatief overeen met de experimentele waarden. We vinden geen overeenstemming tussen de experimentele en berekende polarisatie van het zuurstofatoom. Een analyse van het convergentiegedrag van de fotodissociatieberekeningen laat zien dat de aannamen achter het analytische model slechts ten dele geldig zijn.

Naschrift

Dit proefschrift zou niet tot stand gekomen zijn zonder de hulp en steun van een aantal mensen. Hen wil ik hierbij bedanken.

Ten eerste Gerrit Groenenboom, voor de prettige samenwerking, de inspiratie en de vrijheid die ik kreeg bij het uitvoeren van dit project. Ik bedank Ad van der Avoird en Paul Wormer voor de samenwerking, de (wetenschappelijke) discussies en het kritisch lezen van de manuscripten. Alle medewerkers en studenten van Theoretische Chemie wil ik bedanken voor de collegialiteit en samenwerking: Marloes van Beek, Anna Fishuk, Rob van Harrevelt, Mathijs Hendriks, Guillome d'Hont, Liesbeth Janssen, Vivike Lapoutre, Dick Tanis, Gé Vissers, Mirjam van Vroonhoven en Wilfried Zeimen.

Ik bedank onze collega's van MLF voor de samenwerking: Hans ter Meulen, Dave Parker, Dragana Radenovic̀ en Shiou-Min (Malcom) Wu. I would like to thank Meg Greenslade and Marsha Lester from the Dpt. of Chemistry at the University of Pennsylvania for the pleasant cooperation. Thanks also to Alex Dalgarno for inviting me to the ITAMP institute and to Michael Jamieson for the pleasant cooperation on the H_2 project. Gerard Meijer, Bas van de Meerakker en Nicolas Vanhaecke dank ik voor de samenwerking aan het OH-levensduur project.

Ik bedank alle leden van promovendi organisatie Probe aan de bèta faculteit voor de gezelligheid naast het onderzoek.

Ik wil mijn ouders en mijn zus Yvonne bedanken voor alles wat ze voor, tijdens en na mijn studie voor mij betekend hebben en nog steeds betekenen.

E finalmente, eu gostaria de agradecer à Talita Pereira por ter entrado em minha vida e por estar ao meu lado. Todos os beijinhos para vocé querida!

Curriculum vitae

Naam	Mark Petrus Jacobus van der Loo
Geboortedatum	28 september 1976
Geboorteplaats	Deurne, Nederland

2007−	Methodoloog, Centraal Bureau voor de Statistiek
2003−2007	Promovendus, Instituut voor Theoretische Chemie, Radboud Universiteit Nijmegen. In 2005 een verblijf van 3 maanden aan het Institute for Theoretical Atomic, Molecular and Optical Physics aan Harvard University.
2000−2003	Informatische Chemie, RU Nijmegen, *cum laude*. Hoofdvak: theoretische chemie, Photodissociation and spectroscopy of OH. Winnaar Unilever research prijs 2003.
1996−2000	HLO-Chemie, Fontys Hogeschool Eindhoven. Stage aan het YTOL Institute of Technology, Ylivieska Finland: Analysing rheological data of high solid suspensions. Afstudeerstage bij NV Organon: Polymorphism of pharmaceutical compounds.
1992−1996	MLO-Chemie, Technisch Lyceum Einhoven
1988−1992	Jan van Berlaer MAVO, Helmond